Characterization of depleted monolithic active pixel sensors

Trinity College, Oxford



This thesis is submitted for a *Doctorate in Philosophy* degree

Kaloyan Metodiev

September 13, 2021

Abstract

Monolithic active pixel sensors are a viable detector option for many high energy particle physics experiments, as they reduce both the production cost and the amount of material required in a detector. They are produced in CMOS (Complementary Metal-Oxide Semiconductor) processes, which are ubiquitous across consumer electronics and therefore have been the focus of development for several decades. The thesis focuses on a prototype device produced in a 180 nm TowerJazz high resistivity CMOS process, which was initially designed for the ATLAS experiment. Specifically, it investigates the radiation hardness of the sensor by measuring the capacitance of the collection electrode and the depletion region before and after irradiation. There are inefficiencies found at the pixel corners after irradiation, which are also confirmed by previous test-beam campaigns.

A new chip with additional modifications designed to combat those inefficiencies was produced. A novel measurement using an X-ray test-beam was conducted to measure the effect of the new modifications. It was found that they reduce the corner inefficiencies after irradiation. Furthermore, an extrapolation technique was used to compare and contrast the results from the X-ray test-beam with conventional charged particle test-beam done on the same chip.

Preface

This thesis investigates the application of monolithic active pixel sensors in particle physics. Specifically, the thesis focuses on evaluating the radiation damage of such a sensor developed in a modified 180 nm TowerJazz CMOS process, initially designed for the outer layer of the ATLAS pixel detector. In chapter 3, the capacitance of the collection electrode is used as a parameter to determine the damage to the silicon. A technique developed for estimation of the conversion gain of a CMOS imager is used to measure the gain curve of the Investigator2 sample. All gain curves measured are validated by a monoenergetic X-ray source and the collection capacitance of the irradiated and non-irradiated samples is extracted from the results. The results show no change in the collection capacitance, thus suggesting that the silicon bulk is not substantially affected. The gain curves obtained are used in chapter 4 to convert the output signal of the device into a number of electron-hole pairs.

An important parameter and a direct measurement of radiation damage is the depletion region of a sensor. Thus a scan of the depletion region was performed using an edge transient-current technique (E-TCT) on the irradiated and non-irradiated Investigator2. One of the main challenges is to keep the device cold for a prolonged period of time. Preliminary E-TCT results along with the developed cooling set up are documented in Ref [56]. Further E-TCT studies showed that there are inefficiencies in the pixel corners for the irradiated sample. To better understand the physical processes behind the E-TCT results, the technique was simulated in TCAD software.

A new test chip, the mini-MALTA, was introduced to combat the low pixel corner efficiencies. This chip has additional modifications along the pixel edges. The effect of these modifications was measured in a charged particle test-beam, as well as in a novel X-ray test-beam. The results of the X-ray test-beam and its benefits and drawbacks are discussed in chapter 5 and published in Ref [57]. Additionally, to allow better comparison and conversion between the results of a charged particle

test-beam and an X-ray test-beam, an extrapolation technique is used, discussed in section 5.5 and published in Ref [55]. The additional modifications introduced with the mini-MALTA are found to have eliminated the inefficiencies at the pixel corners.

Contents

1 Introduction **1**

1.1 The Standard Model 2

1.2 Experimental particle physics 3

1.2.1 Large Hadron Collider 4

1.2.2 ATLAS experiment 6

1.2.3 The ATLAS Inner Tracker Upgrade 10

1.3 Monolithic pixel detectors in HEP 12

2 Silicon pixel detectors **14**

2.1 Interactions of particles with silicon 14

2.1.1 Charged particles 14

2.1.2 X-ray photons 18

2.2 Principles of p-n junctions 20

2.2.1 Semiconductor production 20

2.2.2 Depletion region 22

2.2.3 Signal generation 27

2.2.4 Shockley diode model 30

2.3 Types of silicon pixel sensors 32

2.3.1 Hybrid pixel detectors 33
2.3.2 Monolithic pixel detectors 34
2.4 Radiation damage 37
2.4.1 NIEL 37
2.4.2 TID 38
2.4.3 Annealing 39

3 Radiation hardness measured via the collection capacitance 40

3.1 The Investigator chip 40
3.1.1 Chip design 41
3.1.2 Active reset (pMOS) 45
3.1.3 Diode reset 46
3.2 Measuring collection electrode capacitance 48
3.2.1 Monoenergetic X-ray source 48
3.2.2 Pain-Hancock method 51
3.2.3 Source follower contributions 57
3.3 Comparison before and after irradiation 58
3.4 Summary 62

4 Depletion region comparison before and after irradiation 63

4.1 Laser E-TCT 63
4.1.1 Laser wavelength and power 64
4.1.2 Focusing 65
4.1.3 Cooling apparatus 67

4.1.4 Absolute position of depletion region 69

4.2 Comparison of depletion regions before and after irradiation 72

4.3 TCAD simulation of the depletion region 74

4.4 Estimation of the depletion region depth using MIPs 80

4.5 Summary 81

5 X-ray test-beam measurements of the charge collection shape 83

5.1 The mini-MALTA prototype 83

5.2 Experimental Setup 84

5.3 Analysis of the pixel response 87

5.3.1 Single pixel response 87

5.3.2 Pixel response maps 88

5.3.3 Pixel response as a function of radiation dose 89

5.3.4 Shape of the charge collection area 91

5.3.5 Pixel response as a function of external bias voltage 92

5.4 Charge Sharing 94

5.4.1 Analysis from pixel response maps 94

5.4.2 Asymmetry of the pixels 96

5.4.3 Cluster sizes 97

5.5 MIP efficiencies from X-ray data 99

5.5.1 Methodology 101

5.5.2 Source measurements 104

5.5.3 Results 105

5.6 Summary 110

6 Conclusions **111**

Chapter 1

Introduction

By the end of the 19^{th} century, it was a well-established fact that matter was made up of atoms. In the beginning of the 20^{th} century subatomic investigations were conducted and the first model of the atom having a positive dense compact nucleus with the electrons orbiting it was created by Ernest Rutherford. It started the field of physics that studies subatomic particles. The theory of quantum mechanics was later developed and that helped with constructing a model for the subatomic particle called the Standard Model.

The Standard Model has been extensively verified by different experiments and its parameters measured to increasingly higher precision. This was made possible by the development of better equipment - more luminous and higher-energy accelerators and faster and more precise detectors. The Large Hadron Collider (LHC) is a proton-proton collider experiment with the highest luminosity and energy achieved so far. It has four different detectors adjusted for different types of measurements. This thesis is going to concentrate on one of them called ATLAS, which is a multi-purpose detector. In its innermost detector layers it has silicon pixel detectors, used to provide precise track reconstruction.

The currently used type of silicon detector in ATLAS inner pixel layers is called a hybrid detector, described later in this thesis. An alternative would be to use a depleted monolithic active pixel sensor (DMAPS), which would reduce the production cost, the thickness of the sensor and the pixel size. The DMAPS are produced using a process usually referred to as "CMOS process" in factories called foundries, making similar devices for chips and cameras in everyday use. In high-energy physics (HEP), the CMOS technology has been developed for other experiments like STAR[31] and

ALICE[75]. There are experiments currently at the end of their CMOS development process such as Mu3e[10] and future experiments like CLIC[74] and ILC[95], where the process is in the early stages. This thesis is going to focus on the development of CMOS technology for ATLAS.

Due to the high event rate that ATLAS has to detect, the silicon pixel layers need to survive a high dose of radiation - they need to be radiation hard. This is the main parameter which separates the ATLAS silicon pixel sensor to other experiments. The contents of the thesis are about one of the three main chip families that are DMAPS candidates for the ATLAS pixel detector. There are comparisons of different properties of the sensor before and after an equivalent lifetime dose of radiation, which evaluates radiation hardness.

1.1 The Standard Model

There are four known fundamental forces - electromagnetism, weak interaction, strong interaction and gravity. There is a quantum field theory description for the electromagnetism, weak and strong interaction, which is incorporated in the model as the four vector gauge bosons shown in Figure 1.1. The W and Z bosons are used to describe the weak interaction, the gluon mediates interactions via the strong force, and the photon is part of the quantum field theory for the electromagnetic interaction. The 12 fermions divided into three generations of matter. Each generation has higher mass than the previous one, hence all the ordinary matter is made from the first generation. Each of the fermionic particles has an anti-particle counterpart with the opposite charge and identical other properties. Each generation of fermions can be divided into 2 leptons and 2 quarks. The leptons have the property of existing on their own, but the quarks only exist in combinations with each other. Those combinations are separate particles called hadrons. The most recently discovered particle is the Higgs boson. It confirmed the Higgs mechanism [42], which is needed to explain the masses of the W and Z bosons and the Higgs field, which couples to the fermions to give them mass.

Even though the standard model best explains all experimental observations and is self-consistent, there are still unexplained phenomena and areas that need further development. To have a unified theory, gravity must be incorporated into the model. The existence of dark matter and dark energy is established from cosmological observations and is not explained by the Standard Model. To fit the

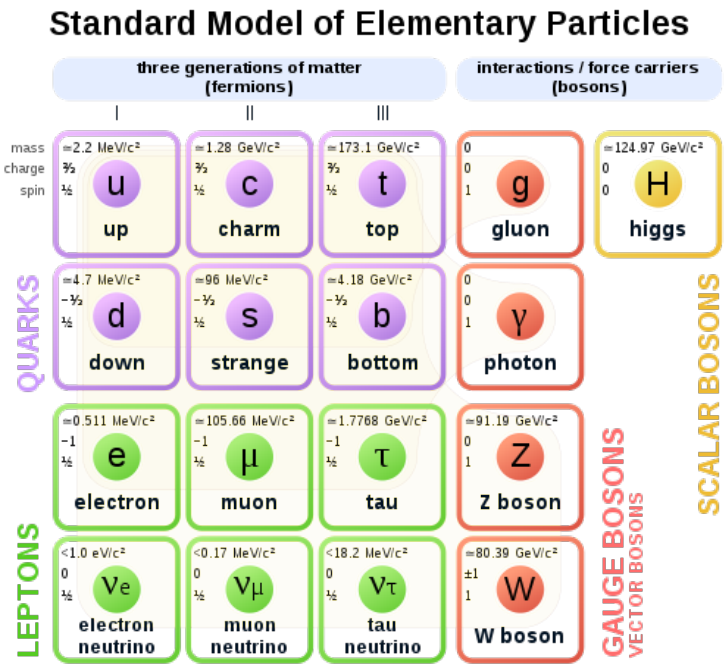


Figure 1.1: Illustration of the elementary particles in the Standard Model [61].

measured Higgs boson mass of 125 GeV/c^2 into the SM, extensive fine-tuning of parameters is needed. The reason for this is still unclear and this is known as the hierarchy problem [14]. These and other problems are targeted by the LHC and ATLAS.

1.2 Experimental particle physics

The SM is verified by using it to make predictions and building experiments to measure those predictions. Advancing the experimental equipment has lead to probing higher energy particles and getting higher resolution data. For most experiments a large chunk of information lies in the tracking - tracing the particle trajectory. This allows for pinpointing the origin of the particle (called primary vertex) and measuring the momentum from the curvature of the track if the particle is in a magnetic field. There are different types of tracking detectors such as time projection chambers (TPC), transition radiation trackers (TRT), muon chambers etc. Each detector has its application specification. The prototype chip, which is used throughout this thesis was being designed for the silicon pixel tracking in ATLAS. Therefore there is additional focus on the ATLAS silicon tracker.

Silicon tracking detectors can be strip or pixel ones. Strip detectors have been

used since the 1980s [16]. They were used in experiments like MARK II [49], where the fine granularity helped track recognition and resulted in one of the first B meson lifetime measurements. The 4 LEP experiments (ALPHA,DELPHI,OPAL,L3) had a silicon vertex detector, which enabled the distinguishability of Z-boson resonance events with a b-quark or a c-quark [82]. CDF [4] had silicon detectors for vertexing and momentum measurement, which lead to the discovery of the top quark. Later D0 [37] also installed a silicon vertex detector for their run II.

Silicon pixel detectors started getting developed at a later stage when the luminosity of the experiments increased and silicon trackers with faster readout capabilities and custom on-chip readout were needed [33]. The technology for pixels was already developing in the beginning of the 1990s and by the middle of the decade the first pixels were implemented in a fixed target experiment - WA97 [46], and a collider experiment - DELPHI [13]. Later they were chosen to instrument the innermost layers of ATLAS and CMS experiments at the LHC and played an important role in the discovery of the Higgs boson [8]. The technology used for silicon pixel detectors has been adjusted for X-ray imaging and has found application in other fields such as medicine, crystallography and chemistry.

1.2.1 Large Hadron Collider

The Large Hadron Collider (LHC) is a proton-proton circular collider with total circumference of 26.7 km [19]. It operates at a centre of mass energy of 13 TeV. There are two counter-rotating proton beams, which cross four times to create interaction points. The source of the protons is hydrogen gas injected into a metal cylinder, called a duoplasmatron. Its operating principle involves applying an electric field to separate the hydrogen atoms into electrons and protons. The protons are then injected into a linear accelerator, LINAC4 (previously LINAC2). A beam with smaller momentum needs a larger beampipe to be contained. This is measured by a parameter called beam emittance, which is related to the momentum and position of a particle perpendicular to the general beam direction. However, a larger radius of curvature is needed to extend the beam momentum, which directly increases the centre of mass energy achievable. Therefore the LHC has multiple stages of acceleration until the final LHC ring is reached. They are shown in Figure 1.2.

The protons travel along the two beamlines in bunches of about 10^{11} protons in each bunch. They are focused to collide at the interaction points and out of all

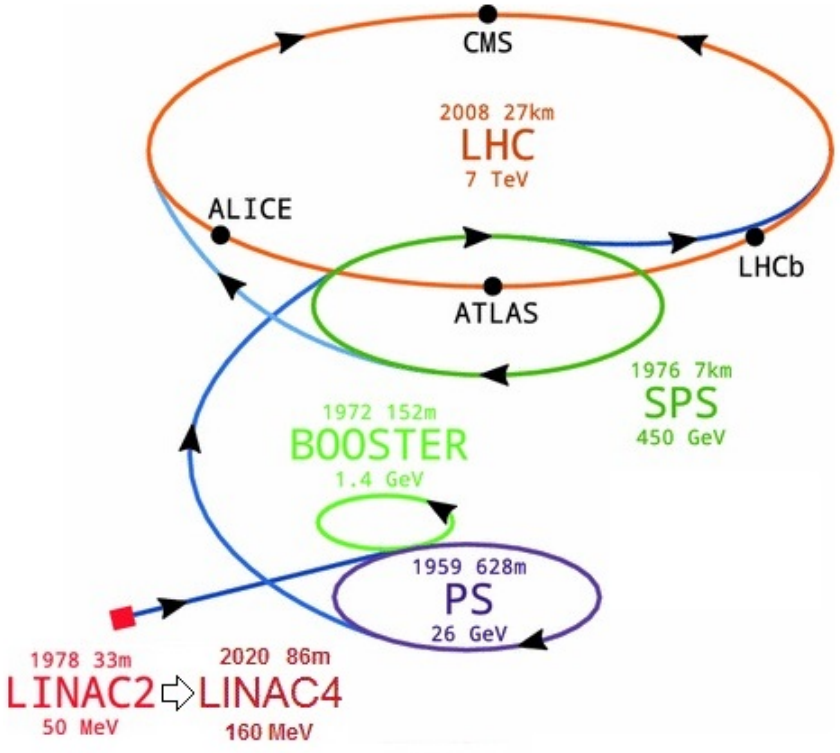


Figure 1.2: A sketch of the accelerating stages of the protons until the LHC beamline is reached. The four interaction points are labelled on the LHC ring with the main experiments that use them. Image adapted from [98].

the protons, there are about 30 collisions per bunch crossing. The bunch crossings are separated by 25 ns. In order to separate out events, ATLAS must have a timing resolution better than that. There are 1232 dipole magnets along the LHC ring keeping the protons circulating by producing a constant field of 7 T. There are thousands of other magnets as well keeping the beam focused, maintaining momentum spread and counteracting unwanted interacting of the bunches with themselves and the surrounding.

The standard model processes have to be measured with increasing precision for a better test of the model. This requires a larger number of events in order to reach the standard 5σ confidence limit. The LHC is scheduled for a tenfold upgrade of luminosity, which is referred to as the High Luminosity (HL) LHC upgrade [6]. All the detectors would need an upgrade as well to match the increased event rate and survive the increased radiation dose. In 2021 there will be a smaller upgrade on the centre of mass energy to 14 TeV for LHC Run 3 and in 2027 the HL-LHC run will start. The HL-LHC will operate at least 10 years.

1.2.2 ATLAS experiment

The ATLAS experiment is located at interaction point 1 on the LHC. It shares the interaction point for Run 3 of the LHC (2021-2023) with the FASER experiment, which will be looking for long-lived exotic particles. ATLAS is a general purpose detector with a cylindrical layout and is made up of different components as shown in Figure 1.3. Its dimensions are 44 m in length along the beamline and 25 m circular width and it has a total weight of 7000 tonnes. It is designed to measure the trajectory, energy and momentum of the particles produced in the LHC collisions. The end-caps ensure that the solid angle coverage is as close as possible to 4π. The detector is used to verify SM predictions, measure predicted coefficients to very high precision or look for enough events that do not match SM predictions and are considered new Beyond the Standard Model (BSM) physics.

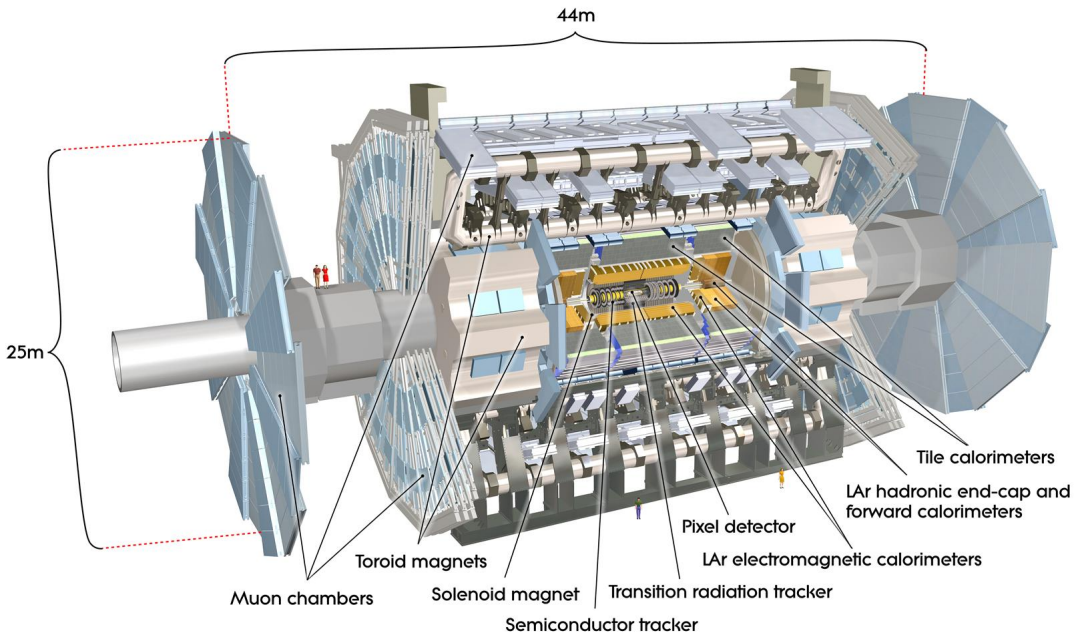


Figure 1.3: Computer generated image of the ATLAS detector cross-section with its components labeled [67].

There are four general sub-detector systems in the ATLAS experiment: the muon spectrometer (MS), the hadronic and electromagnetic calorimeters and the inner detector. There is a solenoid surround the inner tracker, generating a 2 T magnetic field. The field is used to measure the momentum of the particles by the trajectory curvature. A separate toroidal 0.4 T magnetic field is generated in the muon chamber for the same purpose.

The outermost part of the detector is the muon spectrometer as it is easily reached by muons. It measures the energy and momentum of the outgoing muons and provides a trigger information with good time resolution. The barrel part of it consists of monitored drift tubes (MDTs) and resistive plate chambers (RPC) and the end-cap sections consist of cathode strip chambers (CSCs) and thin gap chambers (TGCs).

Right below the muon spectrometer there is the calorimetry. The electromagnetic calorimeter (ECAL) is closer to the interaction point than the hadronic one (HCAL) both in the barrel and the end-caps. The ECAL is designed for photons, electrons and positrons. In the barrel it is made of lead and steel absorbers that develop electromagnetic showers and electrodes submerged in liquid argon (LAr) that produce and collect signal via ionization [63]. The collected signal is proportional to the energy of the particle and hence the energy is estimated. The first of three layers of the ECAL on the barrel has fine granularity to have a better estimate of position. Surrounding the ECAL in the barrel, there is a tile calorimeter which is part of the HCAL. It consists of many alternating layers of iron to stop the high energy showers and layers of plastic scintillator. The scintillators produce light when a particle excites atoms and they return to ground state emitting photons, which is what generates signal [25]. It is used to detect charged and neutral hadrons. The end-cap calorimetry consists of three main parts - closest to the beamline is the forward calorimeter (FCAL), then there are the electromagnetic end-cap calorimeter (EMEC) and hadronic end-cap calorimeter (HEC). They all use liquid argon, but have different materials to absorb particles.

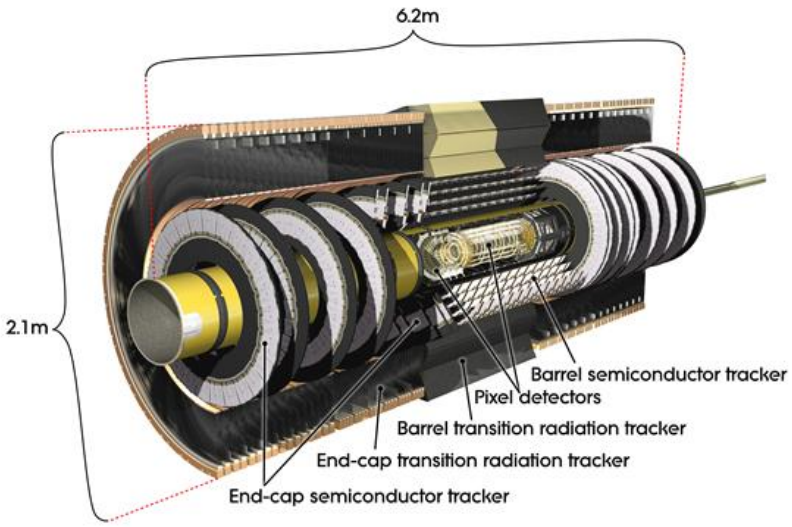


Figure 1.4: Computer generated image of the ATLAS inner detector [2].

In Figure 1.4 a computer generated image of the inner detector (ID) is shown. It is where the silicon detector is positioned. The purpose of the inner detector is to measure accurately the trajectory of the charged particles going out of the interaction point and then calculate their momentum and position. The ID has three main parts and starting from the outermost they are the Transition Radiation Tracker (TRT), Semiconductor Tracker (SCT) and the silicon pixel detector. The layout can be seen in Figure 1.5.

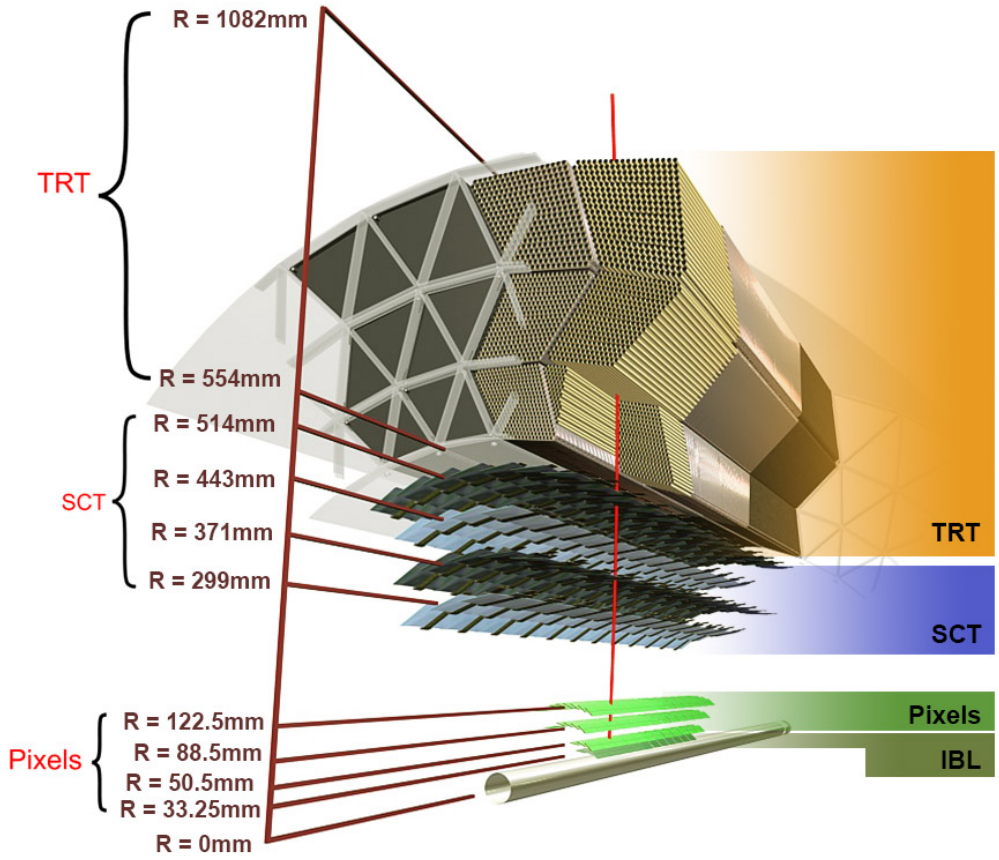


Figure 1.5: Image of the different layers in the inner detector and their position relative to the beamline [72].

The TRT measures transition radiation, produced when charged particles change medium. It consists of drift tubes that contain a mixture of Xe, CF_4 and CO_2 gases, which absorb the radiation of a charged particle traversing the detector and get ionised. The coating of each tube is conductive and kept at a very high negative voltage and a thin gold-plated tungsten wire is position in the centre of the tube. The charge from ionization drifts in that field to create signal. The TRT tubes are placed parallel to the beamline in the barrel region with a total length of 144 cm and radially in the end-caps [43]. Since the amount of radiation produced in the TRT depends on the mass of the charged particle, the detector is used for electron

identification as well as additional points on the trajectory of the particle.

The semiconductor tracker (SCT) is made from 4088 silicon strip modules [3]. There are four strip module layers in the barrel and nine disks in the end-cap regions. The silicon strip module consists of 2 back-to-back sensors of narrow strips of silicon ($\approx$ 80 μm wide) oriented at a 40 mrad degree angle so that the position of the traversing particle can be known. The principle of signal generation in silicon is explained in chapter 2.

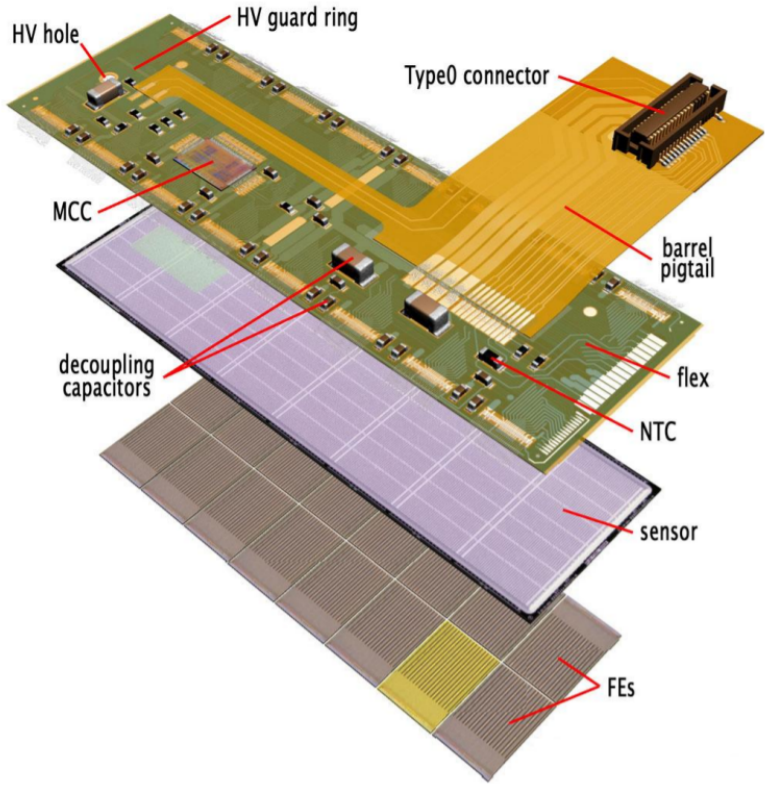


Figure 1.6: Schematic design of an FE-I3 pixel module. The FE ASIC is bump-bonded to the sensor and then the flexible readout circuit is glued on top of the sensor [29].

The silicon pixel layers are closest to the beamline. The top 4 pixel layers were built with a sensor chip called FE-I3 (Front End Interface 3), which is a hybrid pixel detector. The single chip has dimensions of 7.6 $\times$ 10.8 mm^2 and is assembled into a module that holds 16 of it. A schematic of the module is shown in Figure 1.6. There are 1744 modules in total [1]. The innermost layer is called an insertable B-layer (IBL). It was added during the long shutdown from 2012 to 2015 of the LHC. The sensor placed inside the IBL is an upgraded version of the FE-I3, called the FE-I4. The layer structure consists of 14 supporting staves along the beamline with a distance of 33 mm to the beam pipe [23]. Each stave carries 32 FE-I4 chips

with twelve planar sensor double-chip modules in the centre and four 3D sensor single-chip modules at each side. The FE-I4 chip has a smaller pixel pitch, higher active area, higher output data rate and survives the radiation dose that would be received that close to the beamline. In total the silicon pixel detector has more than 93 million separate readout channels.

1.2.3 The ATLAS Inner Tracker Upgrade

As the LHC luminosity is going to be increased in 2027, ATLAS needs to upgrade its equipment too. The Inner Detector needs to be able to detect more events ($\sim$ 200 events per collision). Therefore it needs finer resolution to prevent pile-up of events, higher data output rate and more radiation tolerant sensors.

The Inner Detector is going to be replaced with an all-silicon detector called the Inner Tracker (ITk). It will consist of strip modules and pixels. The strips would start a bit further than they currently do in the ID and extend to the end of the current ID. Everything below that would be filled with silicon pixel detectors. A simulated layout is shown in Figure 1.7.

The four layers of the strip barrel region extend to $\pm$1400 mm along the Z-axis. The strips will have a pitch of 75.5 μm and length 48.2 mm for the outer two layers. The inner two layers would be with the same pitch, but half the length - 24.1 mm. In the end-cap regions the layers are more variable ranging from 69.9 μm to 80.7 μm in width and 19.0 mm to 60.1 mm in length with the shorter and narrower ones being closer to the interaction point.

There are going to be 5 layers of silicon pixels in the barrels. The silicon detector chip is developed by the RD53 collaboration [38] and will have 50×50 μm ^{2} pixels. Silicon pixels in the end-caps are going to be mounted for improving the hermeticity of the detector. The pixel modules are going to be placed in half rings radially symmetric and positioned in a way to leave the least amount of gaps. There will be four layers of pixel rings on each side.

As the pixel layers are closest to the beamline, they receive the highest radiation dose. Therefore one of the challenges is to develop a chip that would survive that dose. The chip that is being developed is a hybrid pixel sensor, described in detail in subsection 2.3.1. An image of the simulated hadron fluences that each part of the detector would encounter is shown in Figure 1.8. Hadron fluence displaces atoms

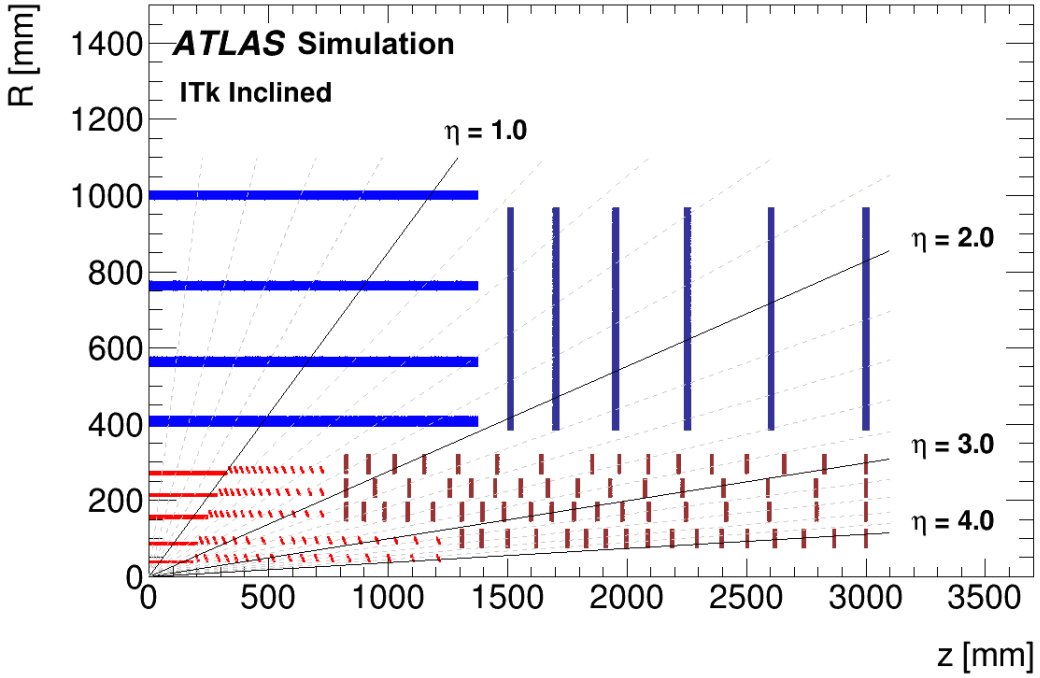


Figure 1.7: Image of the design of the ATLAS inner tracker. The origin of the image coincides with the interaction point and only a quarter of the detector is displayed. The blue and dark blue lines represent silicon strip detectors in the barrel and the end-cap respectively, while the red and darker red represent the intended silicon pixel layers. [28].

from the silicon lattice, thus creating defects and damaging the silicon bulk. Damage from hadron fluence and ionising radiation is discussed in more detail in section 2.4.

Due to the very high fluences on the first two barrel layers, it is planned that they are replaced during a long shutdown in the HL-LHC phase after collecting about 2000 fb^{-1} of particles. This thesis is about the chip family initially developed as a DMAPS alternative for ATLAS. Thus the first requirement was the radiation hardness needed to withstand the radiation dose received in the outermost layer - fluence of 10^{15} 1MeV n_{eq} cm^{-2}. There is an equivalent simulation for the total ionising dose (details in section 2.4), which for the outermost barrel pixel layer is equal to 80 Mrad. The requirements of the pixel chip are such that its efficiency needs to be $> 98.5\%$ before irradiation and $> 97\%$ after [89]. The timing of the chip needs to be fast enough, that all types of particles detected by the chip fall into a 25 ns window as this is the period of collisions.

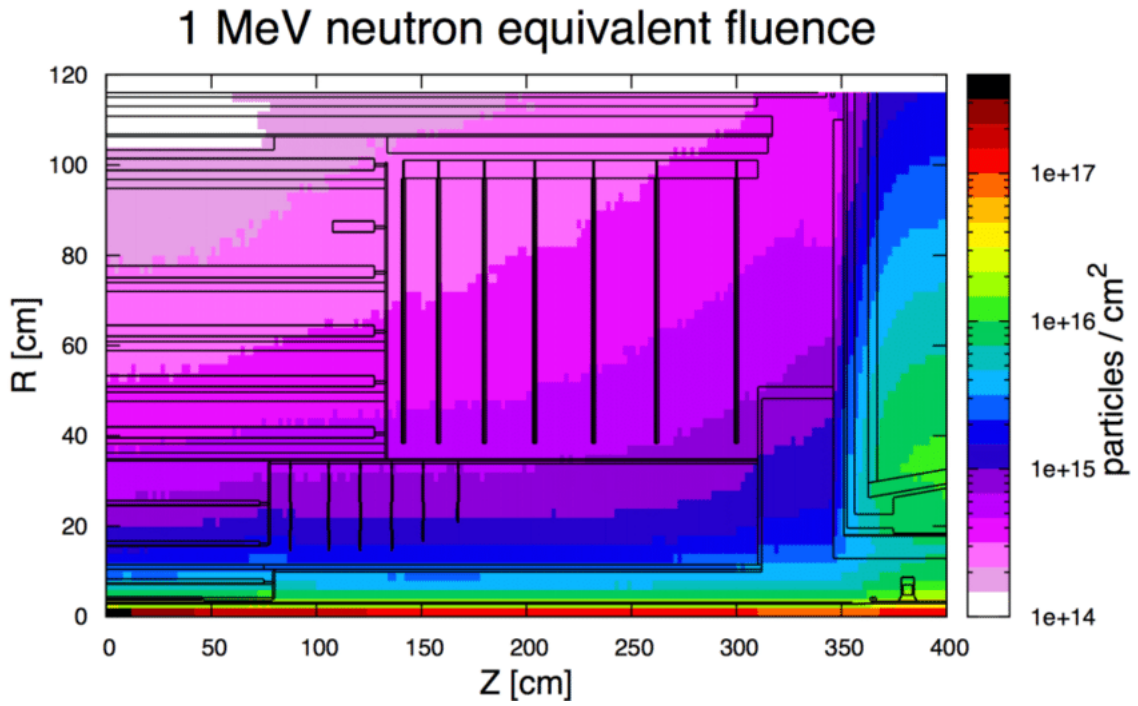


Figure 1.8: Image of part of the ATLAS Inner Tracker with the beamline on the bottom (Z-axis) and the interaction point being at the origin. The colors represent a simulated hadron fluence received for the whole lifetime of the expected HL-LHC run. The simulation is of the damage that would have been done by the same amount of neutrons with energy of 1 MeV [77].

1.3 Monolithic pixel detectors in HEP

Monolithic imaging sensors are devices that have the sensor part and the readout logic in the same block. Almost all contemporary cameras for everyday use are developed with such a structure. There are two general requirements that are important for this technology to make its way into HEP. The chips need to have low power consumption and a certain radiation hardness, while maintaining high efficiency and fast timing [87].

One of the main advantages of monolithic detectors is the lower production cost relative to the conventionally used hybrid pixel detectors. This comes from removing the bump-bonding step, explained in more detail in 2.3.1. For most experiments using or intending to use DMAPS, the lower cost is the main reason for the choice of this technology. Monolithic detectors also allow for reducing the total thickness of the detector. This is also an advantage, as it reduces the overall scattering. Experiments have different specifications for the detectors they are going to use. Thus there are DMAPS specially designed for each experiment.

This thesis is about experimentally quantifying the radiation damage on a depleted monolithic active pixel sensor, which is a potential candidate for future upgrades of the ATLAS experiment. The outermost layer was targeted as the first milestone not only because of the lower radiation doses, but also because it has the largest surface area, hence it is going to be most cost effective to replace with monolithic devices.

Chapter 2

Silicon pixel detectors

In this chapter the operation principle of silicon detectors used in particle physics is described. The chapter begins with the interaction of the particles with the silicon material, then continue to the signal generation and readout. It finishes with a description of radiation damage in silicon and its effect on signal generation and readout.

2.1 Interactions of particles with silicon

As protons collide in the LHC with 13 TeV centre-of-mass energy, they create multiple particles with lower total energy. Some of them have will ionise the material they are passing through and hence would be detectable by silicon. The silicon detector would be used to detect charged particles, as they can go through multiple layers of silicon and produce enough measurement points that their trajectory can be reconstructed.

2.1.1 Charged particles

As charged particles pass through a material, they excite or ionise the bound electrons of that material. Doing that, they lose part of their kinetic energy. As energy loss is susceptible to stochastic processes and the possible ionization by secondary electrons, the mean energy loss is considered. The parameter used to describe this ionisation in the material is called stopping power and is defined by the average

energy loss of the particle over a certain distance - $\langle \frac{dE}{dx} \rangle$. Assuming only ionisation as the energy loss process, the stopping power can be numerically calculated by the Bethe-Bloch formula [88]:

$$-\left\langle \frac{dE}{dx} \right\rangle = 4\pi N_A r_e^2 m_e c^2 \rho \frac{Z}{A} \frac{z^2}{\beta^2} \left\{ \ln \left(\frac{2m_e c^2 \beta^2 \gamma^2 W_{max}}{I^2} \right) - \beta^2 - \frac{\delta(\beta\gamma)}{2} \right\} \quad (2.1)$$

where A the atomic mass number, r_e is the classical electron radius, m_e the mass of the electron, N_A is Avogadro's constant, z is the charge of the incoming particle in units of electrons, I is the mean excitation potential, Z is the atomic number of the absorbing material, W_{max} the maximum amount of kinetic energy that can be transferred in a single collision, δ is the density-effect correction and ρ is the density of the material. This formula is valid in the region of $0.1 \leq \beta\gamma \leq 1000$ for particles heavier than the electron. Due to the small mass of the electron, there are additional terms that need to be added to the formula to account for Bremsstrahlung and electron-electron interactions in the material.

Figure 2.1 illustrates the stopping power per unit density (mass stopping power) of a charged particle. The region where there is a minimum in the stopping power is known as minimum ionisation and particles with mass stopping power close to the minimum are known as Minimum Ionisation Particles (MIPs). The value of the MIP mass stopping power is 1.664 MeV g^{-1} cm^2 and is roughly similar for materials with atomic number $10 \leq Z \leq 30$. Since the region where $1 \leq \beta\gamma \leq 1000$ is relatively flat, that value is relevant for the detection of particles with silicon detectors.

This thesis focuses on relatively thin detectors (a few 100 μm at most). For this geometry a good model for the energy loss fluctuations is the Landau-Vavilov model [50]. It describes the probability distribution of energy loss in a thin detector, as shown in Figure 2.2. The width of the Landau distribution depends on the thickness of the detector. The tail at high energy comes from the probability of large single-collision energy losses or production of secondary δ-electrons that start ionising as well. The mean energy loss per unit distance traversed is not a well defined number, as the distribution is heavy-tailed. Therefore a more useful commonly used quantity is the most probable value (MPV).

The Landau probability distribution function is given by Equation 2.2, where η is a scaling factor and μ is the location of the peak [99].

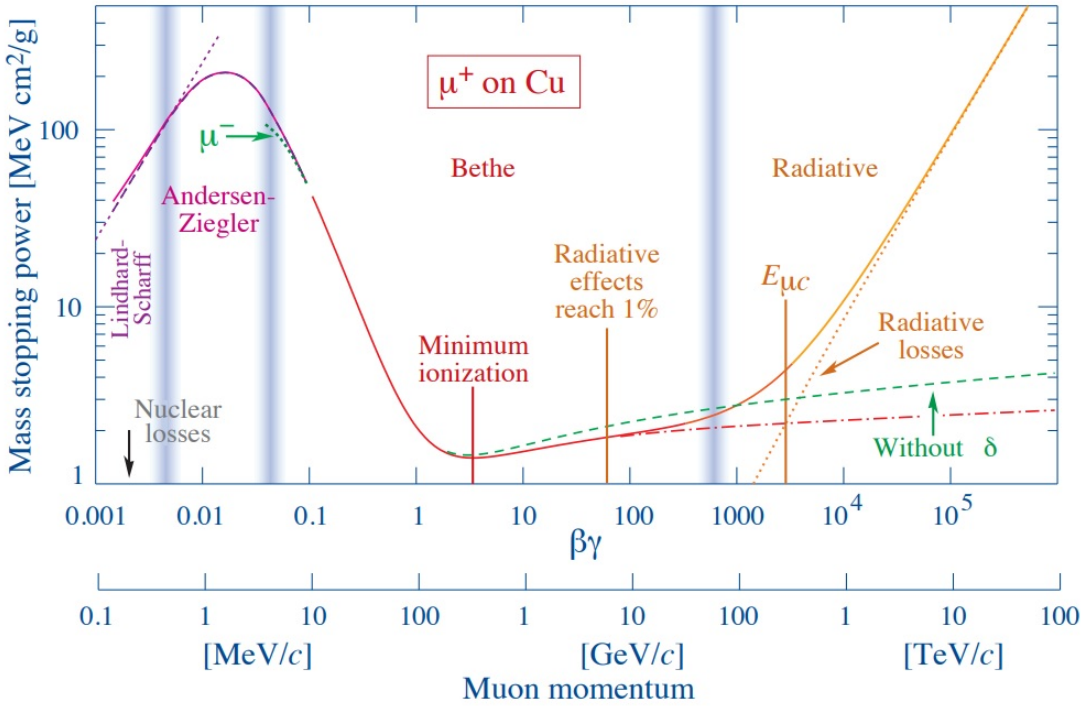


Figure 2.1: Mean energy loss of a muon passing through copper. Taken from the Particle Data Group (PDG) [88].

$$f(x;\mu,\eta) = \frac{1}{\pi\eta}\int_0^\infty e^{-t}\cos\left(t\left(\frac{x-\mu}{\eta}\right)+\frac{2t}{\pi}\log\left(\frac{t}{\eta}\right)\right)dt \tag{2.2}$$

The parameter that is easily measurable and identifiable is the Landau peak and its position. The position refers to a value that represents the most probable energy loss per unit distance (Δ_p/x). In Landau's model the most probable energy loss is calculated as:

$$\Delta_p = \xi\,[ln(\frac{\xi}{I}) + ln(\frac{2m_ec^2\beta^2\gamma^2}{I}) + j - \beta^2 - \delta(\beta\gamma)] \tag{2.3}$$

where $\xi = (2\pi N_A r_e^2 m_e c^2/2)\langle Z/A\rangle z^2(x/\beta^2)$ with x being the detector thickness multiplied by the material density (measured in g cm^{-2}), $j = 0.200$ and all the other parameters are the same as in Equation 2.1 [88]. This means that $\Delta_p/x = a\,ln(x)+b$ where a and b are constants. The logarithmic dependence can be seen in Figure 2.2, but since the detectors used in the thesis are thin and are roughly the same thickness, it is approximated that $\Delta_p/x \sim const$. The value of this proportionality constant would depend slightly on the energy and type of the particle, but it would be similar for particles with momentum near or above the MIP range. Figure 2.3 shows the behaviour of $\Delta_p/x \sim const$ for particles with different energies with respect to the

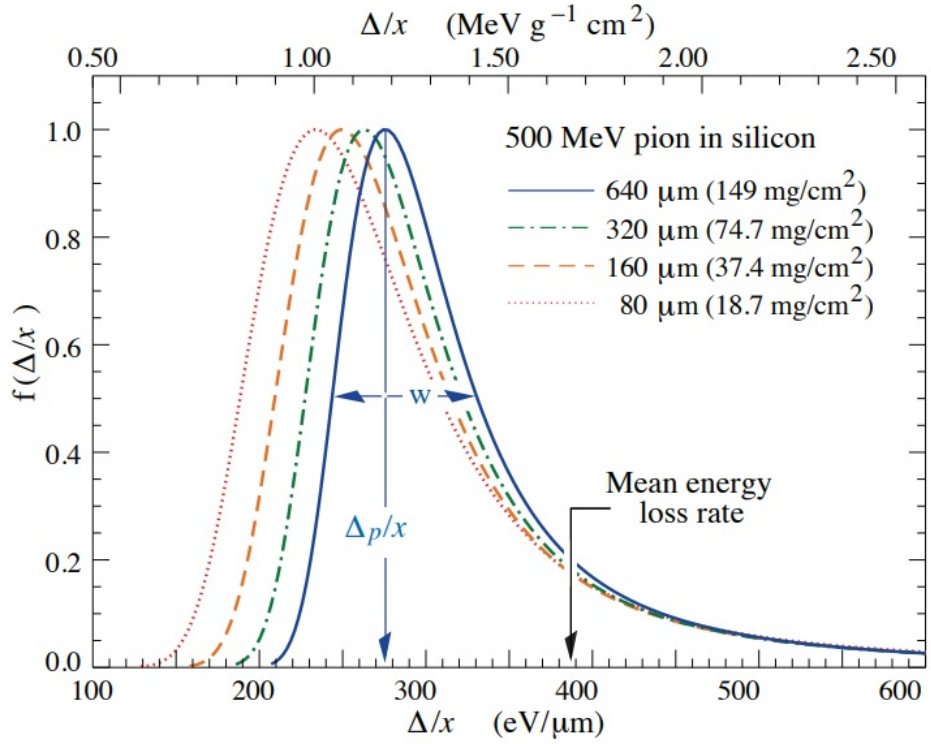


Figure 2.2: Landau distributions from a 500 MeV pion interacting with different thicknesses of silicon. The distributions are scaled so that the most probable value is 1 [88].

minimum ionisation energy.

A convenient and widely used source of MIPs is Strontium-90 (^{90}Sr). It is a radioactive source that emits β^- radiation with a half-life of ~ 28 years. It has two decay channels of energy level differences 0.546 MeV and 2.274 MeV. They both produce electrons close to the minimum ionisation energy, but the lower energy one is more prominent due to its shorter lifetime [41]. Considering that this is a three-body decay as there is an extra antineutrino emitted, most electrons carry energies lower than the energy level difference. If we assume that the kinetic energy of the electrons is around half the level difference, we estimate that an electron from that channel has $\beta\gamma \sim 1.5$. Since the MIP stopping power for silicon is 3.9 MeV/cm [88], this leads to $\Delta_p/x \approx 280\,\text{eV}/\mu\text{m}$ [32]. Usually the value is shown in terms of electron-hole pairs per micrometer (described in detail in subsection 2.2.3) and the conversion factor is 3.69 eV/e^- [36], so that results in $\Delta_p/x \approx 76\,e^-/\mu\text{m}$.

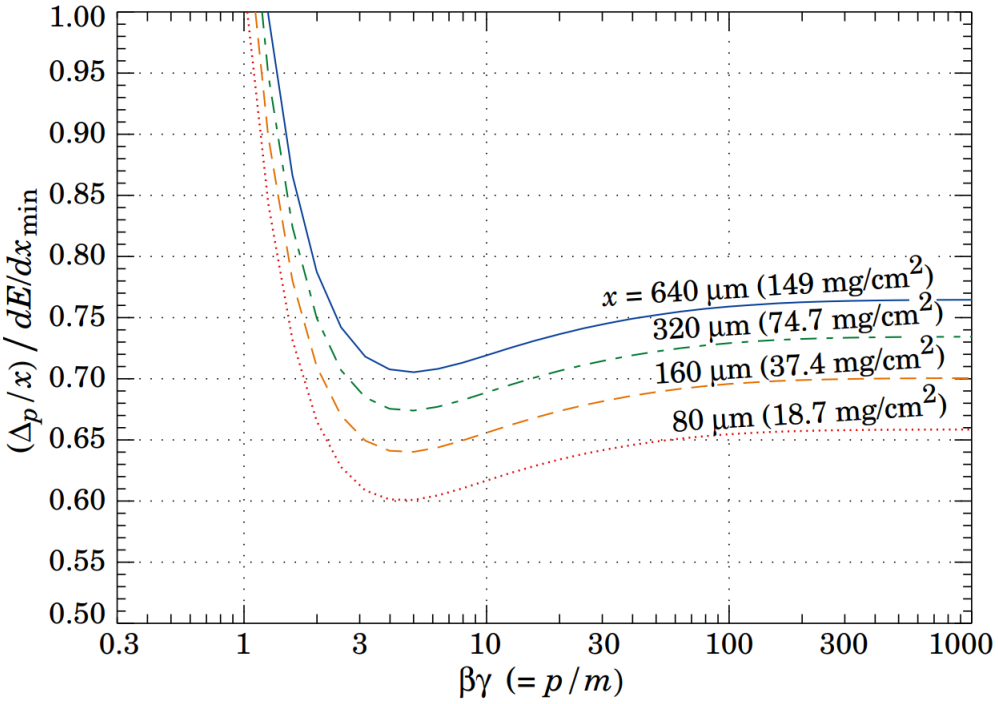


Figure 2.3: Most probable energy loss per μm for particles in silicon in the MIP region. The graph is scaled to the mean energy loss of a MIP in silicon. Figure is adapted from [88].

2.1.2 X-ray photons

The interaction of X-ray and gamma photons with matter occurs via the electromagnetic force. The main processes by which a photon can lose its energy in matter are the photoelectric effect, Compton scattering and pair production. These processes become dominant and different energies and their impact depends also on the Z of the materials as seen by Figure 2.4.

The photoelectric effect happens when a photon is absorbed by an atom leading to an energetic electron being emitted. The kinetic energy of the outgoing electron is the difference between the incoming photon energy and the binding energy of that electron. At higher incoming energy and lower Z, Compton scattering starts to become dominant. Compton scattering is an inelastic scattering of the photon with an electron. Part of the energy and momentum of the photon is transferred to the electron. If the photon has energy more than double the mass of the electron (1.022 MeV), then that the photon can turn into an electron-positron pair.

Photons going through a material have some probability of undergoing some of the aforementioned processes. A beam of photons will be attenuated as it passes

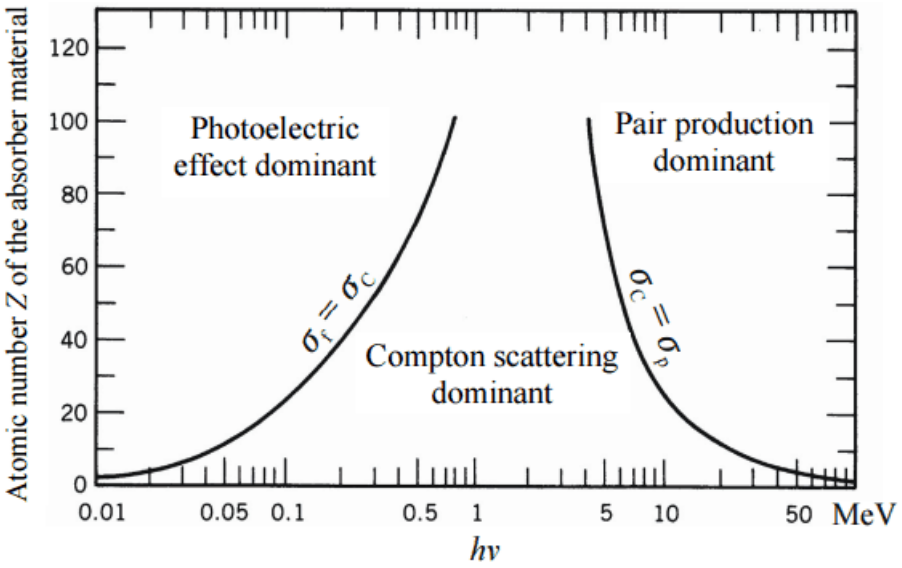


Figure 2.4: The dominant energy loss processes for X-rays and gamma rays at different energies ($h\nu$) and for different atomic numbers (Z). [27]

.

through the material. Since the rate of the interactions happening is proportional to the number of photons, the attenuation of the intensity of a beam is described by the following:

$$I(x) = I_0 e^{-\mu x} \tag{2.4}$$

where I_0 is the initial intensity and μ is the attenuation coefficient, which depends on energy and material type. Calculated and verified datasets for the attenuation coefficient are available at the NIST database [84]. The one for silicon can be seen in Figure 2.5. The attenuation coefficient for silicon increases by several orders of magnitude for photon energies < 100 keV. Therefore silicon is almost transparent at photon energies > 100 keV. Since most silicon sensors are not thicker than a few hundred micrometers, a rough upper energy boundary for detectable X-rays in silicon is 20 keV. In this energy range, the dominant process for silicon is the photoelectric effect, which is three orders of magnitude larger than Compton scattering and pair production [64]. The ejected photoelectron has enough energy to travel a distance roughly $\sim 1\,\mu$m [35]. This is more than an order of magnitude smaller than the thickness and pixel pitch of most silicon detectors, including the sensors that will be described in this thesis. Therefore for silicon, the interaction of detectable photons with the material is modelled as a photon stopping and depositing all of its energy in a certain point, creating a cloud of electrons from ionisation, which are then swept away by an electric field to generate a signal (more detail in subsection 2.2.3).

2.2 Principles of p-n junctions

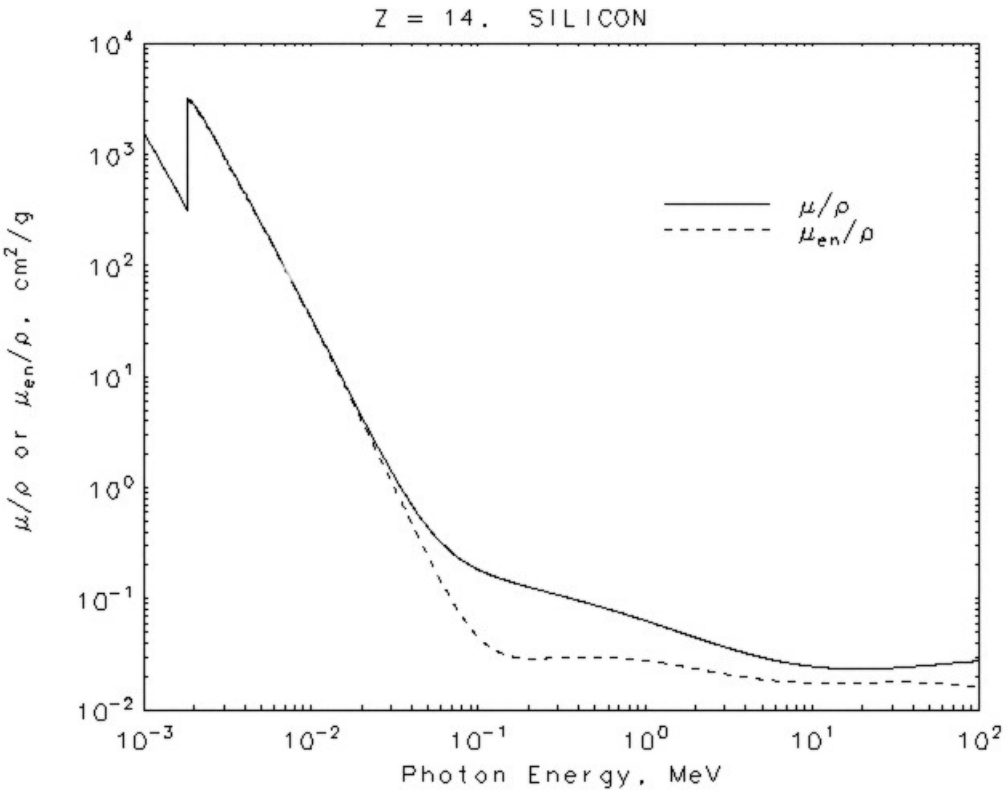


Figure 2.5: The mass attenuation coefficient (μ/ρ) and the mass attenuation energy-absorption coefficient (μ_{en}/ρ) as a function of energy of the incident photon for silicon [84].

In this section the basic properties of semiconductors are going to be described. Most of the principles overlap with other semiconductor materials, but the thesis is focused on silicon.

2.2.1 Semiconductor production

Band gap model

When atoms are bound closely in a lattice, their orbits might partially overlap. The energy levels of the single atom orbit shift and hence they are separated into two energy bands which electrons can occupy - the conduction band and the valence band. The occupancy of each band is temperature dependent and is described by the Fermi-Dirac distribution. An important parameter in the model is the Fermi level - the energy level at which the occupancy probability is one half. At 0 K the

Fermi level is the upper limit on the occupied energy levels, but as the temperature increases thermal energy may excite electrons to go from the valence to the conduction band as shown in Figure 2.6. The electrons in the conduction band can move freely, since it is an almost empty band.

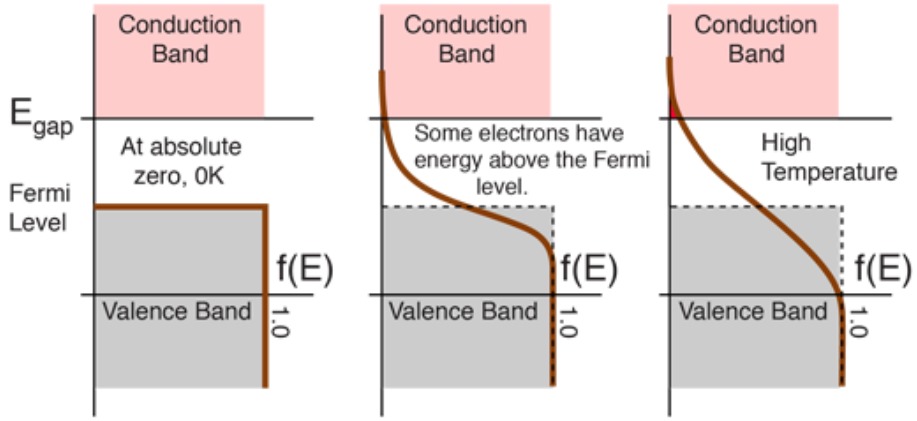


Figure 2.6: The conduction and band gap at increasing temperature. The solid line represents the occupancy probability f(E) at different energy levels. [39].

The energy gap between the conduction and valence band is known as band gap. Depending on the band gap the materials can be separated into three types - conductors, insulators and semiconductors. In conductors the conduction and the valence band overlap, hence the charge carriers can move freely. Insulators have a large band gap and no electron from the valence band can get enough energy to reach the conduction band. Semiconductors have a small band gap (1.12 eV for Si [64]), which allows for excited electrons to jump from the valence band to the conduction band. As an electron is in the conduction band, there is a space for one electron open in the valence band, which is called a hole. The hole can move freely and transfer positive charge. It is possible for an electron from the conduction band to fill the space of that hole and that process is known as recombination. The concentration of electrons in the conduction band (n) and the concentration of holes in the valence band (p) are be equal for all temperatures for intrinsic (non-doped) silicon. The intrinsic carrier concentration (n_i) is defined as [20]:

$$n_i^2 = n.p = N_C N_V exp\left(\frac{-E_g}{2kT}\right) \tag{2.5}$$

where N_C and N_V are the total number of states in the conduction and valence band respectively and E_g is the band gap energy.

Silicon doping

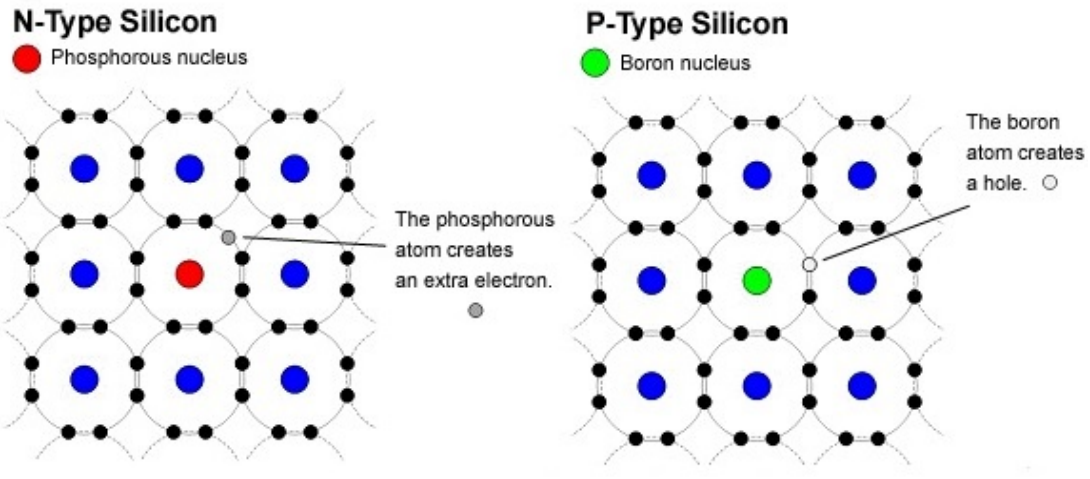


Figure 2.7: A sketch of a n-type and p-type doped silicon, with the impurities marked in red and green respectively [62].

Silicon doping is the process of replacing some silicon atoms with impurity atoms. There are 4 valence electrons in the outermost shell of Si, so the most common dopants are with 5 or 3 outer shell electrons (examples are phosphorous (P) and boron (B)). In the example of phosphorous, the extra electron is very loosely bound to the phosphorous nucleus and goes into the conduction band at very low temperatures. This is called n-type silicon. Similarly for p-type silicon the atoms are called acceptors and there is an extra hole near the valence band created. An illustration of doping is shown in Figure 2.7.

The effect of doping is that the Fermi level shifts towards the conduction or valence band for the n-type or p-type respectively. There are additional states at the donor or acceptor energy level, which at 0 K are filled with their respective charge carriers, but at higher temperatures are within the bands, as shown in Figure 2.8.

Semiconductors properties can be modified by doping small regions of that bulk with different concentration dopants. Those regions of different high concentration doping are called implants.

2.2.2 Depletion region

When n-type and p-type silicon are brought together a p-n junction is formed. The most common property and usage of that junction is that current can flow from the

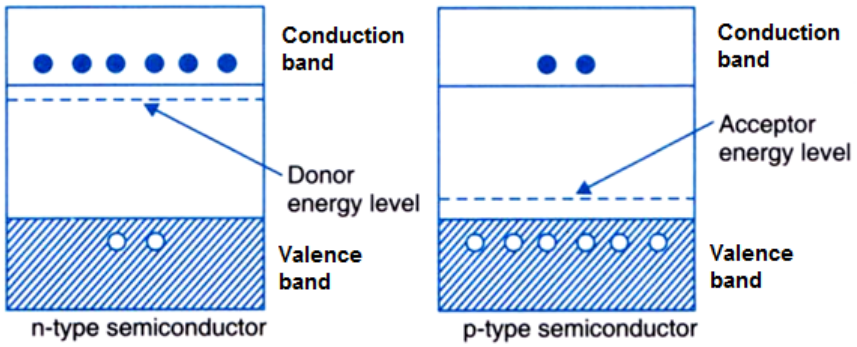


Figure 2.8: Band gap structure of n-type (left) and p-type (right) doped silicon with their donor and acceptor levels shown [97].

p-type silicon to the n-type, but not backwards.

Thermal equilibrium

When the p-type and n-type silicon can exchange charge carries, thermal diffusion takes place. The charge carriers make their way into the opposite type silicon and recombine there. The recombination introduces charge to the immobile atoms - negative charge in the p-type and positive charge in the n-type region as shown in Figure 2.9. This creates a potential difference that opposes the diffusion. Thermal equilibrium is reached when the potential difference from the fixed charges is large enough to stop the charge carriers diffusing through the junction. The effect is that there is a region where there are no charge carriers and an electric field is present. That region is known as depletion region.

To calculate the in-built potential difference (ΔV) or the size of the depletion region (D) we need to solve Poisson's equation for the potential $\varphi(x)$:

$$\frac{d^2\varphi(x)}{dx^2} = -\frac{\rho(x)}{\epsilon_0\epsilon_r} \tag{2.6}$$

where $\rho(x)$ is the charge density and ϵ_r is the relative permittivity of the material, equal to 11.68 for Si. Integrating this equation yields the distribution of the electric field ($E(x)$). Let $x = 0$ be the position of the junction boundary. If we denote N_a and N_d as the concentration of acceptors and donors respectively, while d_p and d_n are the extents of the depletion region in the p-type and n-type silicon, the solution for the electric field is [93]:

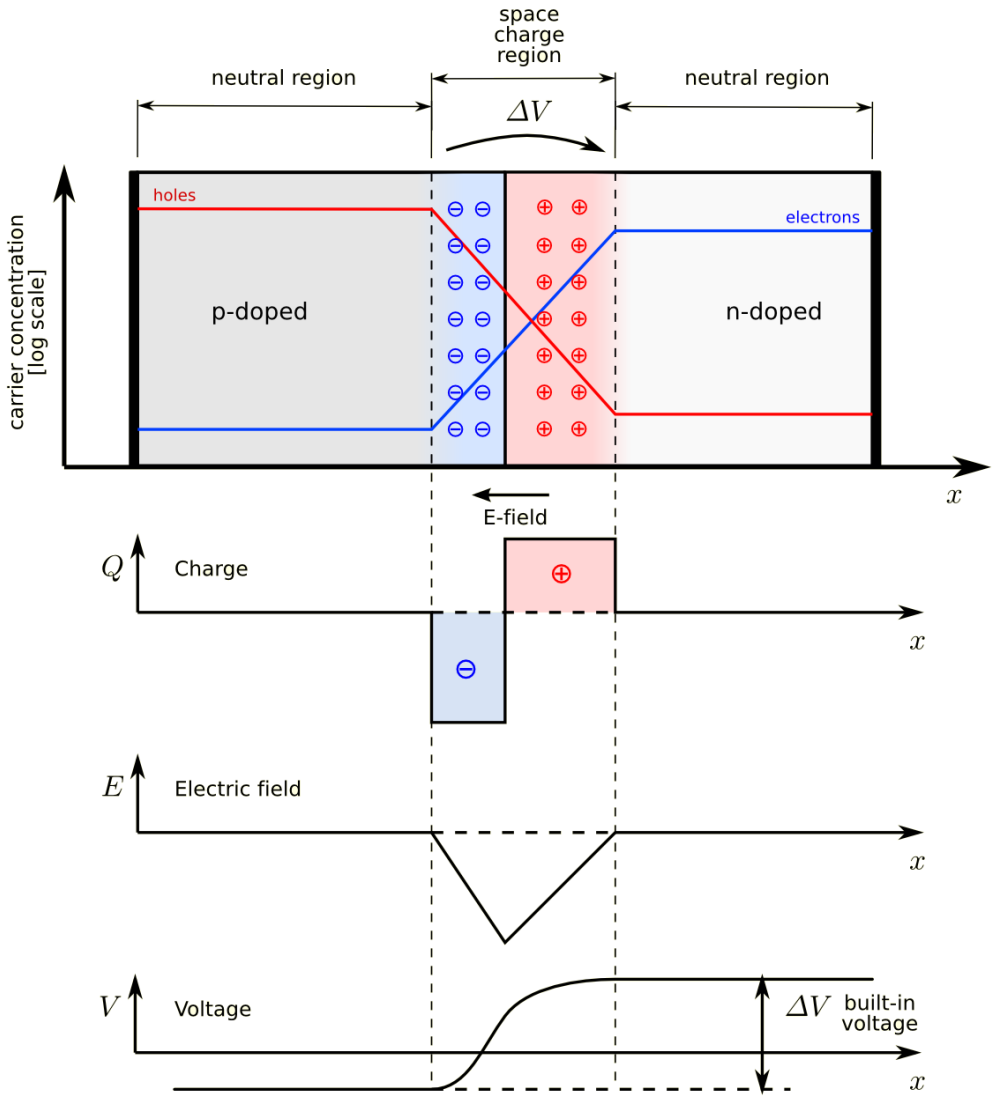


Figure 2.9: N-type and p-type silicon forming a depletion region. Below are graphs of the charge, electric field and potential as they change along the junction length. [73].

$$E(x) = \begin{cases} \dfrac{-eN_a}{\epsilon_0 \epsilon_r}(x + d_p) & \text{for the p-doped region x<0} \\ \dfrac{eN_d}{\epsilon_0 \epsilon_r}(x - d_n) & \text{for the n-doped region x>0} \end{cases} \tag{2.7}$$

The continuity condition and the junction boundary ($x = 0$) gives the relation:

$$N_a d_p = N_d d_n \tag{2.8}$$

Integrating the electric field yields the potential with a negative sign ($E = -\nabla\varphi$).

Since there is no physical condition that sets the integrating constant, it is chosen to be such so that the potential at the boundary is 0 ($\varphi(0) = 0$) and the solution becomes:

$$\varphi(x) = \begin{cases} \frac{eN_a}{\epsilon_0\epsilon_r}(x^2 + xd_p) & \text{x<0} \\ \frac{-eN_d}{\epsilon_0\epsilon_r}(x^2 - xd_n) & \text{x>0} \end{cases} \tag{2.9}$$

Plugging in the positions at the boundaries and using Equation 2.8, the expression for ΔV becomes:

$$\Delta V = \varphi(d_n) - \varphi(-d_p) = \frac{e}{2\epsilon_0\epsilon_r}(N_d d_n^2 + N_a d_p^2) = \frac{e}{2\epsilon_0\epsilon_r} N_d d_n (d_n + d_p) \tag{2.10}$$

The total depletion depth D can be related to d_n using Equation 2.8:

$$\begin{aligned} D = d_n + d_p &= d_n \left(1 + \frac{N_d}{N_a}\right) \\ \therefore \qquad d_n &= D\frac{N_a}{N_a + N_d} \end{aligned} \tag{2.11}$$

Plugging Equation 2.11 into Equation 2.10, a formula for the total depletion region is derived [96].

$$D = \sqrt{\frac{\Delta V 2\epsilon_0\epsilon_r}{e}\left(\frac{1}{N_d} + \frac{1}{N_a}\right)} \tag{2.12}$$

Reverse biasing

The fact that there are no free charge carriers within the depletion region, means that it can be used to detect charged particles or photons (described in more detail in subsection 2.2.3). The typical silicon depletion region from diffusion would extend a few micrometers, which is small relative to the usual sensor size. Since the signal collected from a particle depends strongly on the size of the depletion region, the depletion depth is externally extended by applying a voltage directed from the n-type to the p-type silicon.

The two modes of operation of a p-n junction are called forward biasing and reverse biasing. Forward biasing is the when the positive voltage is applied on

the p-doped region, so this counteracts the intrinsic electric field and lets current flow through the junction. Reverse biasing is the mode, which is used for particle detection. In that mode the external voltage reinforces the electric field making the depletion region larger. With external biasing the depletion depth is given by:

$$D = \begin{cases} \sqrt{\frac{(V_{external} + \Delta V) 2\epsilon_0 \epsilon_r}{e} \left(\frac{1}{N_d} + \frac{1}{N_a} \right)} & if\ V_{external} + \Delta V > 0 \\ 0 & if\ V_{external} + \Delta V < 0 \end{cases} \tag{2.13}$$

In most silicon pixel sensors, the p-n junction forms between a small implant and the silicon bulk. Thus most of the depletion region is either within an n-type or p-type silicon. Thus an effective doping of $|N_{eff}| = |N_d - N_a|$ is used. For the examples in the thesis, the p-n junction starts from an n-type implant into a p-type substrate. This means that $N_a >> N_d$, which makes the equation for the depletion region:

$$D = \begin{cases} \sqrt{\frac{(V_{external} + \Delta V) 2\epsilon_0 \epsilon_r}{e} \frac{1}{|N_{eff}|}} & if\ V_{external} + \Delta V > 0 \\ 0 & if\ V_{external} + \Delta V < 0 \end{cases} \tag{2.14}$$

Resistivity (ρ) is connected to impurity concentration by [93]:

$$\rho = \frac{1}{e\mu |N_{eff}|} \tag{2.15}$$

where μ is the mobility discussed in subsection 2.2.3. Using that, the depleted region equation in reverse bias becomes:

$$D = \sqrt{(V_{external} + \Delta V) 2\epsilon_0 \epsilon_r \mu \rho} \tag{2.16}$$

Capacitance of the junction

The capacitance of the p-n junction is due to the electric field created by the charge gradient in the depleted region. Hence it depends on the applied reverse biasing voltage. A simplified model is assumed where the junction is approximated as a parallel plate capacitor. Then the equation for the capacitance becomes:

$$C = \frac{\epsilon_0 \epsilon_r A}{D} = A\sqrt{\frac{e\epsilon_0\epsilon_r}{2(\Delta V + V_{external})}\frac{N_a N_d}{N_a + N_d}} \tag{2.17}$$

From the equation it can be seen that the capacitance is reduced for lower doping concentrations, higher bias voltage and smaller area (A).

These are the main characteristics of a p-n junction that are used in this thesis. It is also possible to create a junction with the same type of doping, but different concentrations. For example a high doped n-implant (n^+) in a low doped (n^-) bulk. This junction would have similar characteristics as a normal p-n junction, but the charge gradient creating the electric field would be smaller.

2.2.3 Signal generation

When a charged particle or photon ionizes atoms, it moves an electron from the valence band to the conduction band creating an electron-hole pair. Since the electron is a fermion, it follows the Pauli exclusion principle that two fermions cannot be in the same quantum state. Therefore a factor to account for the available states is added, called density of states ($\rho(E)$). The more energetic particles have more states available with the relation $\rho(E) \sim \sqrt{E} \sim p$, where p is the particle momentum [79]. The minimum energy required to jump across to the conduction band is the band gap energy, which for silicon is 1.12 eV. However, considering the availability of states, there will also be momentum transfer, which increases the mean pair creation energy. Thus the energy that does not create electrons, emits phonons, which leads to an average electron-hole pair creation energy of 3.69 eV [36].

When the particles are free to move, they are affected by the external or internal electric field and start to move along the field lines. This movement is called drifting. In constant electric fields that are less than < 100 kV/cm [80], the charge carriers are considered to have a constant mobility with magnitude estimated by the mobility parameter μ. The mobility gives the relationship between the drifting velocity and the applied electric field and is different for electrons (μ_e) and holes (μ_h).

$$v_{drift} = \mu_{e/h}\, E \tag{2.18}$$

Shockley-Ramo theorem

When a charge is moving towards an electrode, it induces current into that electrode, which is the signal that is detected. The current starts as soon as the charge is created and is moving and stops when the charge has stopped, recombined or has reached the electrode. The equation that allows the calculation of the induced current is the Shockley-Ramo theorem [86]:

$$I_{induced} = q\vec{v} \cdot \vec{E_w} \tag{2.19}$$

where q is the value of the moving charge, $\vec{v}$ is its velocity and $\vec{E_w}$ is the weighting field (unrelated to the actual electric field). The weighting field is a virtual field calculated when the charge is removed, a potential of 1 V is applied to the collecting electrode and 0 V to all other electrodes.

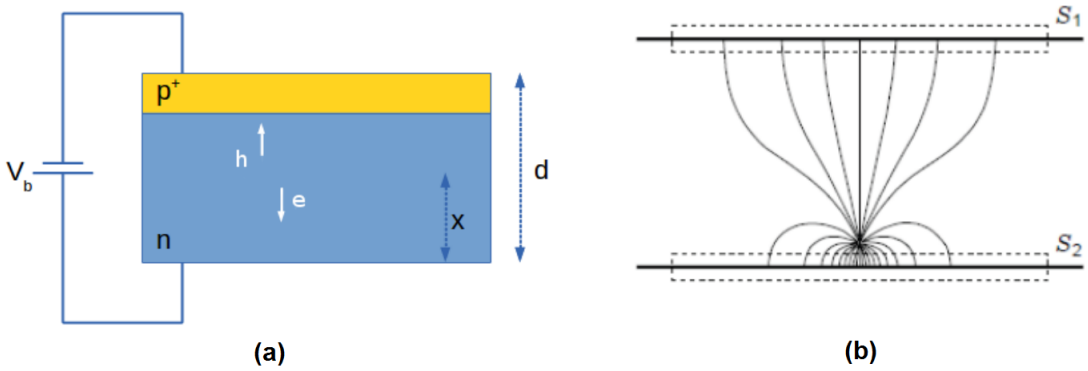


Figure 2.10: (a) a schematic of a reverse biased p-n junction with the anode and cathode considered to be the only electrodes and an electron-hole pair created at a distance x from the anode. (b) a schematic of the electric field lines that induce charge on the electrodes [26].

A simple model with two electrodes can be considered for the p-n junction with reverse bias voltage applied [26]. If an electron-hole pair is created at a distance x from the anode, the hole and electron would start to drift in opposite directions. There will be electric field lines that induce the charge in the electrodes Figure 2.10. Since the detector is thin, the electric field can be approximated to be flat and then the drift velocity becomes:

$$v_{drift} = \mu E = \mu \frac{V_b}{d} \tag{2.20}$$

Therefore, the induced current on the anode from a single charged particle is:

$$I_{induced} = evE_w = e\,\mu\frac{V_b}{d}\,\frac{1}{d} \tag{2.21}$$

The electron and the hole both contribute to the total induced charge, but they have different mobilities and travel different distances. So the travel times for each are:

$$\tau_e = \frac{x}{v_e} = \frac{xd}{\mu_e V_b} \tag{2.22}$$

$$\tau_h = \frac{d-x}{v_h} = \frac{(d-x)d}{\mu_h V_b} \tag{2.23}$$

Therefore using $Q(t) = \int_0^T I_{induced}(t)dt$ the total charge induced on the anode from the electron and the hole is:

$$Q_e = e\,\mu_e\frac{V_b}{d^2}\,\tau_e = e\frac{x}{d} \tag{2.24}$$

$$Q_h = e\,\mu_h\frac{V_b}{d^2}\,\tau_h = e(1-\frac{x}{d}) \tag{2.25}$$

Since charge is conserved, when summing them we get $Q_e + Q_h = e$. Thus the electron-hole pair produces a charge of one electron charge (e^-) on the collecting anode if it does not recombine along the way. Thus if the focus is not the mechanics of the collection, the electron-hole pair signal is normally referred to as collected and the units used are number of electrons (e^-). Using the 3.69 eV on average for an electron-hole pair creation and the most probable ionisation deposition energy to be 278 eV/μm, the most probable signal collected is 76 e^-/μm [32].

Diffusion

If there is no electric field applied, electrons and holes would not drift. They will begin to diffuse, scattering from silicon lattice and impurity atoms. For silicon the mean distance between scattering is $\sim 0.1\mu$m. Due to the completely random nature of diffusion, the net movement of a particle is zero. However, when a trace of electron-hole pairs is created when a MIP passes through, a carrier concentration gradient is created. The carriers follow the gradient, which results in a non-zero

net travel and non-zero current [61]. The diffusion current density depends on the diffusion constant D the following way:

$$J_{diffusion} = qD\nabla n \tag{2.26}$$

where q is the charge of the carriers and ∇n is their concentration gradient. The diffusion constant can be calculated using the Einstein relation:

$$D_{e/h} = \frac{kT}{q}\mu_{e/h} \tag{2.27}$$

2.2.4 Shockley diode model

The p-n junction can be operated in forward bias mode, which is normally labeled with positive voltages and reverse bias mode, where negative voltages are used. The current-voltage dependence (normally called an IV curve) can be approximated by the Shockley diode equation:

$$I(V) = I_S[exp\left(\frac{qV}{\eta kT}\right) - 1] \tag{2.28}$$

where I_S is the saturation current in reverse bias mode, T is the temperature, k is Boltzmann's constant and η is a dimensionless ideality factor that is 1 for an ideal diode. A graph of a diode I-V can be seen in Figure 2.11.

In forward biased mode, the diode becomes fully conductive very quickly. A typical value for the voltage drop (V_0) over a diode while its conducting is $\sim$ 0.6 V for silicon, but that value can change for custom made diodes within a chip. In reverse bias mode, there is a small amount of current flowing through the p-n junction even if there is no signal being generated within the depletion region. That current is called leakage current. Increasing the reverse bias would eventually lead to breakdown, where the diode becomes conductive even in reverse bias mode.

Leakage current

The main source of the leakage current are charge carriers created from thermal excitations in the depleted region. Therefore the volume of the depleted region is

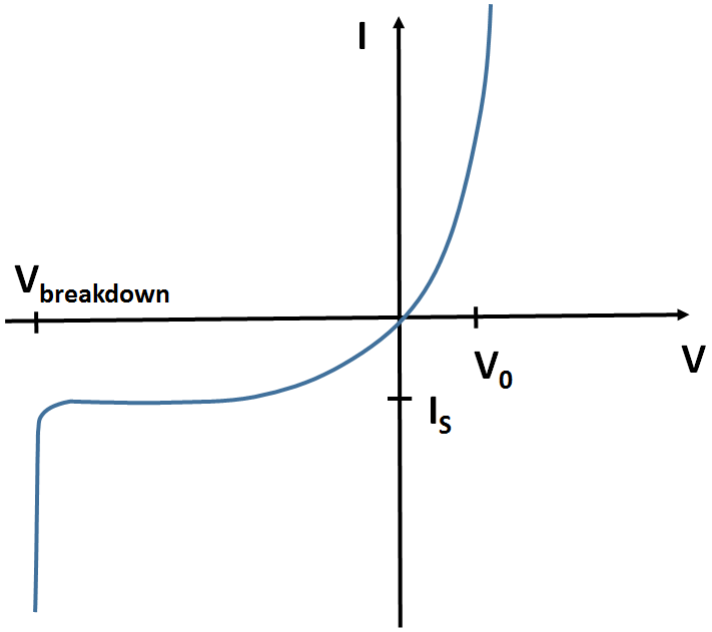


Figure 2.11: Current-voltage dependence for a diode following the Shockley equation and its breakdown voltage. I_S is the saturation current while being reverse biased and V_0 is the typical voltage drop in forward bias mode.

proportional to the leakage current. Because of its origin, the leakage current is strongly temperature dependent following the equation [20]:

$$I_{leakage}(T) \sim T^2 exp\left(\frac{-E_g(T)}{2kT}\right) \tag{2.29}$$

It is possible for charge carriers from the non-depleted regions to diffuse into the depleted region and produce current. This contributes to the total leakage current. Other contributions include currents from surface and edge effects that originate from the p-n junction layout and processes used to create it [61].

In an experimental setup with a photosensitive silicon detector, background light is a major source of leakage current and is indistinguishable from other sources. For this reason most measurements are made with the devices in the dark, but there will always be some visible or non-visible light leak.

Breakdown

When the reverse bias voltage is too high, breakdown will occur. The mechanisms that can cause it are referred to as thermal instability, avalanche multiplication or Zener breakdown [20].

Thermal instability occurs when there is a random local rise in temperature, which increases the leakage current. The energy dissipation from the leakage current increases the temperature even more, which creates a feedback loop causing the p-n junction to conduct a large current. To reduce this effect, the detectors are normally operated and very low temperatures. In avalanche multiplication an energetic electron knocks out another one from the valence band, the electrons gain kinetic energy due to the field and knock more electrons. If the doping and size of the sensors are suitable, this multiplicative process continues and makes the sensor conductive in reverse bias mode. The Zener breakdown occurs when the electric field within the junction is high enough that increases the probability of charges to tunnel from the valence to the conduction band.

2.3 Types of silicon pixel sensors

When multiple p-n junctions are put next to each other on a piece of silicon, a silicon pixel detector chip is created. There are two main schemes of extracting the information from each pixel. The one used in charge-coupled devices (CCDs) consists of having 1 readout pixel at a corner of the chip. The gathered charges are being moved to their neighbouring pixel at each clock cycle. The one inputting its charge into the readout pixel, gets its charge converted to a voltage output. The result is one continuous output data line for the charge of each pixel.

The other scheme, which is more common in particle physics, is that every pixel is read out separately. The data is encoded while it is still on the chip and is sent out in packets. This method requires more parallelisation in the readout design, but is capable of maintaining higher data flow. There are two general ways of making such a detector. The most common one, which is currently used, consists of a sensing and a readout part of silicon bonded together. The pixels made that way are called hybrid pixel detectors. The other way is to use one piece of silicon for the readout and the sensing. These type of detectors are called monolithic active pixel sensors (MAPS), but are commonly referred to as CMOS, which is the name of the technological process.

2.3.1 Hybrid pixel detectors

Hybrid pixel sensors consist of two parts - the sensing part and the readout part. This concept originates from silicon strip detectors, but in this case, the sensing part is smaller and has a different orientation. The sensor is a p-n junction, while the readout is an application-specific integrated circuit (ASIC). The electronics that receive, encode and send the signal are located in the ASIC. A sketch of a hybrid pixel detector is shown in Figure 2.12. The sensor and the readout are conductively connected via a solder bump which is $\sim$ 20 μm in diameter. Under bump metallization (UBM) is applied on both parts at the pixel positions for better contact with the solder. The charges created from the particle travel through that bump and are read out in the ASIC. This type of connection is called DC coupled. If the bumps are replaced by a glue layer, then the connection between the sensor and the readout parts is capacitive and that is called AC coupling. Hybrid pixel detectors have been a very successful development and are currently the basis of most tracking technologies in HEP.

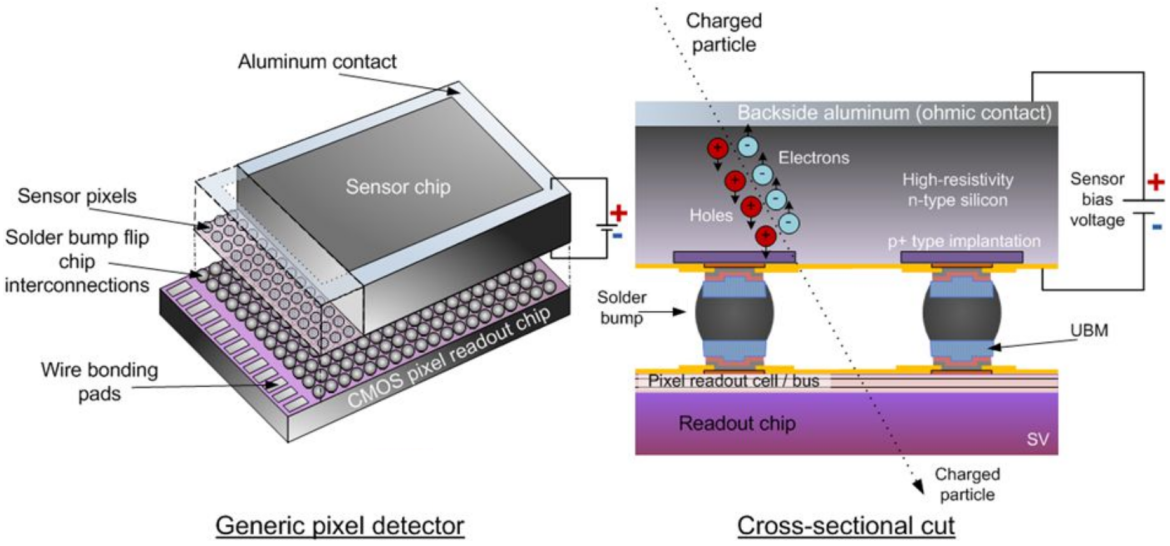


Figure 2.12: Sketch of a hybrid pixel chip. On the left there is a 3D view of the readout chip, the sensor, and the unattached bump bonds. On the right there is a cross-sectional view of the attached hybrid with a particle going through the biased sensor. The signal has to go through the solder bump and the under bump metallization (UBM) to reach the readout chip [93].

2.3.2 Monolithic pixel detectors

Since both sensor and readout are made of silicon, it is natural to try and combine them as it is done in a monolithic active pixel sensor (MAPS), illustrated in Figure 2.13. The main advantage of MAPS is that there is no more need for bump-bonding, which is one of the most laborious and expensive parts of the hybrid production process. Another advantage is that thinner detectors scatter particles less, thus lower material budget is always better for detection. It is also possible to reduce the resolution of the detector since there is no longer the limit of the bump-bond size.

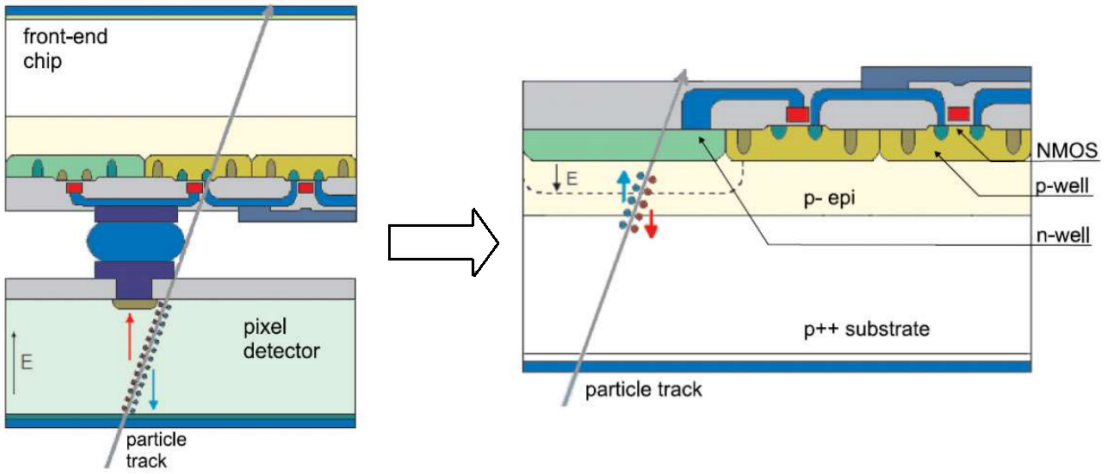


Figure 2.13: A hybrid detector (left) and a monolithic detector (right) [76]

MAPS are commonly referred to as CMOS sensors in HEP, because of their production process. CMOS stands for Complementary Metal-Oxide Semiconductor and consists of two MOS transistors (pMOS and nMOS) transistor linked together. A pMOS (nMOS) transistor consists of two p-type (n-type) implants in n-type (p-type) silicon. The utilization of the pMOS and nMOS transistors is custom for HEP detectors, but they are produced in the same way. The production processes have been developed in CMOS foundries, where other commercial devices (micro-controllers, microprocessors, cameras, memory chips etc), as well as ASICs for the readout hybrid detectors, are manufactured. The exact steps in the CMOS process to produce a device are normally a trade secret for each foundry. The two most common types of CMOS processes used to produce HEP detectors are the high voltage and high resistivity CMOS processes - HVCMOS and HRCMOS.

HVCMOS

In the HVCMOS process, a large highly doped n^{++} implant in p-type silicon produces the p-n junction and hence the depletion region (see Figure 2.14). This is commonly referred to as a deep n-well. The pMOS is shielded from the high voltage and induced currents by an additional p-type layer - p-well. In the case for the nMOS, its own p-type body is providing sufficient shielding.

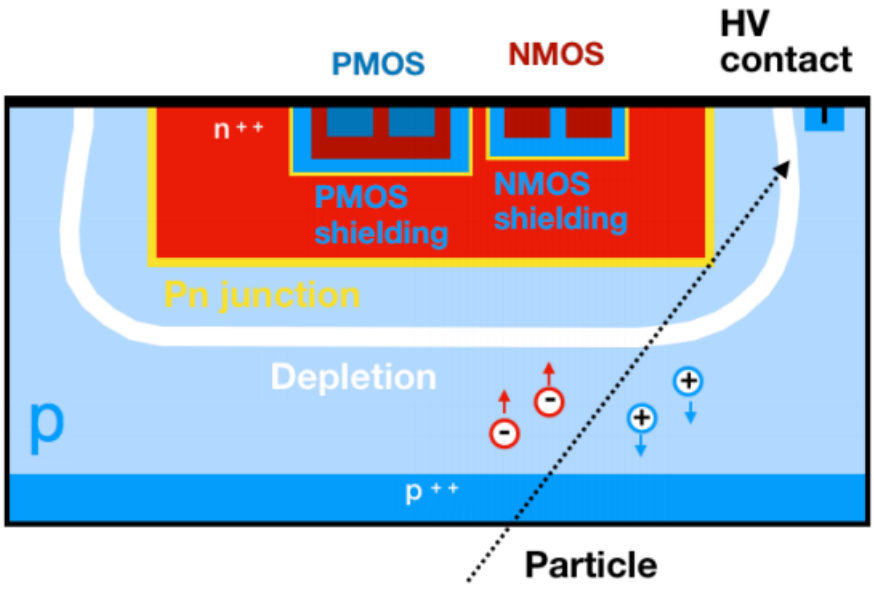


Figure 2.14: A schematic of an HVCMOS process used in HEP [61].

In this design, all the electronics of the pixel readout must fit inside the n^{++} pixel implant. Therefore the size of the collection electrode and the p-n junction is often larger than in a hybrid sensor or in HRCMOS. This makes the sensor capacitance of the p-n junction large, resulting in lower gain per electron, slower rise time and higher noise [61]. As the depletion region grows from the deep n-well, one of the challenges for this technology is to produce a device that allows for enough high voltage applied and has low enough substrate doping that the depletion region reaches the p^{++} substrate at the back of the chip.

HVCMOS prototypes for ATLAS have been fabricated with LFoundry [91] and AMS [68] processes. The most advanced chips from both foundries are LF Monopix [21] and AtlasPix [70] respectively.

HRCMOS

HRCMOS devices are optimized for a small collection electrode, resulting in a small collection capacitance (see Figure 2.15). To prevent loss of the generated electron-hole pairs and shield the electronics, there is a p^{++} layer around the transistors (deep p-well) with a gap in the pixel centre for the collection electrode. Bias voltage is applied to the back substrate and p-wells to expand the depletion region in the lateral direction. The depletion region starts growing from the $n{+}{+}$ implant. There is also a junction from the n-type implants of the nMOS and the p-wells, which sets the upper limit on the voltage applied (which is a few volts).

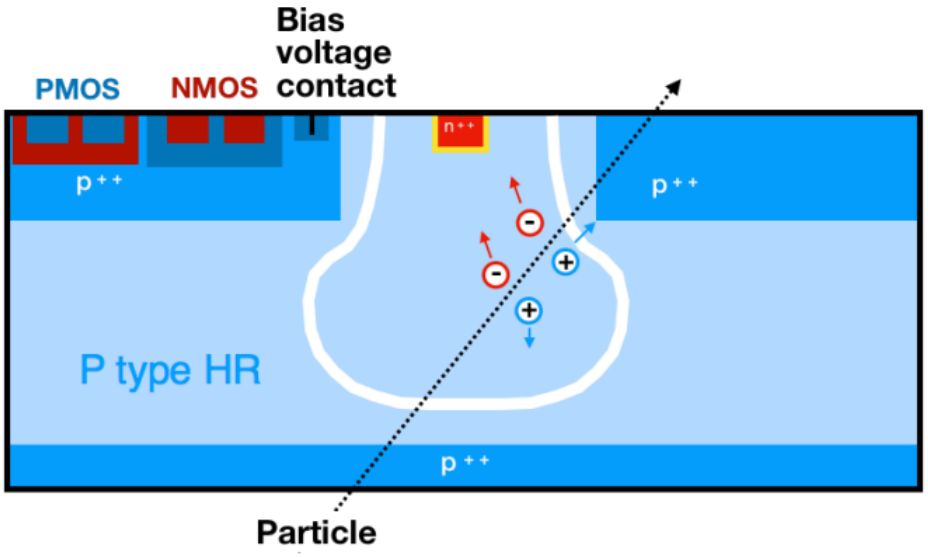


Figure 2.15: A schematic of an HRCMOS process [61].

From equation 2.16, we can see that to reach a large depletion depth with a small bias voltage, a high resistivity substrate is needed. Due to the configuration of the implants, one of the challenges for this type of technology is to achieve a full lateral depletion depth. The lower capacitance of this configuration yields higher gain for the same power consumption, better rise time and lower noise than the HVCMOS. The noise level is low enough that the detection threshold could be placed $\sim 100\,e^{-}$. The higher gain means that less amplification stages are needed. This reduces the power consumption, which affects the amount of material required in a detector due to cooling needs.

This study focuses on the study of ATLAS HRCMOS prototypes produced by the TowerJazz foundry: Investigator, MALTA and mini-MALTA. All these devices are manufactured using the HRCMOS process with modifications to achieve a larger depletion depth and higher radiation hardness, as discussed in section 3.1.

2.4 Radiation damage

The effects of a particle passing through a material depend strongly on the material itself and also on the particle's properties, such as energy, mass, charge, etc. To a first approximation, the radiation damage in silicon can be divided into two groups. The first is Non-Ionizing Energy Loss (NIEL), which causes damage to the silicon bulk, and the second is Total Ionization Dose (TID), which causes damage to the surface and the transition region between different silicon implants.

2.4.1 NIEL

Bulk damage is due to particles displacing silicon atoms from the crystal lattice. The energy needed for this process to occur in silicon is about 25 eV [58]. However since there is a large difference in rest masses between electrons and protons/neutrons, it is a lot easier for the protons/neutrons to deliver that energy to the nucleus. The damage is different between protons and neutrons, but there is an approximate conversion factor and the damage from the protons is converted to equivalent neutron damage. Since this phenomenon is also energy dependent, it is measured in units of 1 MeV neutron equivalents per square centimetre ($n_{eq}cm^{-2}$).

Displacing one silicon atom is classified as a point defect. However, if an atom is displaced, it most likely has enough energy to disturb other atoms around and remove them from their lattice position as well. Most atoms would rearrange back to the original state, but there will be some forming cluster defects. These cluster defects are the more critical ones for detector performance.

There are different ways in which these defects affect the performance of a silicon detector after irradiation. For example, if the defect forms an energy level between the conduction and the valence band, it would act as a recombination centre and thus increase the leakage current through the reverse biased diode. Generating recombination centres causes removal of dopants, but some defects can act as effective dopants. This alters the effective doping and for lower doping concentrations the effective doping type of the implants could change as shown in Figure 2.16. Different effective doping would also affect the resistivity and the depletion depth of the pixel. Trapping centres (or traps) can be a consequence of cluster defects. They trap the charges heading for the collection electrode reducing the amount of charge in the collection electrode, which reduces signal output of the detector.

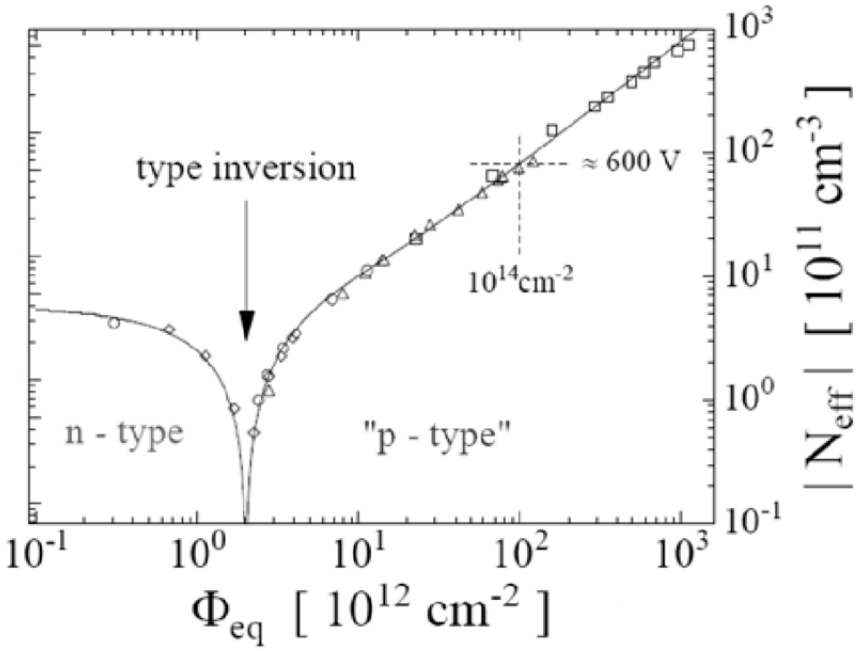


Figure 2.16: Type inversion of an n-type implant to a p-type with increasing 1 MeV neutron equivalent fluence (Φ_{eq}) [83].

2.4.2 TID

The top surface of the chip contains metal layers for data transfer and a silicon dioxide (SiO_2) dielectric in-between them (commonly referred to as oxide). TID affects the dielectric and the boundary between the dielectric and the silicon. Due to the irregular ordering of the atoms in those regions, displacement damage is not as crucial. Ionizing radiation creates electron-hole pairs and a large portion of them immediately recombines. The electrons are quickly collected due to their higher mobility value. The holes go through more material and have a chance to get stuck in an effective trap in the boundary between silicon and the oxide, thus there is a total charge increase in the dielectric. This can cause capacitive coupling between neighbouring pixels, which in turn leads to more charge sharing and higher noise [5].

Clustered charges near the surfaces of thicker oxides can cause additional leakage current. The charge accumulated between two n-type implants (such as an nMOS transistor) may increase its gate threshold voltage for turning off. These problems are commonly mitigated by placing p^+ guard rings around the wells to reduce the leakage current and setting the nMOS transistors within a p^+ well. However, having charge traps near the surfaces inevitably causes additional noise.

2.4.3 Annealing

Annealing in the field of CMOS semiconductor physics is referred to as the process of changing the irradiation effects by increasing the temperature of the damaged device for a period of time. It mainly involves two processes - displacement and migration. The displacement of an atom around a cluster defect can cause a perturbation large enough to effectively reassemble the parts of the lattice if cluster defects are nearby. Interstitial atoms, i.e. atoms trapped between the lattice atoms, can cause atoms around them to move given enough energy. This causes a migration and there is a possibility for a vacancy to be filled [12].

These processes can both increase or decrease the defect concentration and hence the effective doping concentration. Decreasing the effective doping concentration is referred to as beneficial annealing, while increasing the effective doping is known as reverse annealing. It is empirically shown that the beneficial annealing of silicon has a shorter lifetime. Thus a device is expected to perform better after a short annealing [52], and then its performance starts degrading after receiving more annealing [54].

Annealing is highly dependent on temperature. The annealing rate decreases as temperature decreases since defects are more stable. To stop it, devices are kept cold. Temperatures of $< -10°C$ are low enough to reduce the negative effect of reverse annealing by few years [93]. If beneficial annealing is needed, it is commonly done by heating the device to $\sim 80°C$ for 60 minutes.

Chapter 3

Radiation hardness measured via the collection capacitance

Since the collection electrode capacitance depends on the effective doping, its value provides an excellent estimate of the damage to the silicon bulk by NIEL. Therefore in this chapter the capacitances of a new chip with no radiation dose received and a chip irradiated to above 10^{15} $n_{eq}cm^{-2}$ and 80 Mrad are measured and compared, in order to determine the radiation damage to the irradiated silicon. The techniques used also provide useful measurements that are used in the other chapters.

3.1 The Investigator chip

In this thesis, studies of CMOS prototypes for ATLAS produced by the TowerJazz (TJ) foundry are presented. The process is the TowerJazz 180 nm, which means that 180 nm is the minimum feature size. The prototypes are the Investigator chip, MALTA, mini-MALTA and TJ Monopix. The Investigator is a chip with minimal analog electronics (collection diode, reset mechanism and buffer), made for testing the properties of the silicon, the depletion region and radiation hardness. By adding digital readout electronics, it evolved into MALTA and TJ Monopix, which are full CMOS prototypes. TJ Monopix [22] has a column-drain readout, which is the same as LF Monopix, FE-I4 and FE-I3 [69, 21]. MALTA has a fully asynchronous readout, which has less power consumption and higher output rate. The mini-MALTA chip is a test chip with a novel in-pixel architecture discussed in chapter 5.

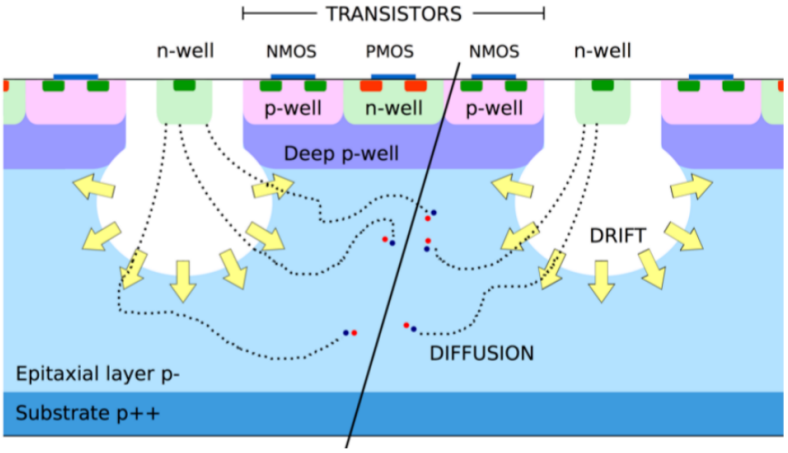
In this chapter, studies of the Investigator chip are presented. These are important, since this chip is the building block of the MALTA and TJ Monopix design. The collection electrode of the Investigator chip is easily accessible for testing since the chip has minimal readout electronics and as many as possible testing points. Its design came from the Investigator0 chip which was designed for the ALICE detector and has now evolved into the ALPIDE chip [78] used in the ALICE ITS upgrade, which will be installed in Run 3 of the LHC. The main problem for ATLAS is that the standard HRCMOS process for the Investigator0 is not radiation hard enough to withstand the lifetime radiation dose of the outermost pixel layer in ATLAS - 10^{15} $n_{eq}cm^{-2}$ and 80 Mrad. Therefore a modification was made to the process, which resulted in the Investigator1 chip. The difference between the chips is shown in Figure 3.1.

In the modified layout, the additional n^- layer makes the depletion region grow from the boundary with the p^- epitaxial layer when a voltage is applied to both the backside of the chip (bottom on the graph) and the deep p-wells. The result is a homogeneous lateral depletion region. Since the boundary between the n^- and the p^- layer is continuous, the conductive connection between the deep p-wells and the p^{++} backside substrate is broken. This gives the option of biasing the backside substrate to higher reverse bias voltages until a breakdown current from the p-well starts flowing. Since NIEL changes the effective doping and introduces traps, thus shrinking the depletion region, it makes the depletion region of the Investigator0 even smaller in the lateral direction. This problem is solved for the Investigator1, since if the depletion region shrinks, it would only be in the parallel to the depth dimension.

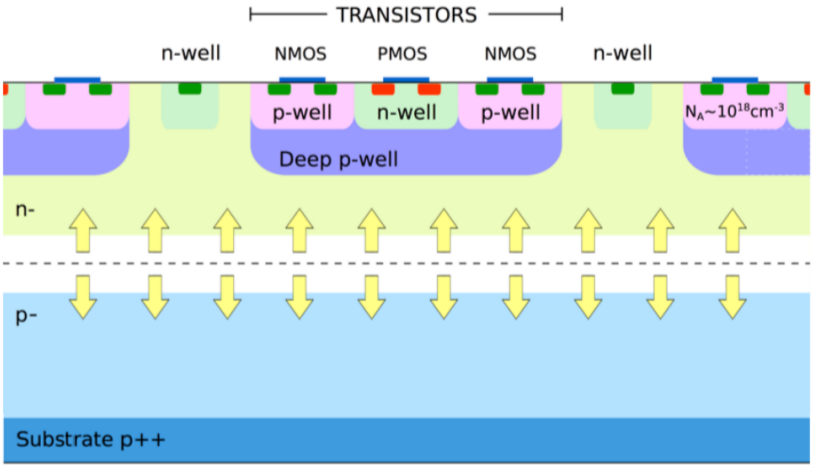
The Investigator2 chip includes further modifications of the Investigator1, which reduce the total leakage current, and enlarged transistors. Adding two different digital readout circuitries to it, produced two fully monolithic prototypes - MALTA and TJ Monopix. In this chapter, measurements of the radiation effects on the Investigator2 chip using two different methods are presented.

3.1.1 Chip design

Investigator1 and Investigator2 are very similar; therefore, their design is often referred to as the Investigator design. The chip has an area of 5×5.73 mm^2 and is sectioned in 268 mini-matrices. Each mini-matrix contains 10×10 pixels with the



(a) Standard HRCMOS process used for the Investigator0 chip

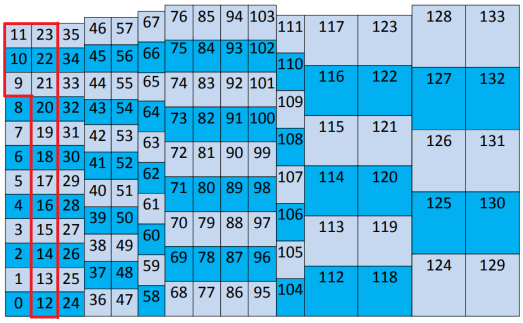


(b) Modified HRCMOS process used for the Investigator1 chip

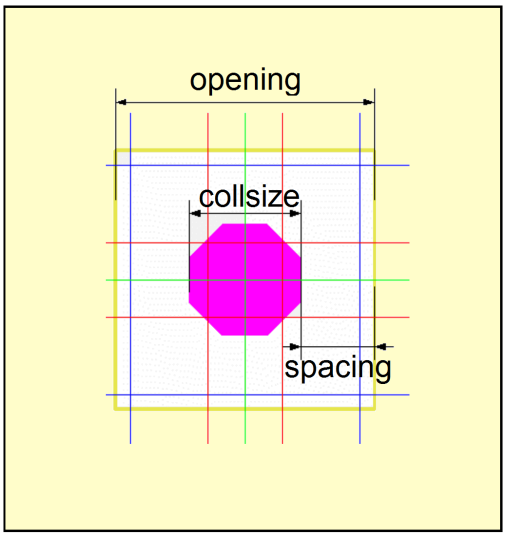
Figure 3.1: Sketch of the depletion region growth and charge collection for the standard HRCMOS process shown on Figure 3.1a and for the modified process shown on Figure 3.1b [71].

perimeter pixels being dummy pixels (pixels with on-chip disconnected readout). The chip has a dual matrix layout of 134 mini-matrices each. One part of the matrix layout allows for direct charge injection through an input capacitor and the other one does not have an input capacitor.

The mini-matrices differ by pixel pitch, collection electrode size, opening and spacing. The different layouts allow for measuring many chip properties (such as collection capacitance) as a function of several parameters. The mini-matrices are chosen by applying the rails voltage on 9 wire bondable pads that represent a 9 bit number, which is the index of the mini-matrix of choice. For the selected mini-matrix, there is an output for each of the inner 8×8 pixels that can be read out with an oscilloscope. After the signal is collected it goes through four source follower



(a) A layout of the 134 different mini-matrices available. The ones circled with red are the pixels with a diode reset.



(b) A top layout of the pixel. The octagon is the n^{++} collection electrode and the deep p-well cutout is the white square opening in the yellow deep p-well layer.

Figure 3.2: A layout of the 134 Investigator mini-matrices is shown in (a) and the collection electrode within the deep p-well cutout of a single pixel is shown in (b).

stages that buffer the output signal.

Source follower

The transistor is a semiconductor element made out of two back to back p-n junctions. MOS transistors have a gate (G), a drain (D) and a source (S) as shown in Figure 3.3. When enough voltage is applied to the gate of an nMOS transistor, the space between the drain and the source becomes conductive, while if the applied voltage is removed, no current can flow form the drain to the source. The pMOS has the same working principle, but is conductive when there is no voltage applied and non-conductive when the voltage on the gate is above threshold.

A source follower is a transistor where the drain is common to both the input and the output as shown in Figure 3.3. The important parameter of the transistor is its transconductance (g_m). It is defined as:

$$g_m = \frac{i_{out}}{v_{GS}} \tag{3.1}$$

where v_{GS} is the voltage between the gate and the source and i_{out} is the current going out of the transistor. These current and voltage signals are small changes relative

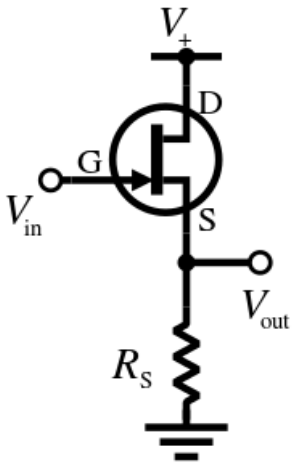


Figure 3.3: A schematic of a simple FET transistor used with as a source follower (common drain) [30].

to the constant DC values. The transconductance is measured in units of siemens (S). In the ideal case, where there is no current flow through the gate $i_{out} = i_D = i_S$. Then, the voltage gain (A_V) is the ratio of v_{out} to v_{in}. Since current can only reach ground through R_S, we can calculate v_{out} as:

$$v_{out} = i_D R_S = g_m R_S v_{GS} \tag{3.2}$$

This yields:

$$v_{in} = v_{out} + v_{GS} = (g_m R_S + 1) v_{GS} \tag{3.3}$$

Hence we can calculate the gain A_V. Picking values for the transistor and resistor, such that $g_m R_S \gg 1$ we get:

$$A_V = \frac{v_{out}}{v_{in}} = \frac{g_m R_S}{g_m R_S + 1} \approx 1 \tag{3.4}$$

The source follower provides gain of close, but slightly lower than one. It has a region of v_{in} voltages where the gain is constant and outside that region the gain is 0.

In the Investigator chip the signal on the collection electrode goes through four source followers. The first one has its gate connected directly to the collection

electrode. This allows for the voltage on the collection diode to be read out, but since no current flows through that gate, the charge remains in the collection electrode until it is flushed out some other way. Since the collection electrode is n-type, the electrons from the electron-hole pairs, created by particles traversing the chip, go towards it. The induced collected charge reduces its potential, since the charge collection is equivalent to charging the negative plate of the p-n junction capacitance. The collected charge would be seen as a voltage drop on the gate of the source followers and hence the output. If the charge is then flushed out at a point of choice, this would be classified as an integrating detector, since it integrates all the collected signal.

There are two reset mechanisms in the Investigator chip that flush out the charge available. The active reset using a pMOS transistor and the diode reset. Most of the pixels have the active reset and there are only 15 mini-matrices of the smallest pixel pitch ($20\times20\ \mu m^2$) that have the diode reset as shown in Figure 3.2(a). There are four source followers for both the diode and the active reset. The first two are slightly different to accommodate the different operating ranges of the two resets.

3.1.2 Active reset (pMOS)

The pixels with active reset need an additional reset signal (labeled RESET) to open a pMOS transistor and flush the charge from the collection electrode as shown in Figure 3.4. When the transistor is open, the operating point is set to the VRESET voltage, which for the active reset pixels should be $\sim 1V$, since that is the top limit of the linearity of the source followers. After turning the pMOS transistor off, the operation point voltage becomes floating and when charge is collected onto the electrode, the voltage drops to the lower limit of the source follower and the output signal flattens.

To validate the behaviour of the device and to make one of the measurements of the collection capacitance, a red LED was used. The visible light is detected by the Investigator chip, since there is a cutout in the metallization layers that would normally stop it. On Figure 3.5 the LED input and the output of the device for a single pixel are shown. After the pixel is reset, the device output is at $\sim 0.6\,V$. This corresponds to the operating point being at a voltage equal to VRESET, if it is assumed that there is no voltage drop over the pMOS reset transistor. Due to the leakage current and the photocurrent from leaks of ambient light, there is a slight

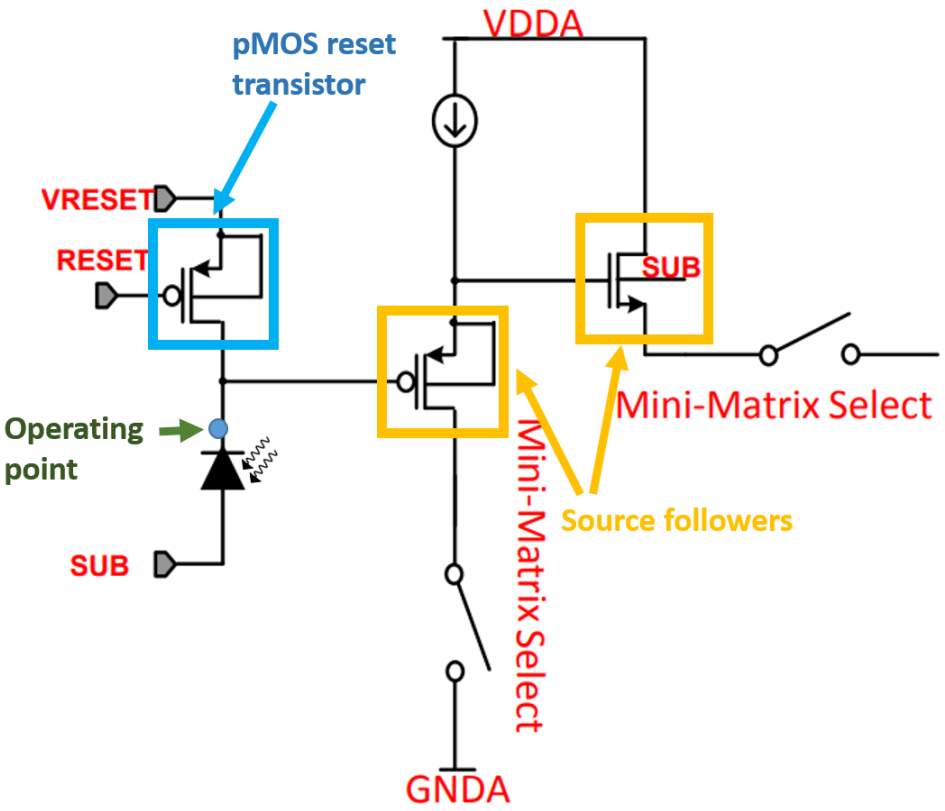


Figure 3.4: A schematic of the in-pixel circuitry for an active reset pixel. Two source followers are present for each pixels.

negative gradient even when LED is off. After the LED is turned on, the visible light is converted to electrons in the silicon, which charges the collection electrode negatively and reduces its voltage. The operating point voltage drops until it reaches the non-linear lower limit of the source followers. The pixel will not detect anything else until it is reset again.

3.1.3 Diode reset

The diode reset pixels have a similar circuit to the active reset, with the main change being in the reset mechanism (see Figure 3.6). The pMOS reset transistor is replaced with a diode. The source followers are at the same positions, but have a different range of linearity. There is current flowing through the diodes when the operating point is at a voltage below VRESET. When VRESET is reached, the current stops and the operating point remains floating. The generated signal in the photodiode lowers the operating point voltage. This creates a positive current flow through the

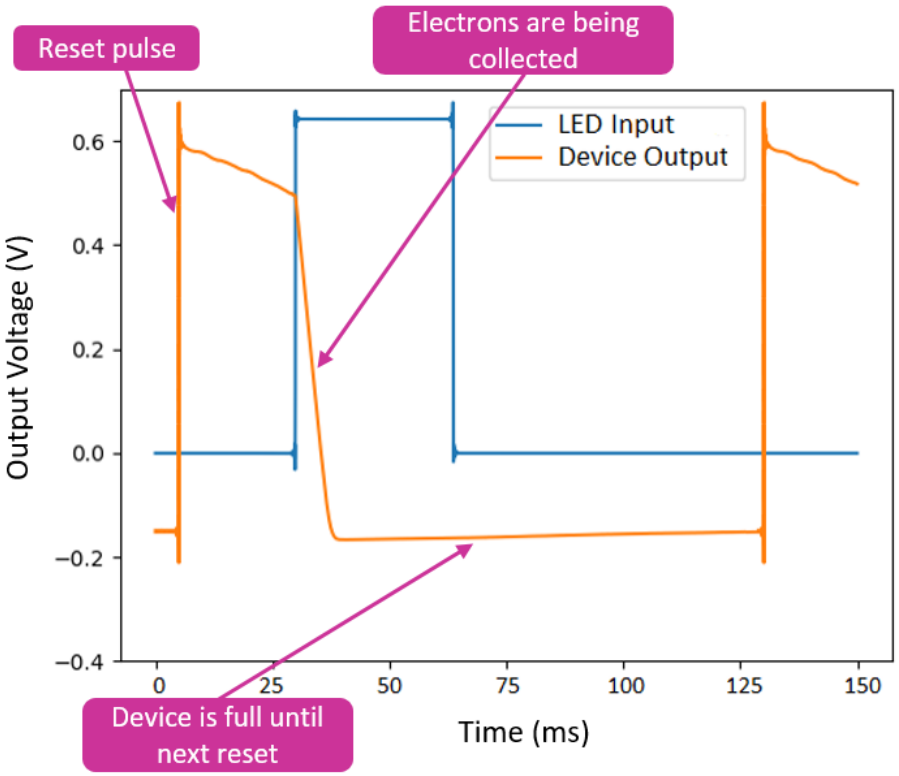


Figure 3.5: The standard output of a single pixel with active reset from the Investigator chip.

reset diode, which is equivalent to the negative charge in the collection electrode being flushed out to the VRESET terminal.

The output of the device is shown in Figure 3.7. There is the reset pulse that AC couples in from the active pixels, but is not necessary for the diode reset pixels as can be seen by the two consecutive LED pulses. The operating point voltage starts dropping when the red LED light signal is received. It reaches a steady state when the photocurrent balances out the charge, which is being flushed through the reset diodes. The voltage drop across the reset diodes is negligible for small currents, which is the case for the photocurrent generated in this device. Diode reset pixels are more robust to leakage current effects due to the leakage current being drained through the diodes. If the current is low enough so that the reset diodes remain with a negligible voltage drop, the effect is only shifting the baseline slightly. The MALTA and mini-MALTA chips (discussed in more detail in chapter 5) use diode reset pixels, thus this is the reset type of interest.

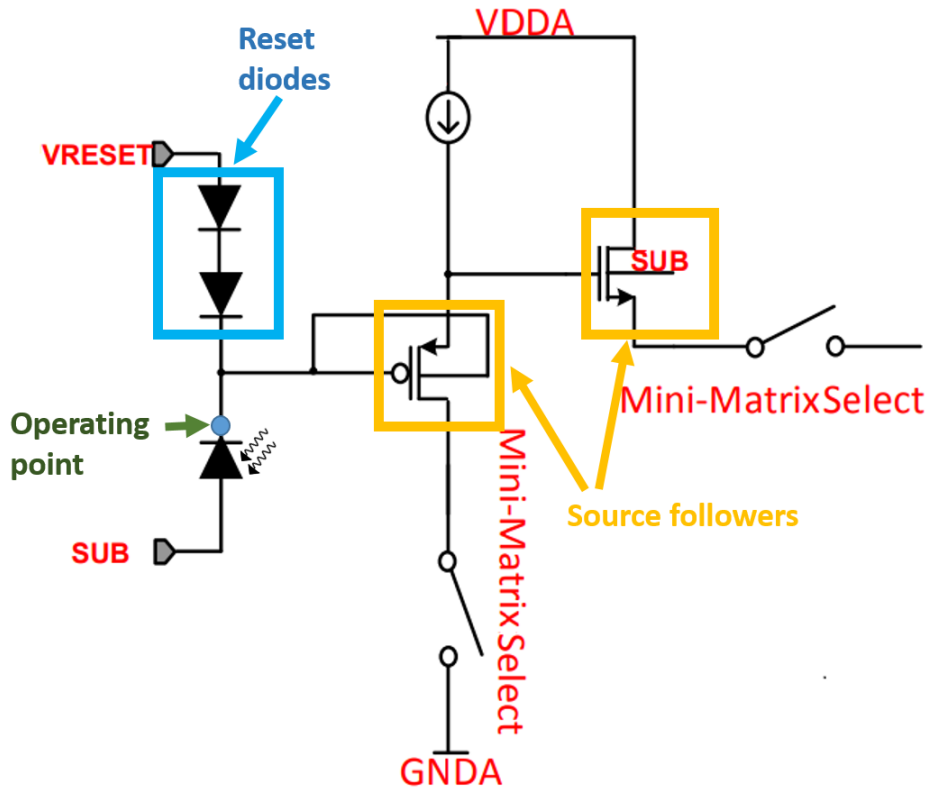


Figure 3.6: A schematic of the in-pixel circuitry for a diode reset pixel.

3.2 Measuring collection electrode capacitance

To measure the electrode capacitance two methods are used, which produce consistent results. The first one uses a monoenergetic X-ray source (^{55}Fe) with a conversion curve to measure the voltage drop directly. The second method uses an LED, following the approach developed Pain & Hancock [65] for integrating imaging devices.

3.2.1 Monoenergetic X-ray source

A commonly used X-ray source for lab measurements is the ^{55}Fe source. Its X-rays are produced by an electron being captured by the iron nucleus that then decays to ^{55}Mn. An Auger electron fills the empty K-shell space emitting an X-ray in the process. The half-life of this decay is $\sim$ 2.8 years. Its spectrum consists of three energy peaks called the $K_{\alpha 1}$, $K_{\alpha 2}$ and K_{β} with energies 5.898 keV, 5.888 keV and 6.49 keV, respectively [9]. The first two peaks are too close together to be distinguished by a silicon sensor, thus they are combined into one K_{α} peak with energy 5.89 keV, which is $\sim$ 8.5 times more prominent than the K_{β}. The X-ray has

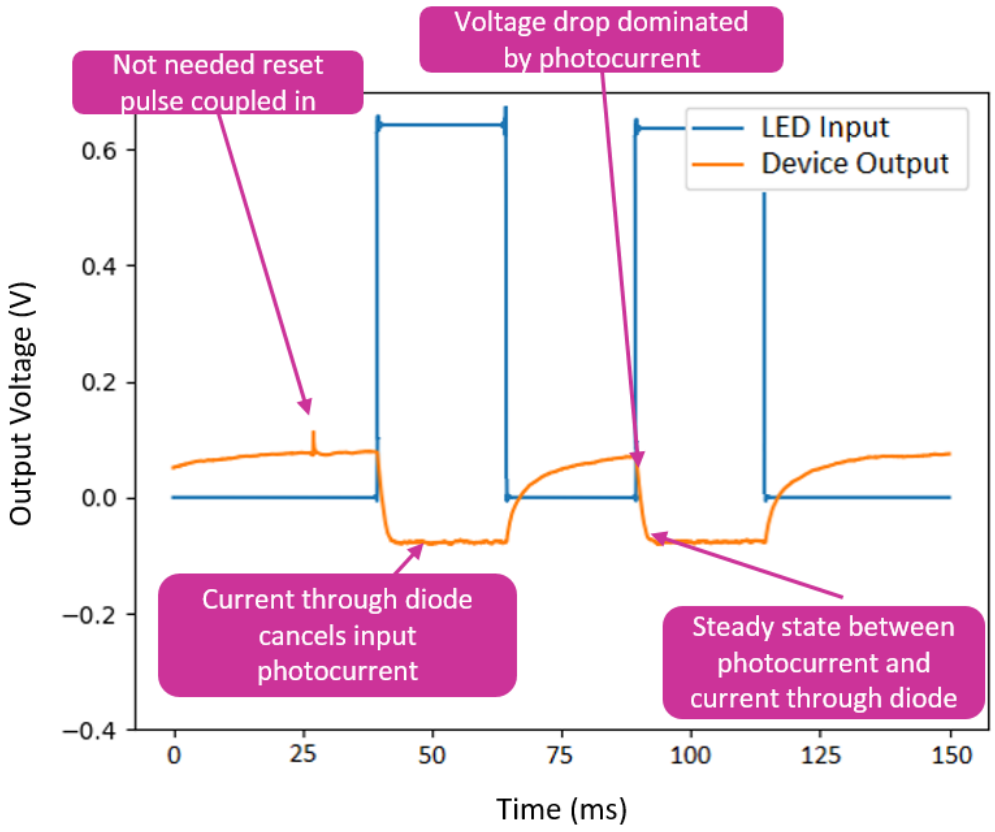


Figure 3.7: A plot of the standard output of a single pixel with diode reset from the Investigator chip with the different features described.

a certain probability to stop in the silicon and deposit its energy. The number of electrons created per X-ray is ~ 1610 for K_α and ~ 1780 for K_β, but those numbers are affected by random fluctuations in the number of electron-hole pair creation and charge collection. There is also a contribution due to the electronic noise component from the readout. The combination of these effects adds a Gaussian uncertainty to the energy of the detected X-rays.

The device under test was exposed to the X-ray source and raw waveforms were saved. The voltage drop on the output corresponds to a measure of electrons in the collection electrode and hence are proportional to the energy of the incoming photon. With the low noise, lower leakage current and lower concentration of traps in the non-irradiated case, the K_α and K_β can be distinguished as can be seen in Figure 3.8.

The charge released by the ^{55}Fe X-rays should always have the same value, but there is a probability that a part of it is collected by a neighbouring pixel. This is known as charge sharing and is the reason for the long tail of the ^{55}Fe source. As we

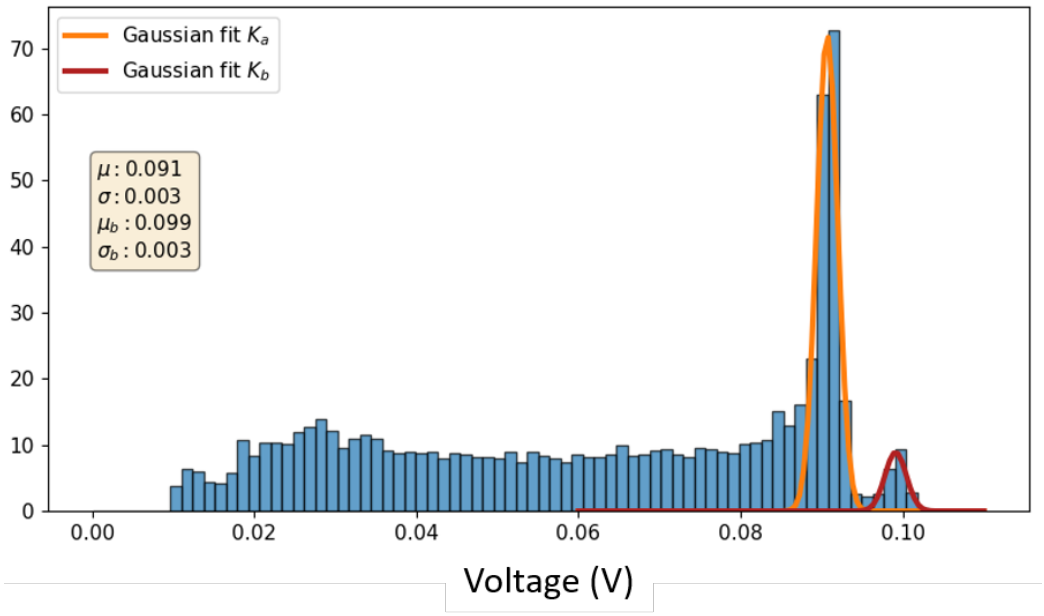


Figure 3.8: A normalized histogram of X-rays from an ^{55}Fe source detected by a non-irradiated Investigator2 chip from a pixel within mini-matrix 11 ($20 \times 20\,\mu m^2$ pixel size).

will show in chapter 5, this is not the case after irradiation. Depending on whether K_β can be resolved, the histograms give one or two points that correspond to a known number of electrons. These measurements are commonly used to produce a gain curve for the device, which is a plot correlating the amount of charge and device output voltage. The gain curve must start at the origin, since 0 electrons are equivalent to $0\,V$ signal. The ^{55}Fe spectrum gives at maximum two other points, thus if linearity is assumed, the gain curve can be created.

The pixels under investigation in Figure 3.9 are the ones in mini-matrices 9, 11 and 13. They all have a diode reset and an octagonal collection electrode with dimensions 3 μm $\times$ 3 μm. The only difference between them is the spacing parameter shown in Figure 3.2b. The spacings on mini-matrices 9, 11 and 13 are 1 μm, 3 μm and 5 μm respectively. Data was taken from two Investigator2 samples - a non-irradiated one and a proton irradiated one. The proton irradiation was performed at the MC40 cyclotron at Birmingham [15]. Protons deliver both TID and NIEL damage due to their charge and mass. The equivalent neutron fluence was determined precisely ($1.2 \pm 0.1 \times 10^{15}$ 1MeV $n_{eq}\,cm^{-2}$) using a technique that involves measuring the activation level of a Ni foil placed in front of the chip while it was being irradiated [45]. The 23 MeV protons at the cyclotron have a specific hardness factor, which is determined by measuring their NIEL damage relative to neutrons and a specific

stopping power [15]. Taking those into account, a TID equivalent dose of ~ 140 Mrad can be calculated for the irradiated Investigator2 chip. The results from the ^{55}Fe source are shown in Figure 3.9. Data is taken with 6V applied to both the back substrate and the deep p-wells. Irradiated modules were kept at $\sim -15\ ^{\circ}C$ to reduce leakage current and annealing effects. Each pixel is read on an oscilloscope, which is triggered on the signal itself. The threshold shown in each graph is placed well above the noise on the oscilloscope line, which is $\sim 5\,mV$.

The results shown in Figure 3.9 show the expected K_α and K_β peaks for the non-irradiated sample and the single widened K_α peak for the irradiated sample. Knowing the average charge released by the X-rays and assuming linearity of the gain curve, a value for the collection electrode capacitance can be estimated for each Gaussian fit.

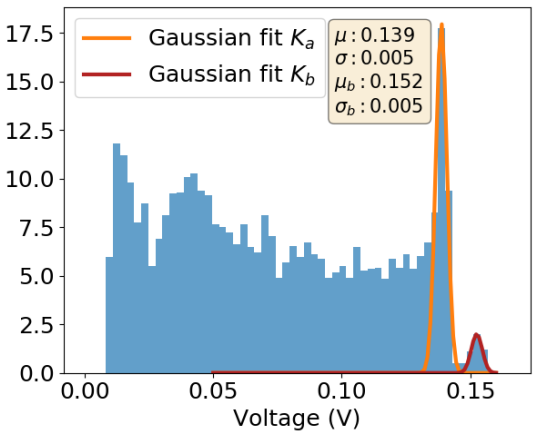
3.2.2 Pain-Hancock method

While the ^{55}Fe source gives at most two points on the gain curve, the Pain-Hancock method provides a continuous gain curve. The method is based on counting interacting photons of visible light from an LED. With a single voltage input pulse to the LED, photons are generated and reach the detector. Even if visible light photons can create roughly 1 electron-hole pair, many photons can be undetected. The number of interacting photons follows Poisson statistics [7]. This allows a mean-variance analysis, which is the basis of the Pain-Hancock method. Since the number of photons is proportional to the LED input pulse length, we define η to be:

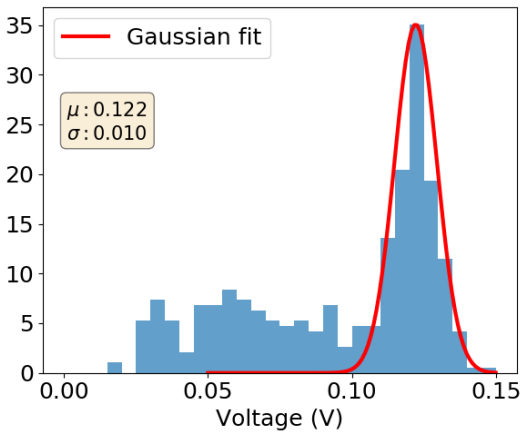
$$\eta = \frac{n}{P} \tag{3.5}$$

where n is the number of electron-hole pairs generated and P is the pulse length in units of time. Lets also define the function f, such that it gives the output voltage V for a certain number of collected electrons, $V = f(n)$. In the mean-variance analysis that function is assumed to be linear. Hence the conversion factor $f'(n) = \frac{dV}{dn} = C_g$ is used. The data taken consists of a large number of identical LED pulses recorded with their corresponding voltage drops. The pulse length can be changed continuously to generate a different amount of photons. The equations for a single LED pulse length using the mean-variance analysis are:

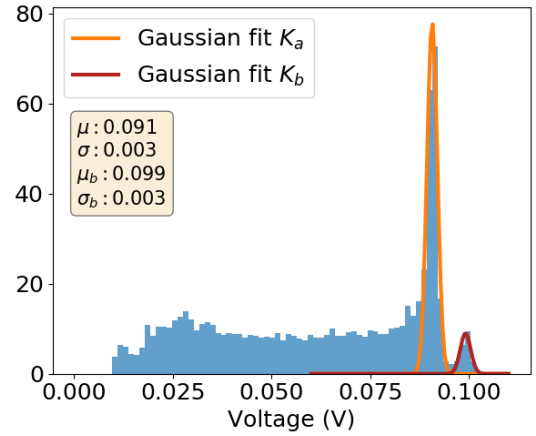
$$\langle V \rangle = C_g \langle n \rangle \tag{3.6}$$



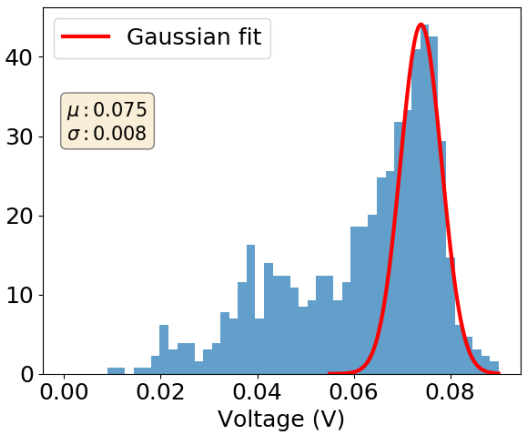
(a) Mini-matrix 9, with spacing 1 μm, non-irradiated



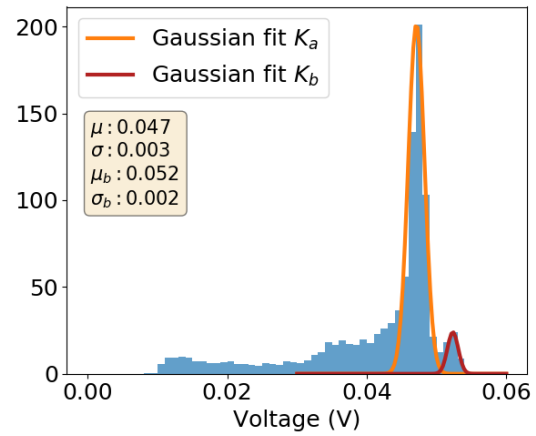
(b) Mini-matrix 9, with spacing 1 μm, irradiated



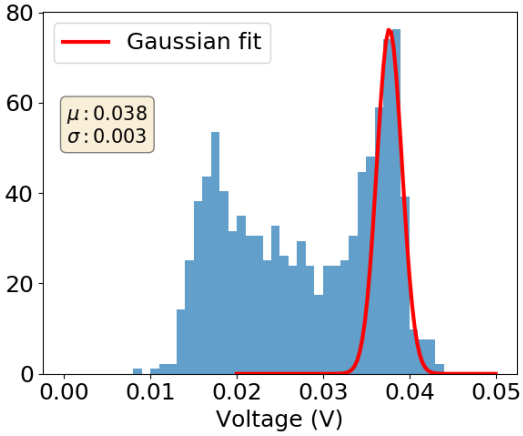
(c) Mini-matrix 11, with spacing 3 μm, non-irradiated



(d) Mini-matrix 11, with spacing 3 μm, irradiated



(e) Mini-matrix 13, with spacing 5 μm, non-irradiated



(f) Mini-matrix 13, with spacing 5 μm, irradiated

Figure 3.9: Histograms of ^{55}Fe source for different samples. Each row represents a different spacing (see Figure 3.2b). The results on the non-irradiated (irradiated to 1.2×10^{15} $n_{eq}\,cm^{-2}$ and 140 Mrad(Si)) Investigator2 chip are shown in the left (right) column. All pixel sizes are $20 \times 20\,\mu m^2$.

$$\sigma_V^2 = C_g^2\sigma_n^2 + \sigma_{readout}^2 \tag{3.7}$$

where $\langle V\rangle$ and $\langle n\rangle$ are the mean voltage amplitude and number of electrons created from all the pulses with a single pulse width, σ_V^2 and σ_n^2 are their variances and $\sigma_{readout}^2$ is the noise component from the readout electronics. From the Poisson process, it can be shown that $\sigma_n^2 = \langle n\rangle$. Measurements with different LED pulse lengths give different voltage amplitudes and variances, allowing the calculation of the conversion factor as:

$$C_g = \frac{d\sigma_v^2}{d\langle V\rangle} \tag{3.8}$$

The mean-variance method is equivalent to multiplying the voltage amplitude by a conversion factor, such that data from different LED pulse measurements has gradient 1 on a $\langle V\rangle$ vs σ_V^2 graph.

In a non-linear estimation method (NLE), which is the one described by Pain & Hancock [65], there is no assumption of linearity of the transfer function $f(n)$. Instead, Taylor expansion to second order around the mean value of electrons (labelled as $N = \langle n\rangle$) from a pulse is used:

$$\langle V\rangle = \langle f(n)\rangle \approx f(N)+f'(N)(N-n)+f''(N)\frac{(N-n)^2}{2} = f(N)+0+f''(N)\frac{\sigma_n^2}{2} \tag{3.9}$$

Keeping terms up to second order we get:

$$d\langle V\rangle = f'(N)dN = \eta f'(N)dP \tag{3.10}$$

The fact that $f'(N)$ is not a constant is the main difference with the mean-variance method. Using Equation 3.10, the equation for variances becomes:

$$\sigma_V^2 = \sigma_{readout}^2 + f'(N)^2(\sigma_n^2 + \sigma_{electrons}^2) \tag{3.11}$$

where $\sigma_{electrons}$ is a factor contributing for the fluctuations in the number of electrons collected and the other ones are the same as in Equation 3.7. Using $\sigma_n^2 = N$, Equation 3.10 and Equation 3.5, we get the following:

$$\sigma_V^2(P) = \sigma_{readout}^2 + P\left[\frac{\langle V(P)\rangle'}{\eta}\right]^2 + \sigma_{electrons}^2\left[\frac{\langle V(P)\rangle'}{\eta}\right]^2 \tag{3.12}$$

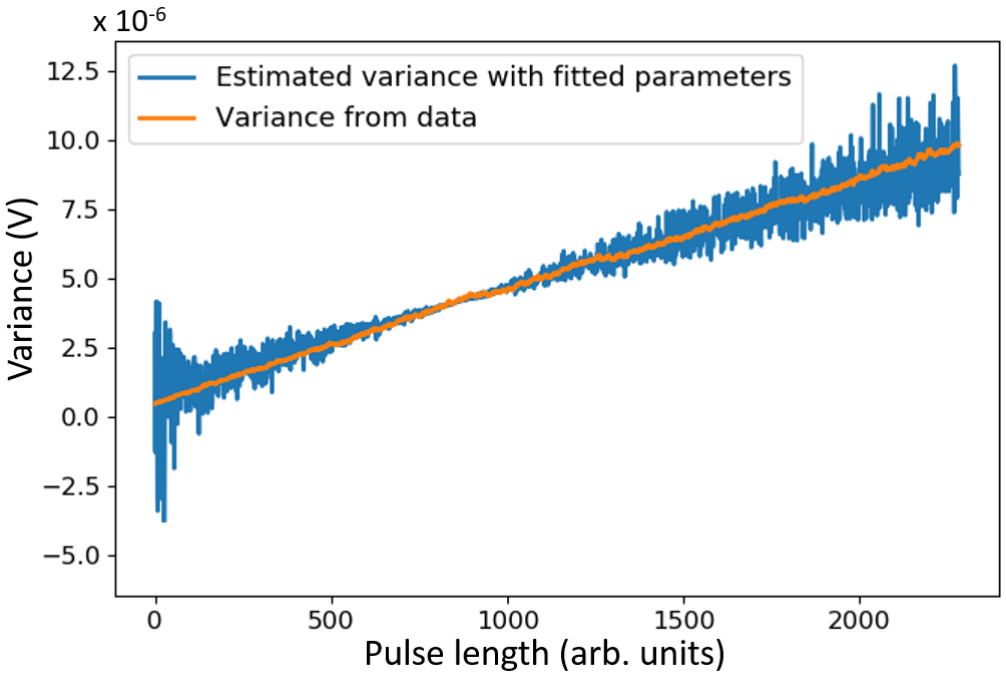
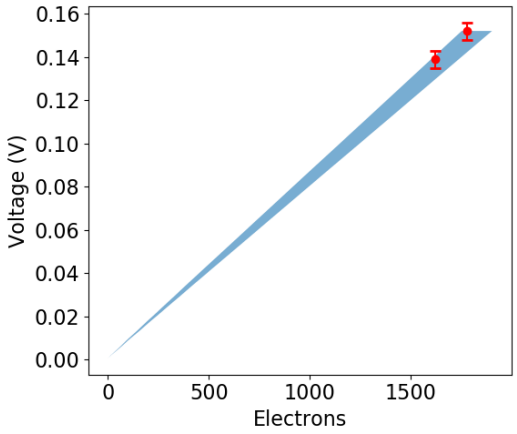


Figure 3.10: An example of the variance of the voltage amplitudes detected plotted for each pulse length (LHS of Equation 3.12) and the calculated variance using fitted parameters along with $\langle V(P)\rangle'$ (RHS of Equation 3.12). Data taken from a non-irradiated Investigator2 chip from a pixel in mini-matrix 11 ($20 \times 20\,\mu m^2$ pixel size).

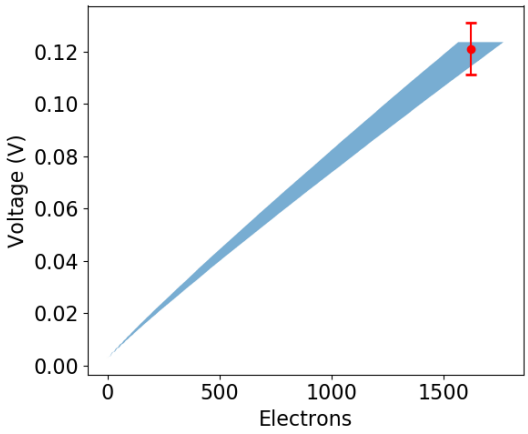
The pulse that is fed to the LED is generated with a pulse generator. Afterwards the output of the pixel is read out with an NI-9215 Analog Input module. This is because the variance requires high precision but the voltage drop is also large, thus a 16-bit ADC is needed. The values of P, $\sigma_V^2(P)$ and $\langle V(P)\rangle'$ are known, having taken multiple data points with a recorded amplitude V for a number of different pulse lengths P. Thus the $\sigma_{electrons}^2$, $\sigma_{readout}^2$ and η are parameters to fit such that the right hand side is equal to the left hand side for every P as shown in Figure 3.10.

To create a gain curve, the mean of the voltages for each pulse length $\langle V(P)\rangle$ are used to extract the parameter η, which converts $\langle V(P)\rangle$ to $\langle V(N)\rangle$. Data with an LED is taken for the same pixels that are shown in Figure 3.9. The conditions were kept the same as much as possible. Since they have a diode reset, having a long pulse length would produce enough current to make the voltage drop on the reset diode large enough to alter the operating point. When this happens the fitting

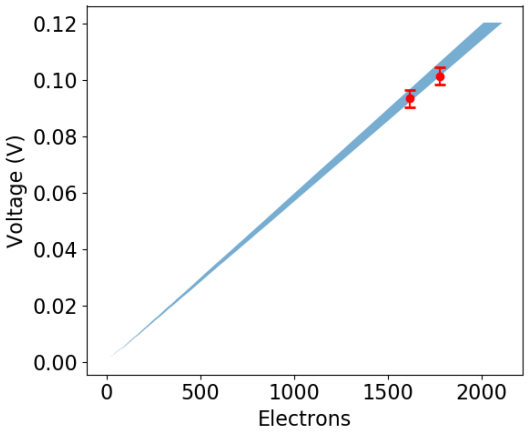
in the Pain-Hancock method becomes worse. Thus the pulse lengths are taken until a pulse length P such as the fits are good and there is no voltage contribution from the reset diode. This point varies between pixels since the different pixels would experience different leakage current due to internal factors such as the in-pixel layout and external factors such as light leaks, temperature, position of the LED, etc. To estimate the error on the gain curve, multiple samples were taken and a separate gain curve was calculated for each. This gives a distribution of η values and the standard deviation of that distribution is taken as error. Results are shown in Figure 3.11. The gain curves are used in chapter 4 to convert the signal to electrons.



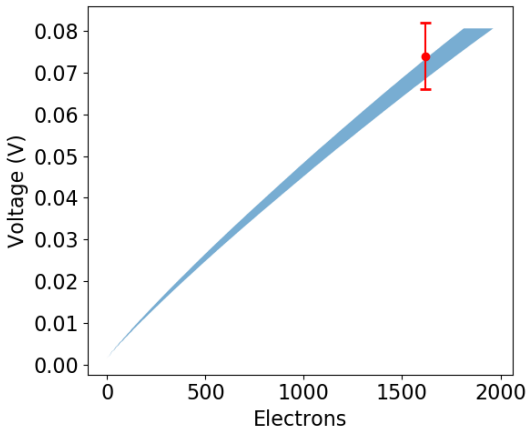
(a) Mini-matrix 9, with spacing 1 μm, non-irradiated



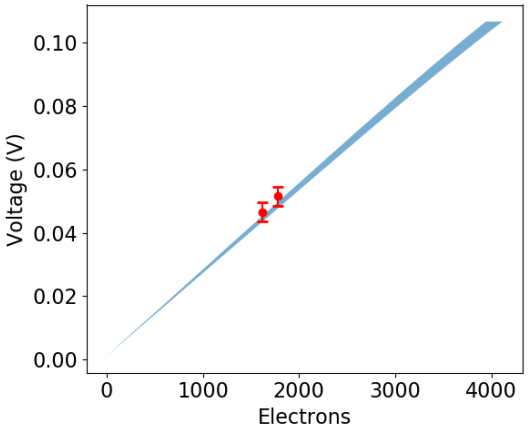
(b) Mini-matrix 9, with spacing 1 μm, irradiated



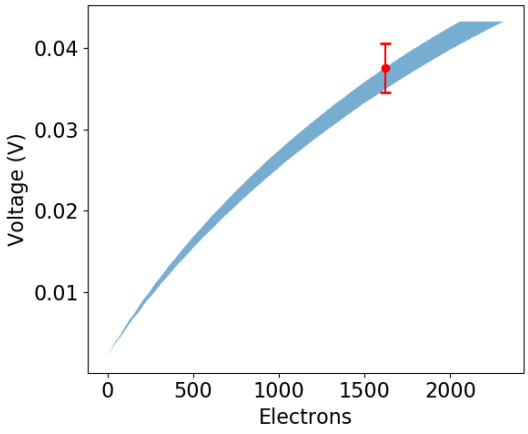
(c) Mini-matrix 11, with spacing 3 μm, non-irradiated



(d) Mini-matrix 11, with spacing 3 μm, irradiated



(e) Mini-matrix 13, with spacing 5 μm, non-irradiated



(f) Mini-matrix 13, with spacing 5 μm, irradiated

Figure 3.11: Gain curves of the same Investigator2 chip pixels shown in Figure 3.9. The red dots are the ^{55}Fe peaks with their corresponding value in electrons.

3.2.3 Source follower contributions

As the gain curve is a relation between charge and voltage, the gradient of this curve is the capacitance. However the voltage recorded is on the device output, after the four source following stages. Thus in order to measure the capacitance of the electrode, a relation between the operating point voltage and the collected charge is needed. To do that the source followers are probed by slowly changing VRESET while the device is in the dark. When there are no electron-hole pairs being produced, a positive change in voltage in VRESET is going to the same positive change in the operating point voltage. The curve in Figure 3.12 is showing the correlation between VRESET and the output voltage.

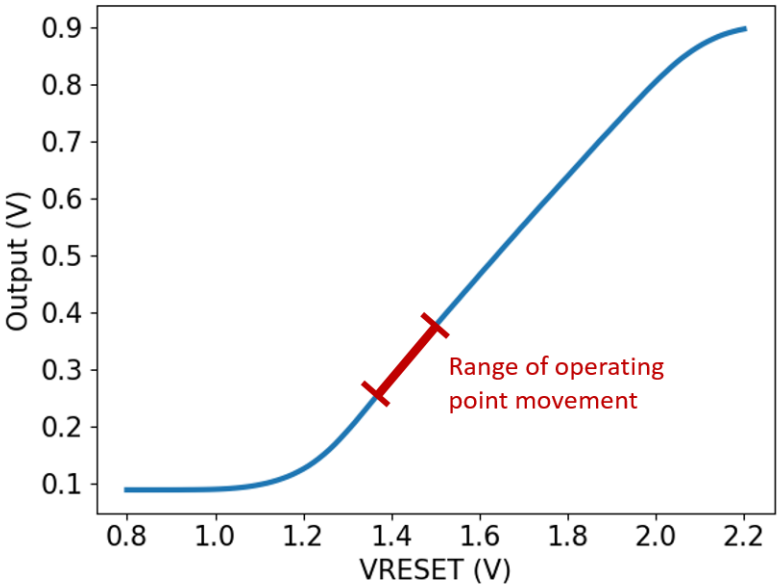


Figure 3.12: A curve of the recorded output voltage of mini-matrix 11 as VRESET changes. The normal range of movement of the operating point while the device is taking data is highlighted.

All the data is taken with VRESET of 1.5V, which is in the linear region of the source followers. The amplitudes that are recorded are $\leq 150\,mV$, thus the range of the operating point is linear. The value of capacitance that is obtained from the gain curve is multiplied by the gradient of curve in Figure 3.12 at the used VRESET voltage. The output voltage versus VRESET correlation is very similar between pixels, but to achieve precision the correlation is measured for each pixel separately.

The pixel capacitance is calculated from the initial gradient in the gain curve. To demonstrate the effect of the source follower, the capacitance with and without

the adjustment from the source follower is calculated at different VRESET for mini-matrix 11. The results are shown in Figure 3.13. Data is taken with $-6\,V$ applied to both the back substrate and the deep p-wells. The change of the operating point is a few $100\,mV$ in a region where the effective external depletion voltage is $> 6\,V$. Therefore it is expected that the collection electrode capacitance does not change significantly within this VRESET interval. The adjustment of the source follower flattens the curve in its non-linear region and reduces the capacitance slightly in its linear part.

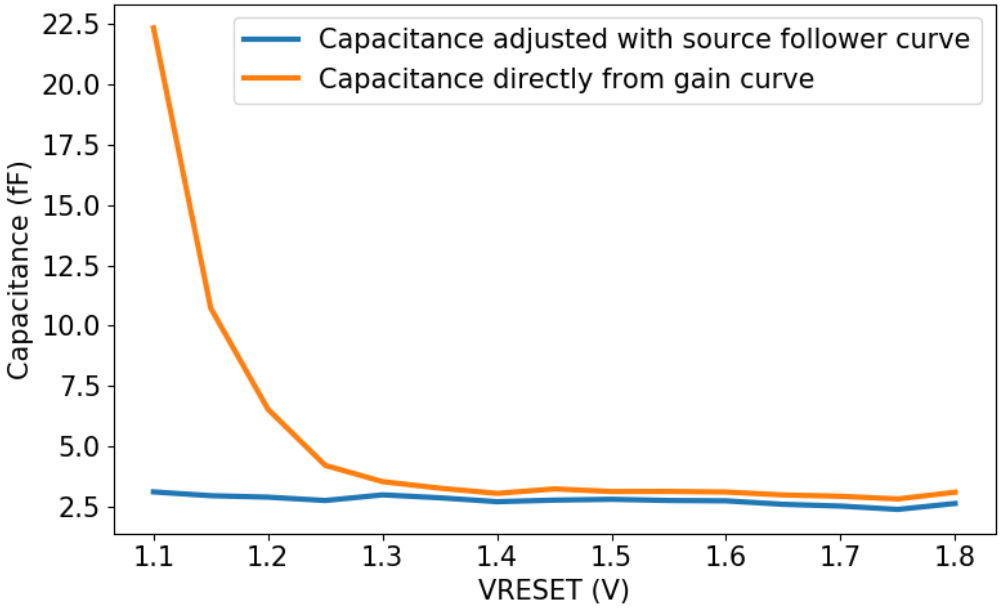


Figure 3.13: The orange curve shows the capacitance value obtained from the initial gradient of the gain curve. The blue one shows the same quantity multiplied by the gradient of Figure 3.12 at the corresponding VRESET.

3.3 Comparison before and after irradiation

Using the procedures described above, capacitances were calculated for the non-irradiated and irradiated Investigator2 chip. The devices are different and this could create difference between the result of the measurements. To account for that, the calculations were done on multiple pixels from each mini-matrix to estimate an average and an error. The results are shown in Figure 3.14. They agree with similar measurements on a non-irradiated Investigator chip, using a parameter that is close to the collection capacitance as shown in Figure 9.6 in [61].

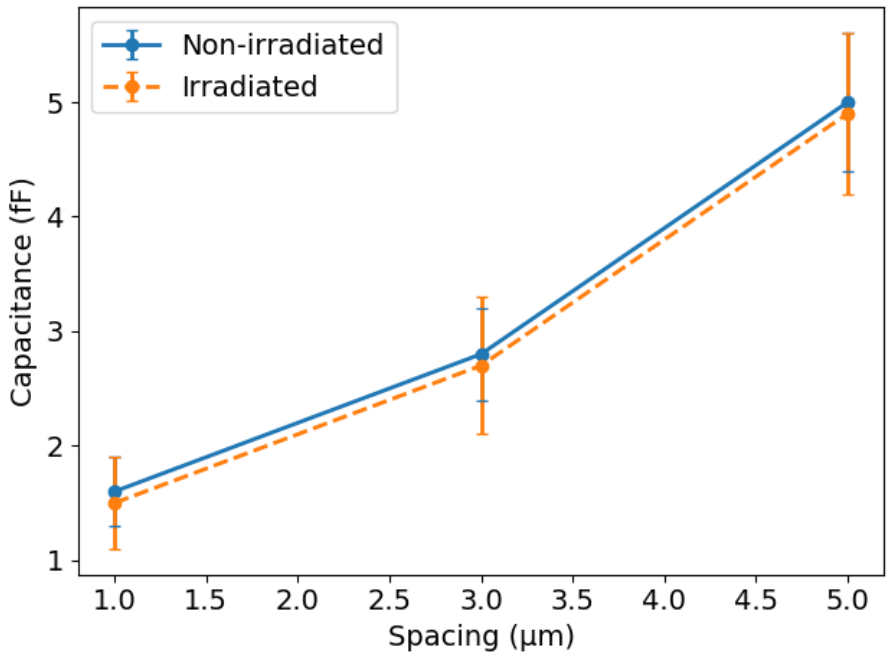
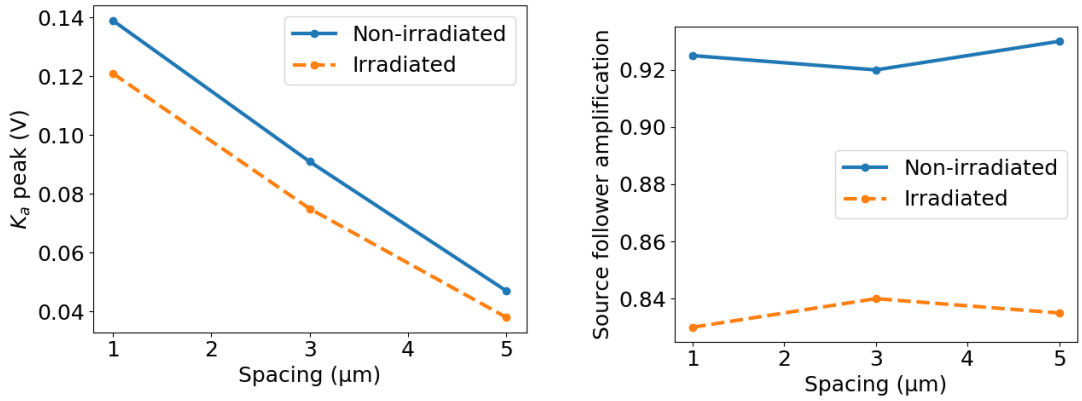


Figure 3.14: Collection electrode capacitances measured for a non-irradiated sample and a sample irradiated to 1.2×10^{15} $n_{eq}\,cm^{-2}$ and 140 Mrad for different spacings.

The capacitance does not change after irradiation within error. This means that the effective radiation damage to the silicon bulk is not enough to cause a change in capacitance. Since spacing is the distance to the deep p-well, a natural assumption would be that the dominating effect is the capacitance between p-well and the collection electrode. However since $C \sim 1/d$, that would mean that the capacitance should decrease with larger spacing. This is not observed due to the development of the depletion region. Since there is an additional n^- layer as shown in Figure 3.1b, there is a p-n junction between that n^- layer and the deep p-well. Therefore, part of the depletion region grows from this junction as well. If the depletion depth does not reach the n^{++} implant, the effective collection electrode becomes the non-depleted volume around the implant including the implant. This means that at larger spacing, there is more non-depleted volume creating a bigger surface area for the effective collection electrode. Since $C \sim A$, the capacitance would increase with larger spacing [61].

The capacitances are measured to be very similar, which shows that the chip could withstand a fluence of 1.2×10^{15} 1MeV $n_{eq}\,cm^{-2}$. Figure 3.9 shows that the ^{55}Fe peak are consistently lower for the irradiated sample. This can be explained by the effect of the source follower. A comparison between the X-ray peaks and the adjustment factor obtained from the source follower curve is shown in Figure 3.15.



(a) ^{55}Fe K_α peaks (b) Source follower gradients

Figure 3.15: A graph showing the ^{55}Fe K_α peaks (a) and the source follower gradients (b) for different spacings. The irradiated X-ray peaks are lower, which is consistent with the source follower gradient adjustments.

From the figure it can be seen that the source follower coefficient of the irradiated sample is lower by roughly $\sim 10\,\%$. The irradiated K_α peaks are reduced by roughly the same amount. This suggests that the capacitances are the same and the lower output on the irradiated sample is due to the different source follower gradient. The TID damage would affect mainly the transistor in the source follower, as charge can accumulate at its gate and alter its g_m. However since there are two different devices from two different batches, random fluctuations in the processing are also possible. Therefore it is not certain whether the change in the source follower output is solely due to extensive radiation damage. The main clearly visible change during these measurements for the irradiated device is the change in leakage current, which then introduces noise on the output. It is highly dependent on high temperature and reverse-annealing effects at high temperature, which is the reason why the operating temperature if ATLAS being well below zero.

Active reset

Due to the fully-integrating detector design, the irradiated active reset pixels are more susceptible to leakage current. The charge generated by the leakage current is accumulated on the collection electrode, forcing the operating point to an equilibrium voltage, which is outside the source follower linear regime. The device would then need another reset pulse to change the operating point voltage. Depending on the amount of leakage current, the device is going to be functional for some time

before needing another reset. If the leakage current is too high, it could contribute significantly more than the signal, which would make the signal not detectable. The output of mini-matrix 2 of an irradiated Investigator2 sample is shown in Figure 3.16.

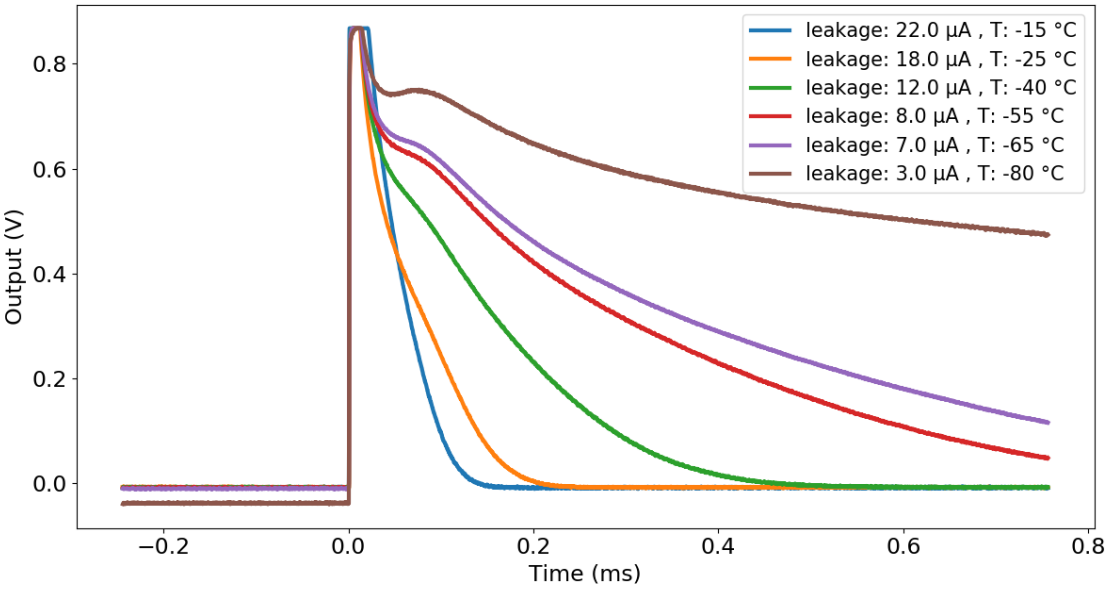


Figure 3.16: The output of a pixel in the dark at different temperatures. The measurements are done on the irradiated Investigator2 sample on mini-matrix 2, which is the equivalent of mini-matrix 11 with an active reset. The pixel is reset at 0 ms and the reset pulse is 10 μs long. The p-wells and the back substrate are biased to $-6\,V$.

Figure 3.16 shows that the high leakage current is filling the collection electrode within $< 1\,ms$ for temperatures $\geq -60\,°C$. Maintaining lower temperatures than that for large amounts of time is difficult (especially using the setup described in chapter 4) and the leakage still has a significant contribution to distort the charge collected from a real particle. Another option is to reduce the amount of biasing voltage, which reduces the leakage current. However, this reduction would change the electric field distribution within the pixel and make the results less comparable. Since the fully monolithic prototypes - MALTA and mini-MALTA (discussed in chapter 5) use only diode reset pixels, many measurements presented in this thesis focus on the diode reset.

3.4 Summary

In this chapter the analog circuit of the Investigator sample is explained. Detection of visible light from an LED is then used in a technique developed by Pain & Hancock [65] to produce a gain curve of the device. This allows conversion of the output voltage of the device into electron-hole pairs, which is also used in chapter 4. The gain curves are validated using a monoenergetic ^{55}Fe source. The results are then used to estimate the capacitance of the collection electrode of the non-irradiated sample and the sample irradiated to 1.2×10^{15} $n_{eq}\,cm^{-2}$ and 140 Mrad(Si). This is a direct measurement of the radiation damage to the silicon bulk. The results show no significant damage to the silicon substrate. Only differences in the source follower transistors are observed, but they are not large enough to be considered as evidence of TID damage.

Chapter 4

Depletion region comparison before and after irradiation

In this chapter measurements of the depletion region of the Investigator2 chips are presented. Radiation damage affects the effective doping and charge collection, which change the depletion region. Its depth and shape before and after irradiation would corroborate results in chapter 3. Knowledge of the depletion region also provides important information about signal generation in the device and the possibility of increasing the magnitude of the signal by changing the bias voltage.

4.1 Laser E-TCT

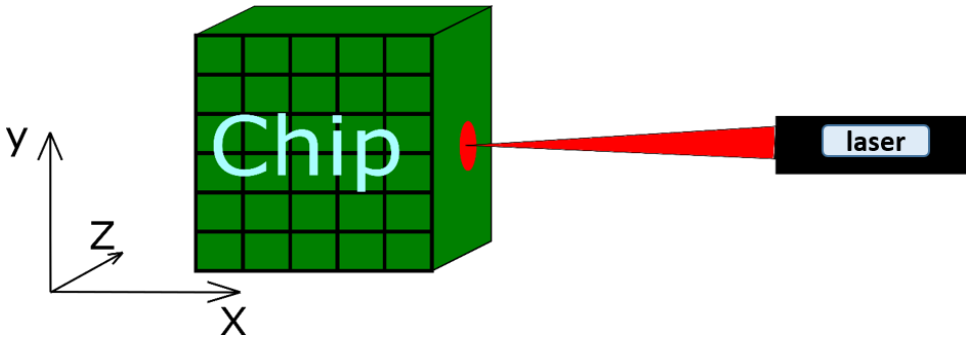


Figure 4.1: Sketch of the E-TCT setup. The axis are defined w.r.t. the detector under test. The Z axis is along the depth of the detector, while the surface is in the XY plane.

The Edge Transient-Current Technique (E-TCT) [18] is way of measuring the

depletion depth of a silicon sensor, typically by using an infrared pulsed laser. The specific system used in the OPMD laboratory involves a laser that can operate with wavelengths of 1064 nm and 660 nm [66]. The setup consists of a focused laser beam shining on the device under test (DUT), which is mounted on its edge on motion stages as shown in Figure 4.1. The stepping motors on the motion stages have a step size of 1.25 μm. To see sub-pixel components from the output of one pixel, we look at the analog output of a single pixel. By focusing the laser beam on the pixel in the X dimension and then scanning in the YZ plane while recording the output amplitude for each step, an image of the depletion region can be constructed.

4.1.1 Laser wavelength and power

It is easier with E-TCT to study pixels that are located at the edge of the chip, since they could be exposed directly to the laser beam. However, every Investigator chip has pixles with different layout configuration at different locations. The pixels with a diode reset that were studied in chapter 3 are on the edge of the chip. However, there are guard rings located between them and the chip boundary.

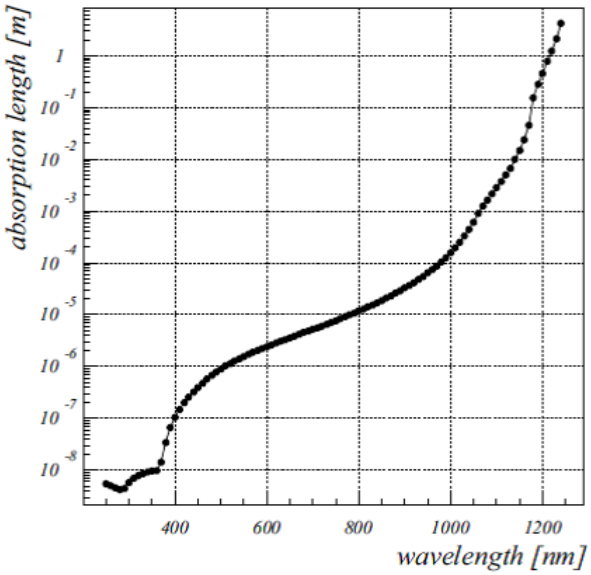


Figure 4.2: The absorption length of silicon for wavelengths in the visible and infrared region[11].

Figure 4.2 shows that silicon is more transparent for infrared than visible light. Therefore the 1064 nm laser is conventionally chosen for E-TCT since more pixels are reachable by the laser light and there is less attenuation of the light when changing pixels.

Due to the small collection capacitance, the threshold for detection is low ($\sim 150\,e^-$ is used in MALTA [24]). The laser system allows for intensity adjustment internally through a digital-to-analog converter and externally through a a flexible aperture. The E-TCT technique works best when the laser pulse signal is of the same order of magnitude as the signal expected during the normal operation of the device. If this condition is achieved, the distortion of the image can be minimized and the device can be operated in optimal gain range that was studied in chapter 3. This allows for direct comparison with a Technology Computer-Aided Design (TCAD) simulation, which is discussed in section 4.3. The length of the pulse is dependent on the setting of the digital-to-analog converter, but would vary between $\sim$ 1 ns to $\sim$ 5 ns. The pixel is readout with an oscilloscope, thus the integration time is effectively set by the timescale of the oscilloscope. In this experiment a window of 500 ns was used.

4.1.2 Focusing

Precision focusing of the laser is essential for E-TCT measurements. Thus before starting a scan in the YZ plane, the laser must be focused in the X dimension by using the front surface of the pixel under test(Figure 4.3). The depletion region on the boundary of the pixel represents a step function $H(Z)$. Thus the pixel output that is observed on that edge, is a convolution of the laser distribution with $H(Z)$. By assuming that the beam profile of the laser beam in the YZ plane of the pixel has a Gaussian distribution, we find:

$$H(Z) * Gaussian(Z|Z_0, \sigma) = \frac{2}{\sqrt{\pi}} \int_0^Z exp(\frac{(x - Z_0)^2}{2\sigma^2})dx = Erf(\frac{Z - Z_0}{\sqrt{2}\sigma}) \quad (4.1)$$

Since the pixel is symmetric in the Y dimension, it is sufficient to find the maximum of the output w.r.t to the Y position, to know that the laser light is in the centre of the pixel along that dimension. Then a 1 dimensional scan along the Z dimension is done. The result of the scan is an error function with a scale and an offset factor, as shown in Equation 4.2. Thus the function fitted to the output of the scan as shown in Figure 4.4 is:

$$f(Z) = A \times Erf(\frac{Z - Z_0}{\sqrt{2}\sigma}) + B \quad (4.2)$$

The Z_0 parameter of this fit gives the position of the midpoint of the slope and the σ parameter is defined as the position resolution of the scan. To find the focus

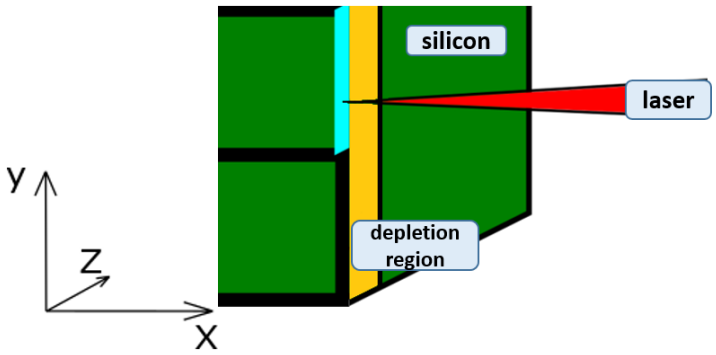


Figure 4.3: A closeup figure of the chip and the depletion regions. The light blue is the boundary onto which the laser is being focused. The yellow area represents the depleted layer across the whole chip.

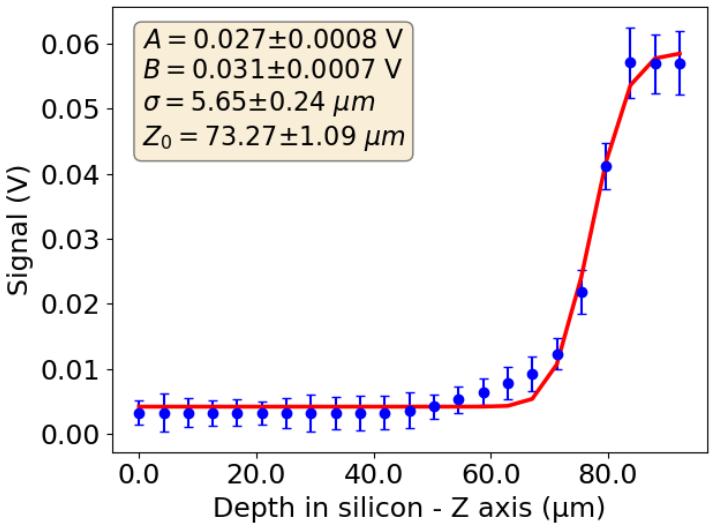


Figure 4.4: A scan along the Z direction at the boundary of a pixel. There are 10 recorded amplitudes per laser position. Their mean is given as the signal and the square root of their variance as the error. The fitted function (red) is shown in Eq.(4.2).

of the laser beam, the chip is moved in the X direction relative to the laser and the σ parameter is extracted for each step in X. The resulting data is fitted with a parabola as shown in Figure 4.5. Then the position of the minimum is extracted for the current pixel and is used as the focal plane, in which the depletion depth scan is done. The value of the minimum depends only on the optics aperture and is similar between the different pixels. Thus the resolution of the laser is measured to be 4.56 ± 0.65 μm as half the Gaussian spot size. It is possible that this technique focuses the laser on something other than the pixel, such as the boundary of the whole chip. To confirm that the pixel under test is in focus, an additional minimization is done. Scans at

different X positions of the whole sensitive region are done and the pixel width in the Y dimension is measured using a full width at half maximum. This results in a similar parabola as in Figure 4.5 and the identical position of the minima of both parabolas is used as confirmation of the correct focal plane.

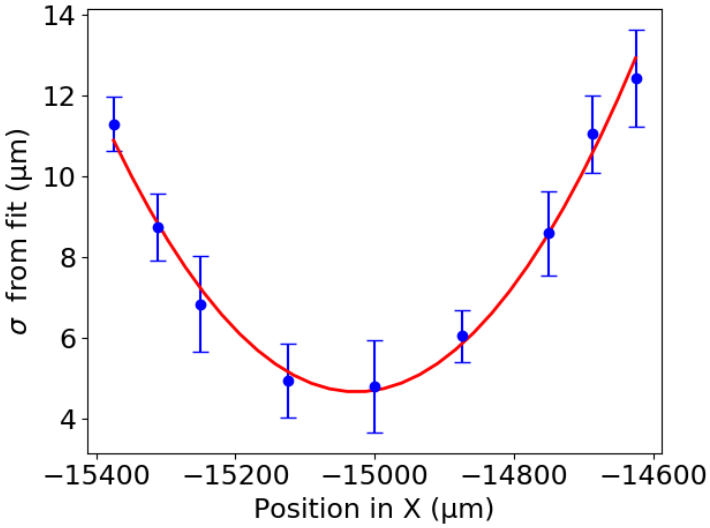


Figure 4.5: Plot of the resolution for each X position of the chip with a parabolic fit to extract the position of the minimum and its value.

4.1.3 Cooling apparatus

Cooling with a vortex cooler

One of the most important requirements for the operation of irradiated samples, is that they need to be kept cold at all times as discussed in Chapter 2. For cold operation, the air needs to be dry enough to prevent frost appearing on the chip. While not in operation, the devices are stored in a freezer. There are different methods to keep them cold while operating, depending experimental configuration. For example in an E-TCT setup or exposure to a radioactive source, cooling with a Peltier chip [17] or a liquid chiller is convenient. However in a test beam, it is important to minimize the material since beam particles should traverse all planes of the tracking telescope. Therefore methods like dry ice or liquid nitrogen boil-off in a thermally insulating box (such as polystyrene) are used in that setup. These methods are generally inconvenient due to needing refills and lack of availability of liquid nitrogen at some test-beam facilities.

An attractive solution is to use a commercially available vortex cooler along

with a portable compressor equipped with an air dryer for facilities where dry air is unavailable [56]. It has been demonstrated that the vortex cooler provides a portable stable cold and dry environment for a low price ($\sim 400£$) and can be used in most small scale experiments. Its basic working principle is illustrated in Figure 4.6. Since the output of the vortex cooler is a cold dry stream of air, no thermal contact to the device is needed. A pipe located as close as possible to the device is sufficient to provide the necessary cooling.

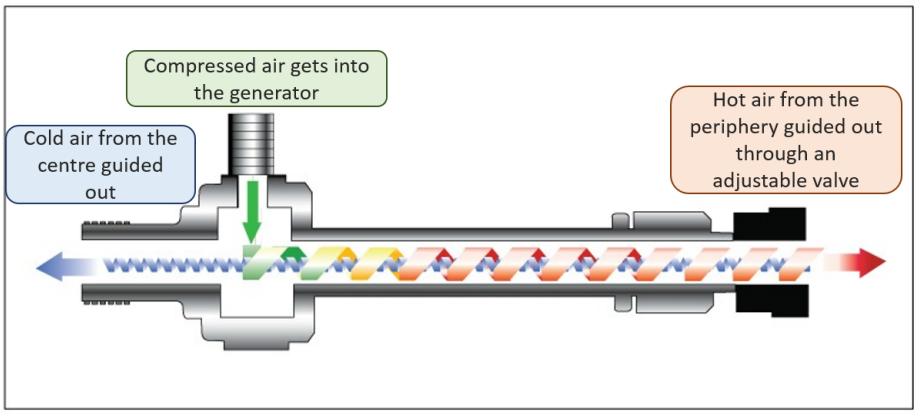


Figure 4.6: Diagram of the basic working principle of the vortex cooler. The high pressure room temperature air enters and creates a swirl. The hot particles on the periphery are guided out on one side whereas the cold ones from the center exit from the other side. The figure is adapted from [56].

Vortex cooling in the E-TCT setup

The printed circuit boards (PCBs) for the Investigator 1 and Investigator 2 chips are designed to be compatible with E-TCT operation and have an extended shape as seen in Figure 4.8b. However, this shape makes it hard to cut a hole in the PCB behind the chip for cooling, which is the way it is done for CCPD_LF, LFCPIX and other chips [92]. There are also no copper thermal vias in the PCB to supply a thermal contact to the back of the chip. Thus a Peltier element would not work well, due to the thermally insulating layer of PCB material between the accessible back of the PCB and the chip.

To overcome this problem, the Vortex cooling system was used to cool the air around the chip. The setup is shown in 4.8a. The motion stages of the E-TCT set-up are enclosed in a polystyrene box with enough room to move freely. The only holes in the box are for the cables, the pipe with the cold air and the laser. Air

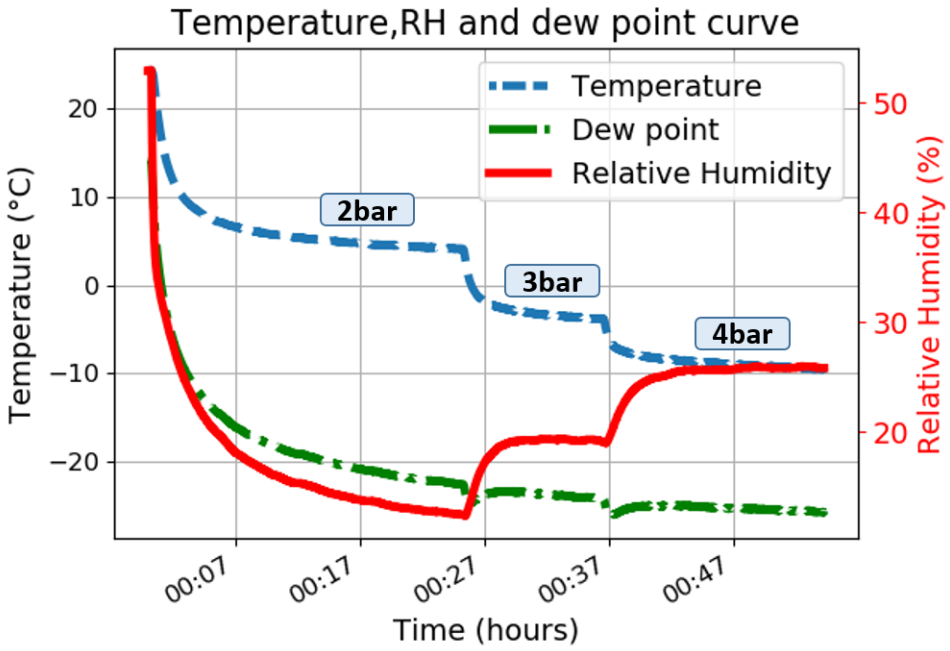


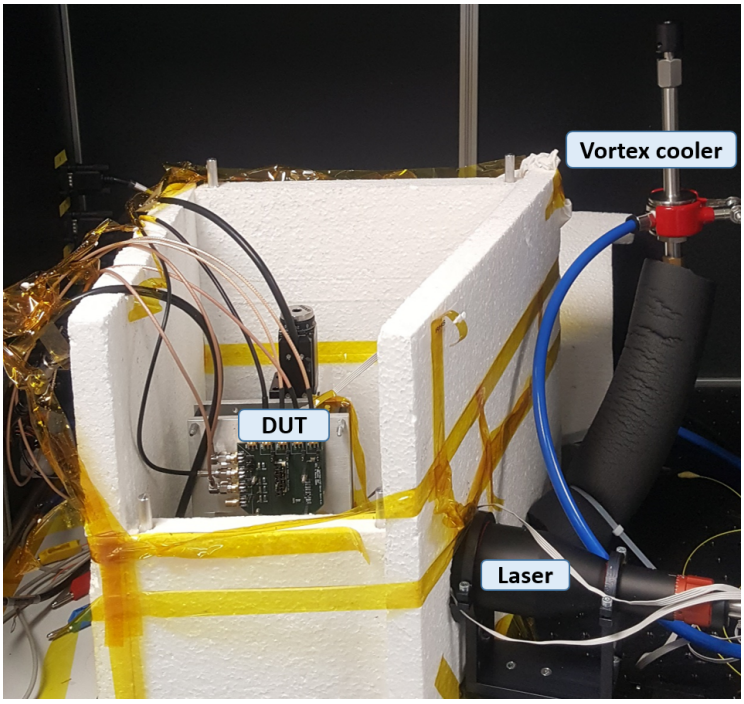
Figure 4.7: Plots from the humidity and temperature sensor that is placed on the back of the PCB as the setup is being cooled down [56]. To make sure the cooling is smooth and the dew point is always a few degrees below the temperature, the setup is cooled in steps of increasing pressure until it is cold enough. The dew point estimation is done using an approximated Magnus formula [51].

leaks were sealed up as much as possible with Kapton tape, but inevitably there will always be some, especially around the laser. The pipe blowing cold air onto the back of the chip can be seen in Figure 4.8b. This is the output of the vortex cooler. To monitor the temperature and humidity, a sensor was placed on the back of the PCB, but a bit further away from the main cold air stream, to make sure the environment around the chip is cold and dry (Figure 4.7).

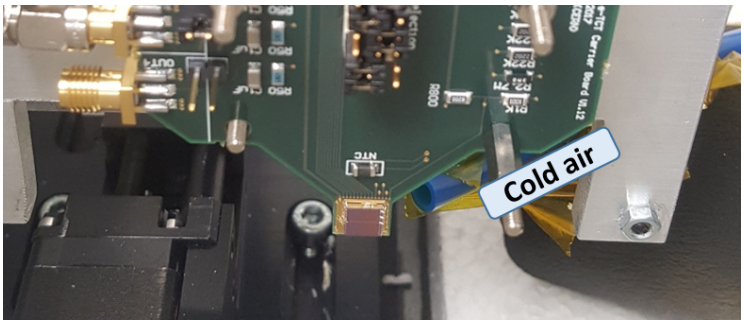
A temperature of $-10\ °C$ and a leakage current similar to the non-irradiated chip at room temperature was reached. This shows that the device is cold enough to be operable and almost no annealing would occur during the E-TCT experiment.

4.1.4 Absolute position of depletion region

The E-TCT technique gives an image of the depletion region of the device. However the absolute position of that region relative to other components in the chip is not determined by the measurement. This information is useful since it allows to compare the depletion region not just in depth, but as a 2 dimensional map along



(a)



(b)

Figure 4.8: (a) A photo of the setup used for E-TCT with cooling provided from a vortex cooler along with a polystyrene insulation enclosure. (b) A close-up picture of the chip and the pipe blowing cold air behind it [56].

the surface of the chip. All chips have metallization layers on their surface, which are

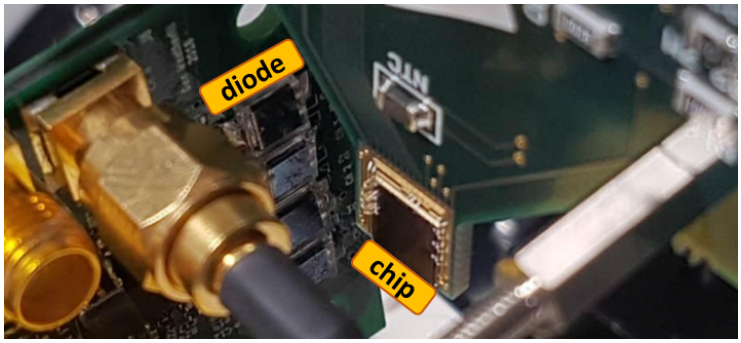
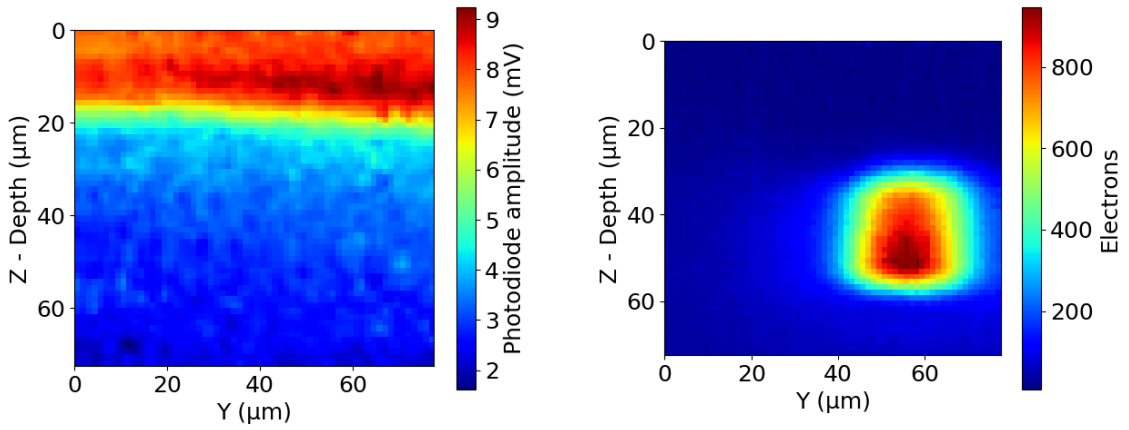


Figure 4.9: A photo of the chip with the photodiode behind it (relative to the laser).

used to interconnect the inputs and outputs of the various implants. The amount of metallization is specific to each chip and for the Investigator chips it is $\sim 10\,\mu$m. This layer is expected to offset the depletion region relative to the surface of the chip. To measure this offset a photodiode is placed near the side of the chip, on which the laser is not shining. A photo of the setup is shown in Figure 4.9. Both the chip under test and the diode are connected to an oscilloscope and their data is taken simultaneously. When the photodiode is not detecting light, it means that it is within the "shadow" of the chip and when the output rapidly increases, it means that the boundary of the chip surface is reached. The output from the two channels is shown on Figure 4.10.

The photodiode is placed behind the chip and only a small amount of defocused light is reaching it. Furthermore the laser power is adjusted to almost the lowest setting in order to simulate a low enough output in the pixel. This causes the photodiode signal to be low compared to its noise. Nevertheless a clear boundary marking the position of the chip surface can be distinguished. To amplify that boundary a Gaussian filter is applied to the scan from the photodiode. It is also possible that the chip surface is not completely horizontal. Therefore only the columns over the pixel are used and averaged in Y. The result is a sigmoid function (along Z) and the middle point is taken as the chip surface. All E-TCT results presented from here have the position $Z = 0$ of the chip surface determined following this method. This technique does not work as well for pixels far away from the edge of the chip, as the boundary becomes too defocused.



(a) 2D raster scan from channel connected to the photodiode

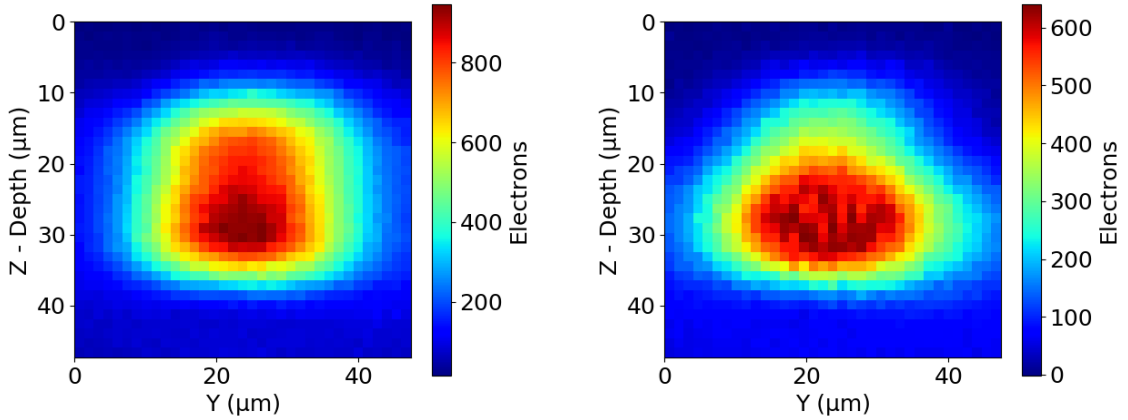
(b) 2D raster scan from channel connected to the pixel output

Figure 4.10: Images of the same scan of a non-irradiated mini-matrix 11 as detected by the photodiode and the chip - (a) is showing the output from the photodiode behind the pixel and (b) is showing the the output from the pixel onto which the laser is focused, which is also the final output of the E-TCT technique. The values in (b) are converted to electrons using the gain curves in Figure 3.11.

4.2 Comparison of depletion regions before and after irradiation

Using the setup described above, the depletion regions of the irradiated to 1.2×10^{15} 1MeV $n_{eq}\,cm^{-2}$ and non-irradiated Investigator chips were measured. The data was taken on mini-matrix 11 as it has the closest characteristics to MALTA [24] out of the diode reset mini-matrices. The pixel is positioned in the outermost mini-matrix on the second to last column within that mini-matrix. This would result in a rough distance of $\sim 100\,\mu m$ to the edge (including the guard ring). The results are shown in Figure 4.11.

Figure 3.1b shows that in the Investigator devices there are n^-, p^- and p^{++} layers. The expected operation of the device is that the depletion region grows in the n^- and p^- due to the low doping and stops at the high doped p^{++} layer. The n^- layer just needs to encompass the deep p-wells, therefore its thickness is roughly ~ 2 to 3 μm. The p^- layer extends to 25 μm in the silicon and then the p^{++} layer fills the remainder of the pixels that is 100 μm thick. At $-6\,V$ on both the p-well and the back substrate, the device is expected to depleted only within the p^- layer.



(a) Non-irradiated mini-matrix 11 (b) Irradiated mini-matrix 11

Figure 4.11: Measured depletion regions for the non-irradiated and irradiated case of the same Investigator2 samples, which were presented in chapter 3. The laser power is adjusted to give similar outputs, which were converted to electrons using the previously calculated gain curves.

Since the resolution of the laser is $\sim$ 5 μm, this expected depletion depth is close to the limit of the technique. Most of the devices measured using E-TCT have a sensitive area of $\sim$ 100 μm. Nevertheless, the results match the expectation very well, showing that the epitaxial p^- layer is depleted.

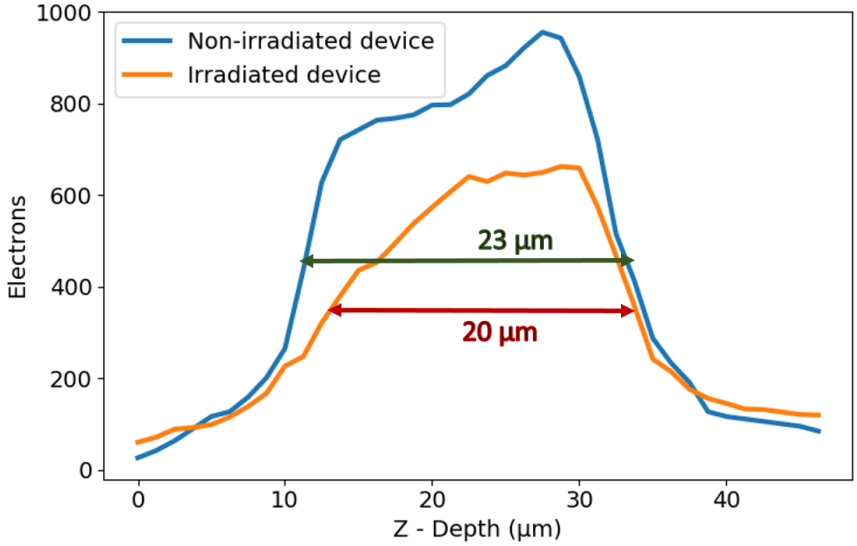


Figure 4.12: One dimensional slice of the depletion region 2D scan along Z at Y = 24 μm for both the irradiated and the non-irradiated device. The calculated full width at half maximum is taken as the depletion region depth.

If the approximation that the depletion region is similar to a step function holds,

then the way to measure its depth is to use the full width at half maximum along the Z dimension at the pixel centre (Y = 24 μm in Figure 4.11). The central slices for both devices are shown in Figure 4.12. The error in this case should be taken as $\pm\sigma$ of the edge at lower Z. This works out as 23 ± 4.5 μm for the non-irradiated case and 20 ± 6.5 μm for the irradiated. However, it is possible that the main difference is caused by a difference in shape of the sensitive region, rather than just a reduction in depletion depth. The small size of the pixel relative to the laser spot makes it hard to discriminate between the two options. To understand this better, the technique applied on the Investigator chip was simulated using Technology Computer-Aided Design (TCAD) simulation.

4.3 TCAD simulation of the depletion region

TCAD is used for simulating semiconductor devices and their electric field structures, currents, charges, potentials, etc. It was used extensively to confirm the principle of depletion region generation when the additional n^- layer was inserted in the Investigator1 modified process. Most detectors are simulated with TCAD before fabrication by a foundry. The exact layout parameters and doping of the implants are a trade secre5 and a special license is needed to use them. However, approximations of the doping parameters can be distributed by the designer, which are the values used in the thesis. The depletion region is created by the back substrate, p-wells, n^- and p^- layers. The charge is collected in the highly doped n^{++} collection capacitance. These are the main features of the pixel needed for E-TCT.

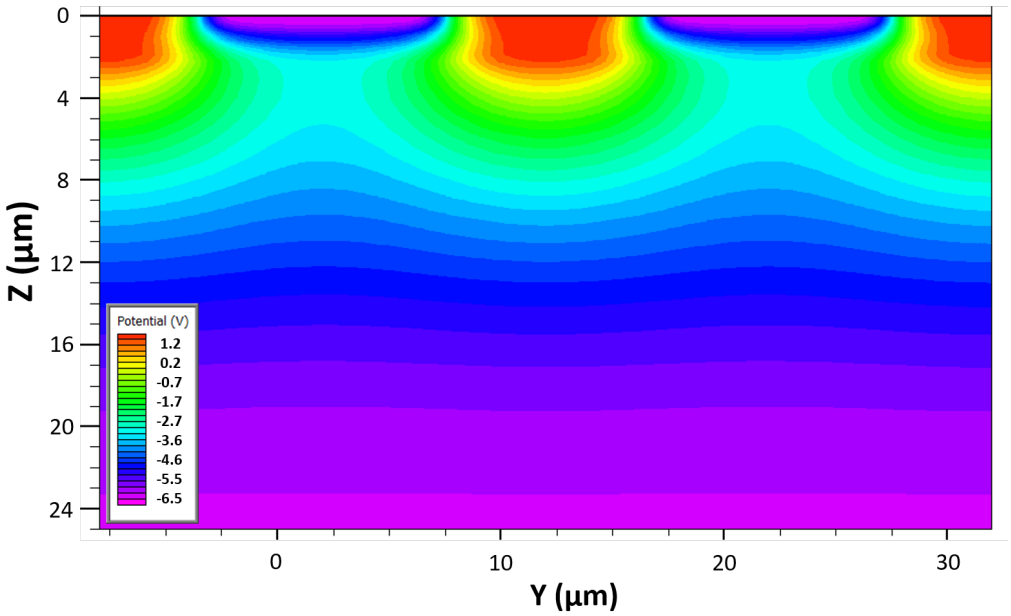
The detector design was simulated using the parameters of mini-matrix 11. In particular, this means using a collection electrode size of 3 μm $\times$ 3 μm, pixel pitch of 20 μm and spacing of 3 μm. The thickness of the epitaxial p^- layer is set to 25 μm. The doping of the n^{++} collection electrode and the p^{++} layer are modelled to be $10^{18}/cm^3$ of their respective doping types. The n^- layer just covers the p-wells and is ~ 2 μm as shown in [61]. Considering the measurements in this chapter, the depletion depth extends roughly to 21 μm within the p^- layer. Using Equation 2.12 for the acceptor concentration only would imply that the p^- doping is $\sim 1.7 \times 10^{13}/cm^3$, as the device is almost at the depth at which the depletion region saturates. This is also slightly higher than the value given for minimal doping mentioned in [61]. Since the n^- layer has to deplete an order of magnitude less distance, it should have an order of magnitude higher doping according to Equation 2.8. To confirm

that the approximated doping parameters are sufficiently accurate, the simulated electrostatic potential was compared to the one done with the exact parameters of the chip in [61] (see Figure 4.13).

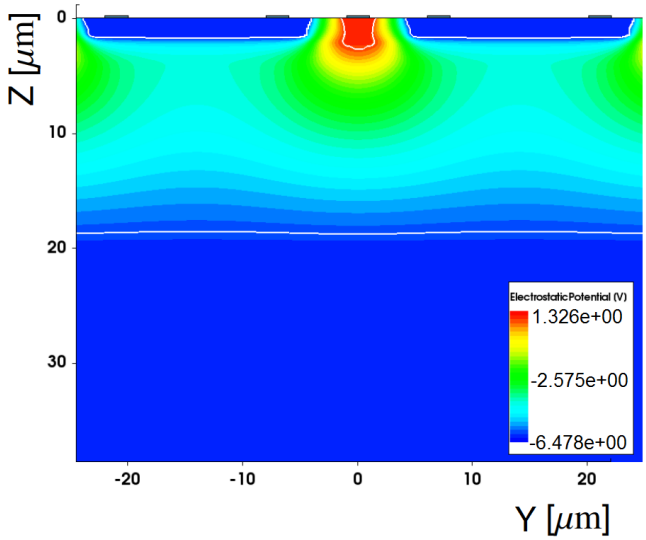
The approximated setup for the simulation ended being a 40 μm region covering 1 total pixel in its centre and half a neighbouring pixel on each side. The top 3 μm are n^- doped with $1.5 \times 10^{14}/cm^3$ and the next 22 μm are p^- doped with $1.7 \times 10^{13}/cm^3$ to reach the full 25 μm epitaxial layer thickness. Afterwards there is the p++ substrate doped to $10^{18}/cm^3$. The implants are n++ ($10^{18}/cm^3$) the collection electrode and the deep p-well doped with p++ ($10^{18}/cm^3$). Both implants are extending 2 μm in depth. The operating point is initialized at a voltage of $1\,V$. The collection electrodes are the highest potential on both simulations. Between them the p-wells are kept at -6V via electrodes on the chip surface. The values and shapes of the constant potential lines are the same in both cases, which would result in the same electric field structure. Therefore these results support the usage of this simulation setup to predict the electric field and the result of the E-TCT technique.

The E-TCT simulation was done by creating a photogeneration area of similar size to the laser spot (5×5 μm). The area was moved in steps of 1 μm of the whole YZ plane. There is a probe on the collection diode detecting induced charge as in [61]. The amount of photogeneration was adjusted, such that the maximum collected charge is similar to the output of the E-TCT in number of electrons as described in subsection 3.2.2. The number of collected electrons is plotted for each YZ position. There is 10 μm of empty space added on top of the picture to make it the scales identical to Figure 4.11 and account for the metallization layers. A Gaussian filter was applied to the final image to remove effects from the mesh density in TCAD. The results are shown in Figure 4.14.

The simulated depletion region agrees with the experimental results shown in Figure 4.11a. In both cases the maximum number of electrons is collected when the laser is shining at a lower depth (higher Z). This can be explained by considering the electron concentration while inputting constant photogeneration, as shown in Figure 4.16. The same simulation for two different photogeneration sites illustrates the origin of the difference. In the region below the p-wells electrons are less concentrated in the "far" case (shown in Figure 4.16a) than in the "close" case (shown in Figure 4.16b). The large laser spot produces a large charge cloud, which would expand due to inter-electron interactions. The almost constant potential in the Y dimension makes the lateral electric field low and allows the spread of the charge



(a) A 2D electrostatic potential map of mini-matrix 11. Collection electrode centres are at Y = − 8 μm, 12 μm and 32 μm.



(b) A 2D electrostatic potential of a mini-matrix with pixel pitch of 28 μm, spacing of 3 μm and collection electrode width of 2 μm at Y=0 μm.

Figure 4.13: Simulated electrostatic potential within the pixel. The plane is taken at the centre of the pixel in the X dimension. In the simulation the metallization layers are not present, therefore Z=0 starts at the top of the silicon (equivalent to 10 μm in Figure 4.11). There are − 6 V applied to both the p-wells and the back substrate. In (a) the potential of mini-matrix 11 is simulated. In (b) a simulation done with the exact doping parameters is done on a different mini-matrix and presented in [61].

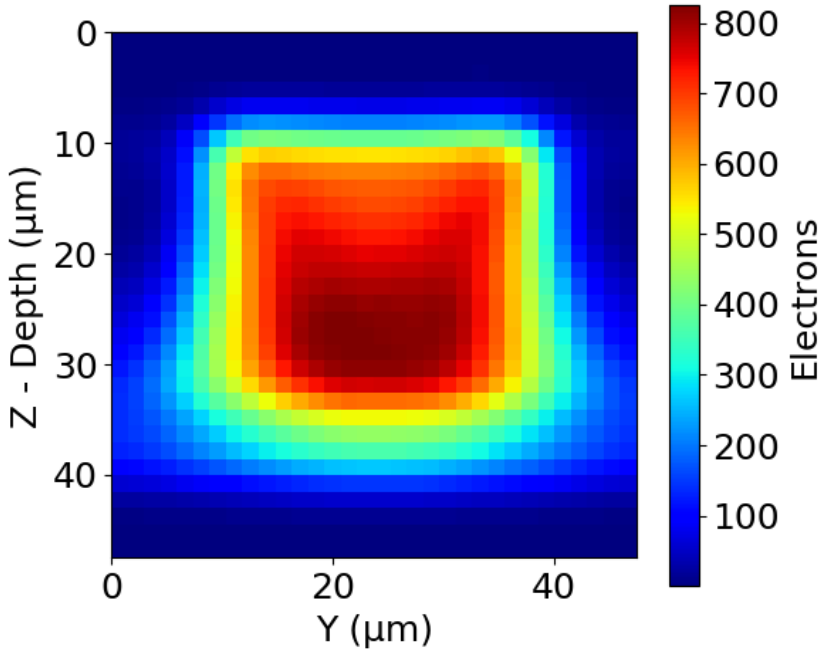


Figure 4.14: Simulated E-TCT output at bias voltage $-6\,V$ of mini-matrix 11 using TCAD.

cloud. Due to the symmetry of the device there is an area of low electric field below the p-wells as shown in Figure 4.15. Electrons that end up in that low E-field area would not contribute as much to the total charge induced in the collection electrode and have a higher probability of recombination due to the lower drift speed. For the "far" case, the mushroom shaped constant potential lines in Figure 4.13a concentrate the charge cloud and reduce the number of electrons that end up in the low E-field regions below the p-wells. This explains the slight positive gradient as Z increases when the E-TCT is done on the non-irradiated mini-matrix of the Investigator2 sample. It is also the main cause of the inefficiencies in the corners of MALTA and mini-MALTA [24, 34], although in those cases the pixel pitch and p-well cutout are different.

When the silicon is irradiated, charge traps are created and the probability for electrons to get trapped or recombine increases. From the fact that the capacitance before and after irradiation are equal within error (see section 3.3), it can be inferred that the effective dopings are similar as well using Equation 2.17. However, it is possible that small doping changes affect the low electric field regions below the p-wells slightly. Additionally the charge traps and higher recombination rate, decrease the probability of full charge collection at the same regions for even higher electric fields, effectively increasing the area of the insensitive region. The result of these

effects is clearly seen as inefficiencies in the corners of the pixel [24]. It is also the reason for the shape of E-TCT output observed in Figure 4.11b. The lack of sensitivity just below the p-wells gives the thin neck around the collection electrode near the chip surface at low Z.

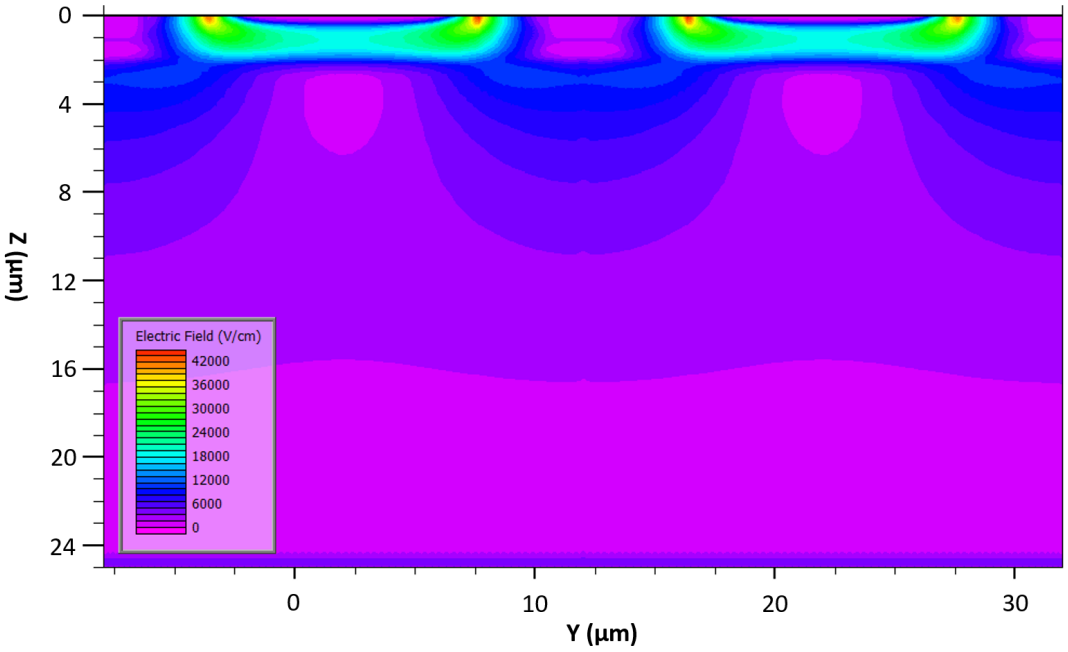
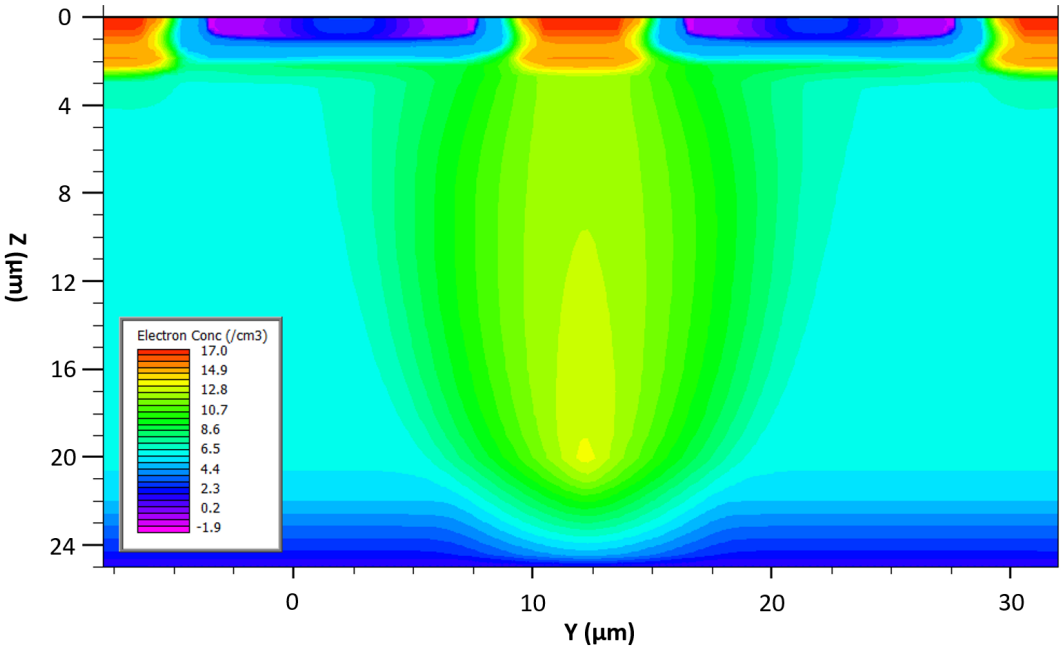
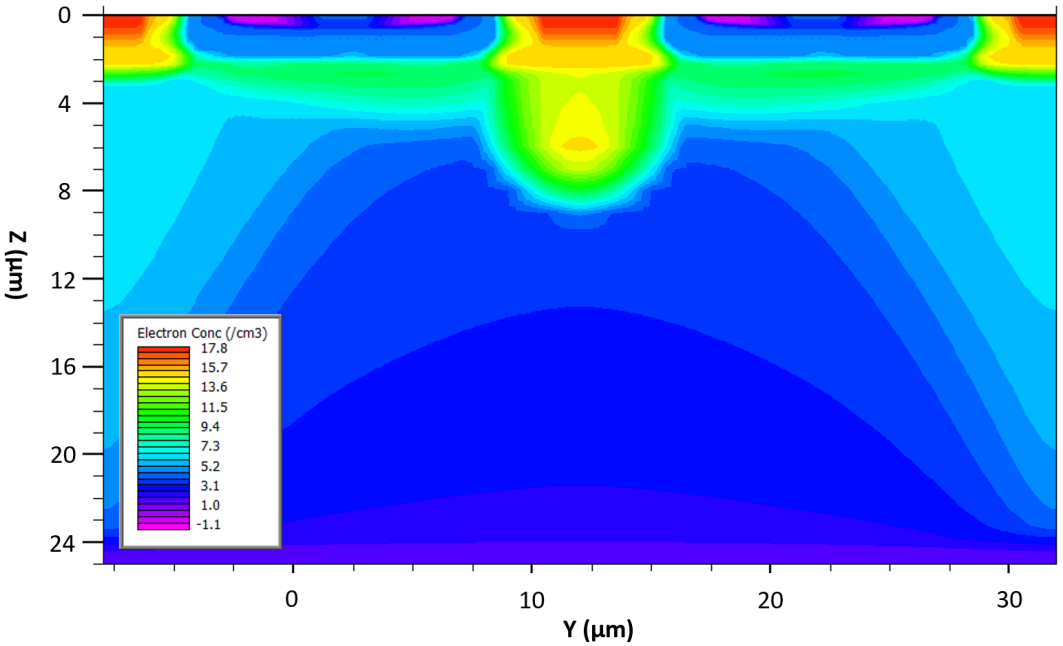


Figure 4.15: Absolute value of the electric field simulated for mini-matrix 11. The shape is consistent with Figure 8.10 in [61].



(a) Photogeneration centre at Z = 20 μm



(b) Photogeneration centre at Z = 6 μm

Figure 4.16: In (a) the electron concentration with bias voltage $-6\,V$ is plotted when the centre of the photogeneration area is far away from the collection electrode at Z = 20 μm and on the central axis (Y = 12 μm) . In (b) the same simulation is ran with the photogeneration centre still being central but at Z = 6 μm.

4.4 Estimation of the depletion region depth using MIPs

Particles with energy close to the energy of a MIP, traverse the silicon and deposit charges along the way. The charges that are outside the depletion region recombine and are mostly not collected and detected. Therefore the effective detector thickness is the depletion region depth. The amount the charge deposited depends on the detector thickness as shown in Equation 2.3. Thus using a source of MIPs, the depletion region depth can be estimated. The most common source used for MIPs is the ^{90}Sr. In chapter 2 it is shown that the expected energy deposition distribution from that source into silicon is a Landau-Vavilov distribution with a most-probable value being $\approx$ 76 e^- for every μm of depletion region thickness. This approximate value is reached by assuming the electrons from the ^{90}Sr are MIPs, thus neglecting the whole energy spectrum of the 3-body decay, the additional energy lost to Bremsstrahlung radiation due to the lower electron mass and the change in the scattering amplitudes due to the two interfering indistinguishable scattering possibilities of e^-- e^- scattering. Using the gain curves measured in subsection 3.2.2, the parameters of the Landau distribution, which is measured in volts, can be converted to number of electrons. From the most probable value in electrons, an estimate of the depletion depth of the detector can be obtained.

The averaged used conversion factor of $3.69\,eV$ creating one electron-hole pair [36] inevitably has fluctuations. There is additional capacitance on the readout chain from the collection electrode to the oscilloscope that contributes to the noise. Since the pixels under test are small, it is also possible to collect shared charge from neighbouring pixels. All these effects are accounted for by convoluting the Landau function with a Gaussian function. This introduces an extra parameter to fit - the standard deviation of the Gaussian function. The effect of the convolution is illustrated in Figure 4.17 with simulated example data.

Data is collected on mini-matrix 11 for both the irradiated and non-irradiated Investigator2 samples using a ^{90}Sr source. A Gaussian convoluted Landau function is used for fitting both irradiated and non-irradiated datasets as shown in Figure 4.18. Errors are given from the covariance matrix of the fit. The parameter of interest is the position of the most probable value (mpv), as it is used to estimated the depletion depth. To get a value in micrometers, the mpv from the fit is converted in e^- using the gain curve. The errors on the gain curve and Landau fit are added

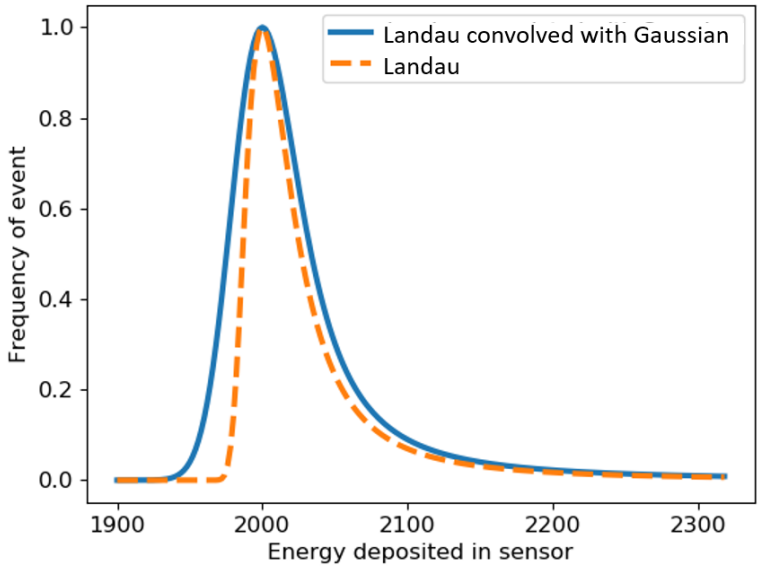
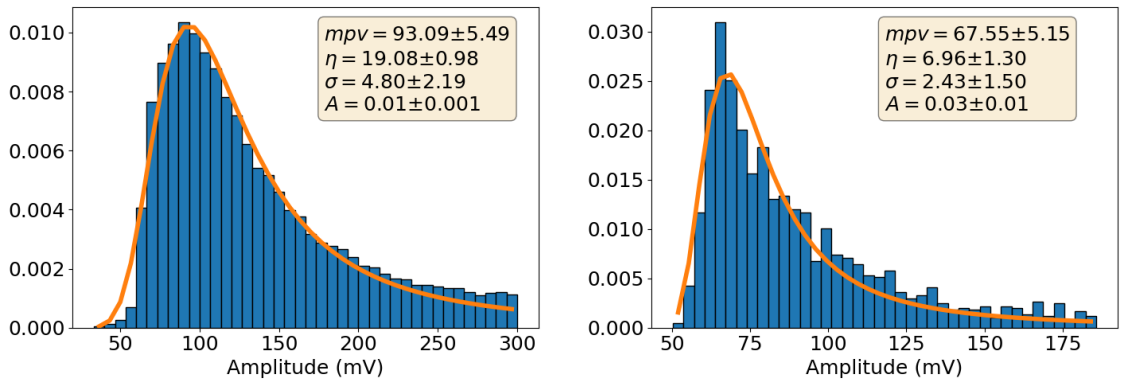


Figure 4.17: Example plots of a Landau with $mpv = 2000, \eta = 10, Amplitude = 1$. The orange dashed line is a pure Landau and the blue one is a Landau convoluted with a Gaussian with $\sigma = 15$.

as uncorrelated. The result is then divided by 76 e^- to get the depletion depth in μm. The depletion depth for the non-irradiated and irradiated device was estimated to be 22 ± 1.6 μm and 19 ± 2.1 μm respectively. These values agree very well with the rough estimation of the depletion region using full width at half maximum performed in section 4.2. The slightly different values could be caused by corner inefficiencies making the effective depletion region slightly smaller. The corner inefficiencies reduce the charge sharing, which results in smaller fluctuations in the energy deposition, since the incoming charge shared electrons are obstructed by the low electric field regions. This causes the narrower Landau shape (lower η parameter) of the irradiated sample.

4.5 Summary

In this chapter the depletion region of the Investigator2 was measured on two different samples - one non-irradiated and one irradiated to $1.2{\times}10^{15}$ 1MeV n_{eq} cm^{-2} and 140 Mrad(Si). Two different techniques were used that give very similar results for the depletion depth. One of them (E-TCT) also provides information about the shape of the depletion region. It can be seen that the main difference between irra-



(a) Non-irradiated mini-matrix 11

(b) Irradiated mini-matrix 11

Figure 4.18: Normalised histograms of data taken with ^{90}Sr on mini-matrix 11 for an irradiated and non-irradiated Investigator2 sample. A Landau distribution convoluted with a Gaussian profile is fitted to both.

diated and non-irradiated devices is the low efficiency region at the pixel corners due to the low electric field below the p-well centres. This is the same effect observed in [24] and chapter 5. Thus it can be concluded that the depletion region depth is not significantly changed with this amount of irradiation and the main difference due to irradiation is the development of larger regions where charge is not collected.

Chapter 5

X-ray test-beam measurements of the charge collection shape

The mini-MALTA chip is designed with two modified layout types to combat the corner inefficiencies observed in MALTA [24]. This chapter is about a test-beam done at Diamond Light Source to measure precisely these inefficiencies and to guide possible design modifications. There are multiple mini-MALTA irradiated samples with different type and amount of irradiation compared using the same setup. The results of this chapter have been published in [57].

5.1 The mini-MALTA prototype

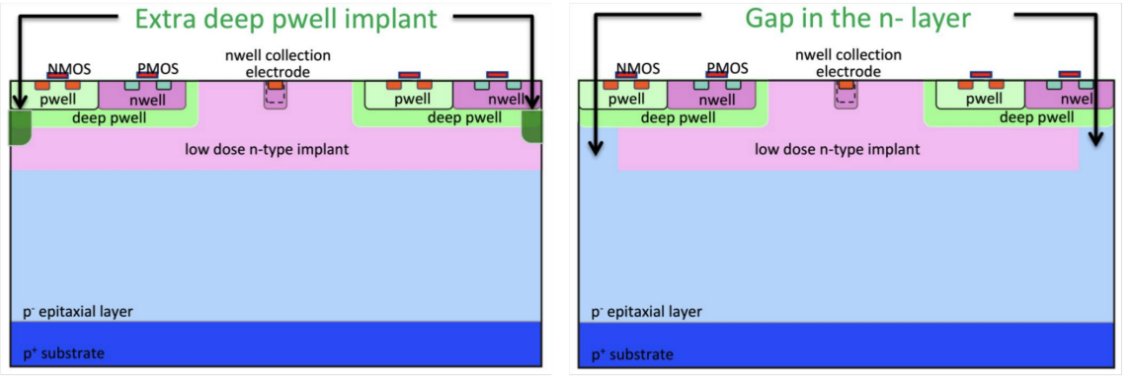


Figure 5.1: Process modification in mini-MALTA. Figure from [85].

The mini-MALTA device is a depleted monolithic sensor prototype, with 64×16 square pixels of 36.4 μm side. It is based on the design of the MALTA chip, which

was a full-sized CMOS demonstrator. The problem with the MALTA chip that mini-MALTA is designed to solve is an inefficiency in the pixel corners after irradiation. Mini-MALTA has eight sectors which differ in their front-end design, reset mechanism and in-pixel layout. In particular, there are two process modifications which have been introduced in mini-MALTA and are shown in Figure 5.1. The aim of these two modifications is to improve charge collection at the pixel edges. The first variant has an extra deep implant of p-type silicon and the second has a gap in the n-type layer at the same position. TCAD simulations of the new designs [59] have shown that both designs result in the same electric field lines, leading to an improvement in the performance of the "old" continuous n^- layer design (Fig 5.2). The modification changes the shape of the potentials and reduces the area with low electric field shown in Figure 4.15. Thus there are no regions with low drift velocity that have an increased probability for charge trapping and recombination when the sample is irradiated. Regarding the simulation, there is no preference over the modification (gap in n^- layer or extra deep p-well), since they produce equivalent electric field structures.

The main goal of the test-beam at Diamond Light Source is to study the performance of these two new designs in mini-MALTA and compare their performance to MALTA for different levels of irradiation. There were five chips tested irradiated at two different places - neutrons at the TRIGA reactor in Ljubljana [47] and protons at the MV40 cyclotron at Birmingham [15]. A summary of the samples is given in Table 5.1. The annealing on sample W5R9 was done to decrease the overall noise and leakage current before the test-beam started. All the equivalent neutron values are calculated in 1 MeV n_{eq}/cm^2 and the TID doses are estimated for silicon (Si).

5.2 Experimental Setup

The measurements were performed at Diamond Light Source using beamline B16. A photo of the set up in the beamline is shown in Figure 5.3a. The mini-MALTA chip is located on a printed circuit board (PCB), which is mounted onto a an aluminium chuck with thermal contact ensured. The design of the cooling system, which was developed in Oxford, is shown on Figure 5.3b. It consists of a water-cooled chuck, reaching a temperature of $\sim 10\,°C$. The aluminium is used to cool the warm side of a Peltier chip, while the cold side of the Peltier element is connected to a cold adapter plate. Plastic screws are used for mounting the PCB, to avoid unnecessary thermal

Sample	Epitaxial Thickness (μm)	Irradiation	Fluence (n_{eq}/cm^2)	TID (MRad)	annealing
W2R11	30	none	0	0	none
W2R9	30	23 MeV protons	5×10^{14}	66	none
W2R1	30	1 MeV neutrons	1×10^{15}		none
W5R9	25	23 MeV protons	5.6×10^{14}	74	120 min at 35 °C
W4R9	25	23 MeV protons	7×10^{13}	9	none

Table 5.1: Mini-MALTA samples with their respective delivered dose in neutron equivalent fluence and TID.

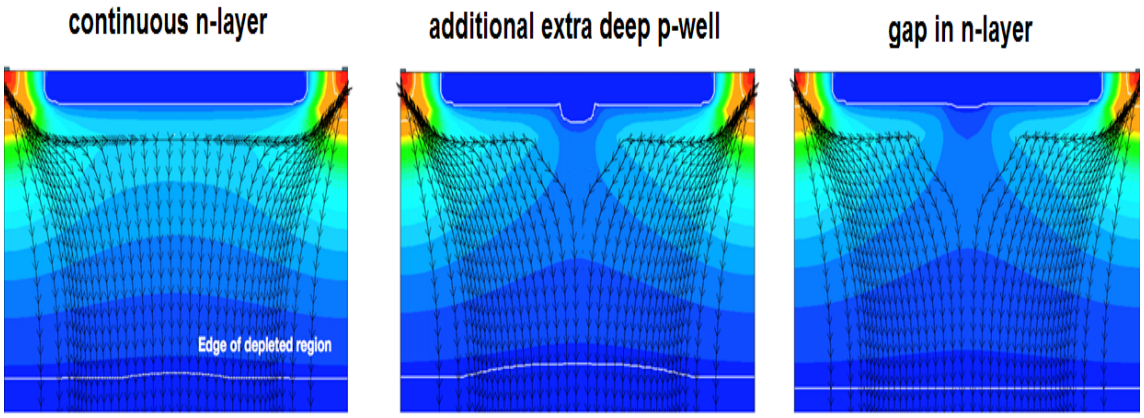
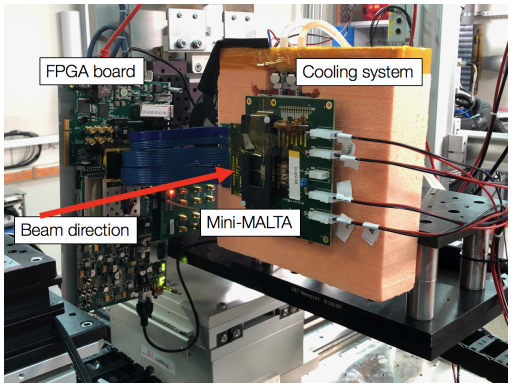


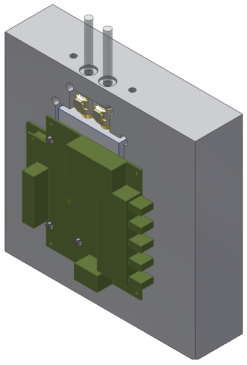
Figure 5.2: TCAD simulation of modified designs compared to the original continuous n^- layer. The contour plots show the relative potential and the arrows show the direction of the electric field. The centre of the plots is the pixel edge, rather than the pixel centre like the ones in Figure 5.1. Figures from [59].

losses. The cooling system is able to keep the device at a constant temperature of $-13\,°C$, as measured by a temperature sensor on the back of the chip.

The X-ray beam was focused using a Compound Reflective Lens (CRL) X-ray mirror arrangement to a beam spot of 2 μm (FWHM), as measured using a knife edge technique. The mini-MALTA chip was mounted on a motion stage, which was placed at the location of the focal point of the X-ray beam. The device was read



(a) Experimental setup in the beamline.



(b) CAD drawing of the cooling system with the attached mini-Malta PCB.

Figure 5.3: Photo (a) and CAD drawing (b) of the setup designed to allow 3D movement of the sample whilst being kept cold. A foam cover is set on top of the PCB when it is in use.

out using a Kintex KC705 Field Programmable Gate Array (FPGA) board, which communicates via UDP protocol with the control computer.

The beam energy was chosen to match the energy a MIP deposits across the depletion region of a mini-MALTA. The stopping power for a MIP in silicon is roughly [88]:

$$\left\langle \frac{dE}{dx} \right\rangle \simeq 3.88 \ \frac{\text{MeV}}{\text{cm}}. \tag{5.1}$$

Mini-MALTA is expected to have a depletion depth of between 19 and 24 μm, depending on chip properties, biasing voltages and levels of irradiation. This means that a MIP would deposit between 7.3 and 9.3 keV in the device. X-rays of that energy would still primarily interact with the photoelectric effect, thus the X-ray energy needs to match that interval. Since it is difficult to change the beam energy during the test-beam, an energy of 8 keV was chosen.

The full beam intensity is more powerful than the readout capabilities of the chip readout. Therefore to make more reliable measurements, the beam was attenuated by placing a 0.5 mm of aluminium before the device. The measurement consisted of moving the detector in the X and Y directions (as labeled in Figure 4.1) with steps of 2 μm. The precision of the motors is 400 nm, but decreasing the step, increases the time of the scan quadratically. Data taking was done for 1 second at each step of the motion stage. An area of 100 $\times$ 100 μm^2 was scanned to make sure the scan

fully contains a set of 2 × 2 pixels. Diamond Light Source also provides a monitor of the current in the synchrotron ring, which is used to adjust all the measurements for better precision.

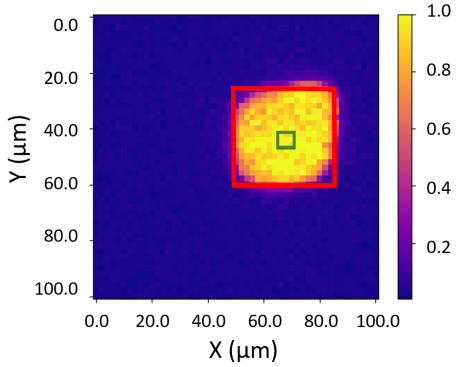
5.3 Analysis of the pixel response

One of the differences with a usual charged particle test-beam, is that the focused X-rays allow for an easier and quicker analysis, due to the lack of multiple detector planes and synchronization of events. The response measured with a photon beam is different from the efficiency determined using a charged particle test-beam, since photons deposit energy via the photo-electric effect. However, a comparison is drawn in section 5.5. The analysis for the Diamond test-beam is done by looking at each pixel individually, as if all the others were masked, and then combining the results to give a response map of the device.

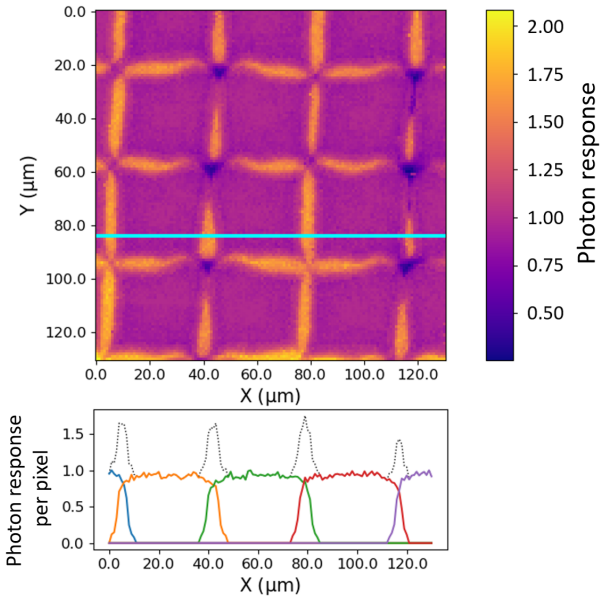
5.3.1 Single pixel response

The design of the TowerJazz family chips does not include an output of the energy deposited (commonly measured with the time over threshold technique [90]). The only output out of the digital side of the device is the position of the hit pixels. The number of hits in a pixel was recorded at each motion stage position. Data is plotted in a 2D histogram with bins being the motion stage positions. An example is shown in Figure 5.4a, where the shape of the sensitive area of the pixel can be seen. To find the best fit for the area of a pixel, the centre of the pixel is used. It is identified by applying a Gaussian filter [94] to the image and picking the location with the maximum value. Then, the average number of hits is found in a small region around the pixel centre, which is the small green square in Figure 5.4a. Under the assumption that the centre of each pixel is 100% efficient, the number of hits in each pixel was normalised to that value. This removes possible variation between pixels that could be caused by a slight difference in the source followers that make the effective threshold of the pixel different. Taking the average of a region around the pixel centre also accounts for variations in the number of hits per step of the motion stage in the raster scan. Subsequently, the average normalised number of hits was calculated within the pixel area (36.4 x 36.4 μm^2), which is the larger red square in Figure 5.4a. This is then defined as the in-pixel photon response. The uncertainty

on the response is defined as the standard deviation of the number of hits in the normalisation area, i.e. the green square.



(a) The green square shows the area of the pixels used to normalise the response. The red square is the expected pixel area.



(b) Example of a summed response map and profile of the pixel response along the blue line. The response for each pixel is shown in a different colour and the total response is shown as a dashed line.

Figure 5.4: Response map for one pixel (a) and for all pixels in one scan (b) of a non-irradiated device with the continuous $n-$ layer

5.3.2 Pixel response maps

The measurements and the evaluation of the response outlined above are repeated for each pixel in the scan and the responses are averaged across the pixels in the scan. When combining all the pixels, their red squares are checked for overlaps. The lack of overlaps confirms that the correct pixel centres were found. The X-ray beam has a halo region of a few hundred micrometers, which causes constant background hits in the single pixel response. Therefore motion stage positions that record less than 7% of the hits in the pixel centre were set to zero. This removes the constant background. The photon response calculations are done before the background cut, even though the results are not affected by the choice of cut, as the background extends outside the pixel area. The removal of background is implemented to keep the normalisation (100% in the pixel centre) when adding the single pixel response

maps together. An example of the summed response map is shown in Figure 5.4b. The bottom panel of 5.4b shows a one-dimensional profile along X of the pixel response at a particular Y location. The response for each pixel is shown in a different colour, and the total pixel response is shown as a dashed line. There is clearly some overlap between the pixels, and the total pixel response reaches more than 100%, which is indicative of charge sharing. There is a more detailed discussion on charge sharing in section 5.4.

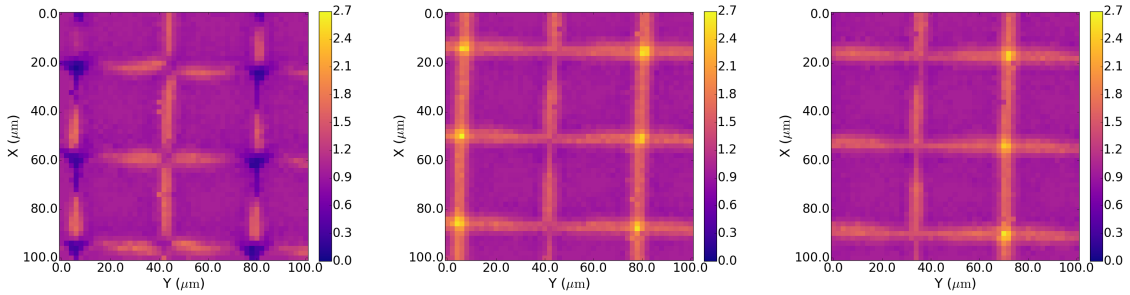
5.3.3 Pixel response as a function of radiation dose

The pixel response maps are compared between samples with different irradiation doses. The data for all the tested samples with the three different layouts is presented in Table 5.2. The most accurate comparison is between the three sample of the same wafer (wafer 2) - W2R11, W2R9 and W2R1. In such a comparison there is less intrinsic variations in the silicon properties such as resistivity and depth of the epitaxial p^- layer. The images for these three samples with the three layouts is shown in Figure 5.5.

Sample	Fluence n_{eq}/cm^2	TID (MRad)	continuous n^- response (%)	extra deep p-well response (%)	n^- gap response (%)
W2R11	0	0	88.3 ± 2.4	90.5 ± 2.2	90.9 ± 2.2
W2R9	5e14 (p)	66	81.2 ± 2.8	87.6 ± 4.2	88.4 ± 3.8
W2R1	1e15 (n)	0	75.4 ± 3.8	90.5 ± 2.8	89.0 ± 3.1
W5R9	5e14 (p)	70	80.4 ± 2.8	89.0 ± 2.5	89.3 ± 2.2
W4R9	7e13 (p)	9	78.7 ± 2.6	89.8 ± 2.3	89.9 ± 2.3

Table 5.2: Calculated average pixel responses for the different samples and designs. Table from [57].

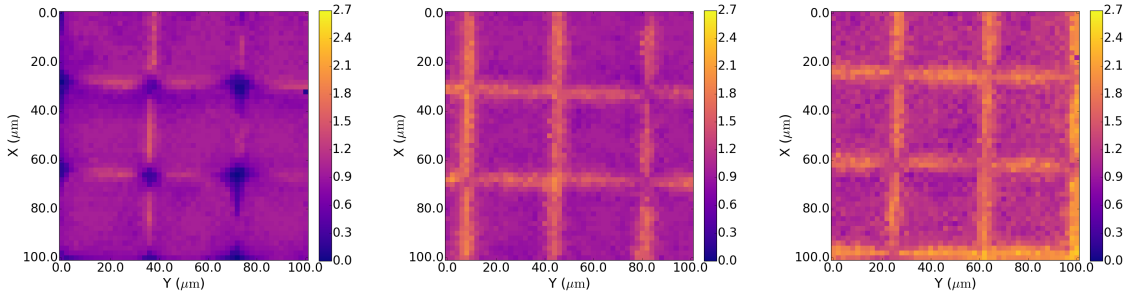
In Figure 5.5a and Figure 5.5g the non-irradiated and neutron irradiated samples with the continuous n^- layer region are shown. This is the same design as in the MALTA chip, which showed corner inefficiencies in [24]. A similar shape and response reduction can be seen here. While the non-irradiated pixels are almost fully responsive, large gaps in the response can be observed around the corners and



(a) W2R11 continuous n^- layer, non-irradiated

(b) W2R11 extra deep p-well, non-irradiated.

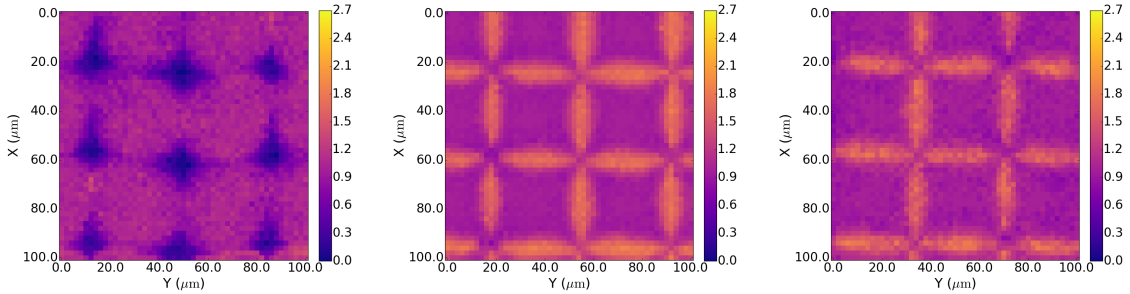
(c) W2R11 n^- gap, non-irradiated



(d) W2R9 continuous n^-, 5×10^{14} n_{eq}/cm^2

(e) W2R9 extra deep p-well, 5×10^{14} n_{eq}/cm^2

(f) W2R9 extra deep p-well, 5×10^{14} n_{eq}/cm^2



(g) W2R1 continuous n^-, 1×10^{15} n_{eq}/cm^2

(h) W2R1 extra deep p-well, 1×10^{15} n_{eq}/cm^2

(i) W2R1 n^- gap, 1×10^{15} n_{eq}/cm^2

Figure 5.5: Pixel response maps for the different samples. For each sample the continuous n^- layer, extra deep p-well and n^- gap sector are shown. W2R11 is non-irradiated, W2R9 is proton-irradiated to 5e14 n_{eq}/cm^2 and 66 Mrad (Si) and W2R1 is neutron-irradiated to 1e15 n_{eq}/cm^2. Figure taken from [57].

the edges of the irradiated samples. The overall response decreases by a factor of $\sim$ 10% as can be seen from Table 5.2. A similar trend is also seen in the mini-MALTA test-beam at ELSA [34].

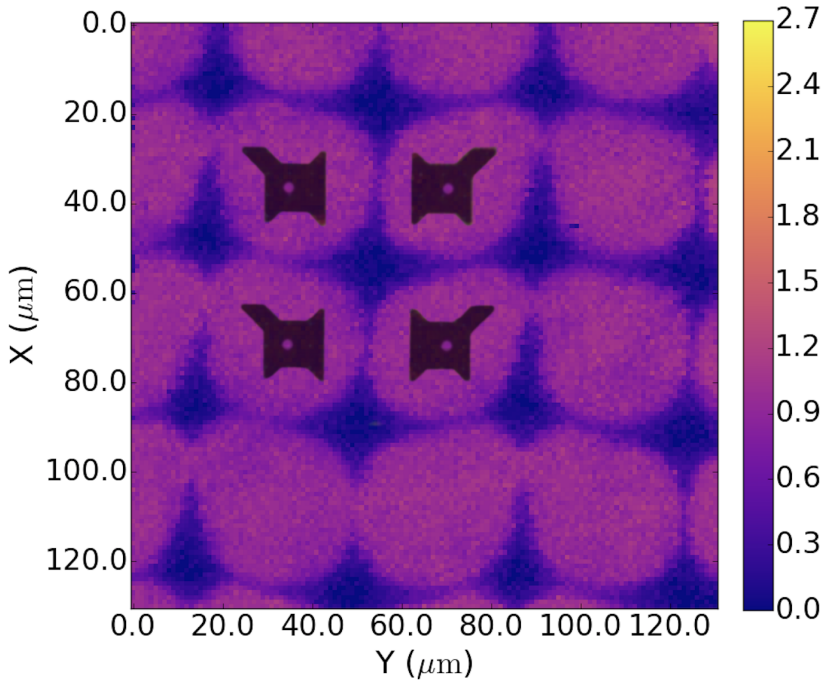


Figure 5.6: Overlay of the scan of the continuous n^- sector in W2R1 (irradiated to 1×10^{15} $n_{eq}\,cm^{-2}$) and the shape of the deep p-well cutout and collection electrodes. The cutout of the deep p-well influences the charge collection shape. The overlaid image is equivalent to four pixels of one double column. Figure from [57]

The improvements in response of the extra deep p-well and the gap in the n^- layer are clearly visible in the plots shown in Figure 5.5. There is a small improvement in the response of the non-irradiated samples, as can be observed in the top row of Figure 5.5. The inefficiency observed in the pixel with the continuous n^- layer is due to the same lack of electric field shown in section 4.3. In particular the slight corner inefficiency is not present in the mini-MALTA modified layouts. It is also important to note that most of the pixels remain fully responsive after irradiation due to the different electric field structure. The same improvement between designs is seen in the other two samples from the different wafers - W5R9 and W4R9.

5.3.4 Shape of the charge collection area

The shape of the continuous n^- layer in the mini-MALTA has a distinctive asymmetric shape, which is most visible in figure Figure 5.5g. There is also a pattern that repeats itself at every other pixel. This is because the chip is readout in double columns of 16 pixels (8×2). The pixels are mirrored on each side of the double column. The shape observed in Figure 5.5g and highlighted in Figure 5.6 is caused

by the shape of the p-well cutout. In the Investigator chip the p-well cutout is square and its size is defined by the spacing parameter. In the MALTA case, all the pixels are the same and have the same p-well cutout which is optimized to have larger area whilst maintaining the junction capacitance low. An overlay of the p-well cutout shape and a scan for the irradiated continuous n^- layer region is shown on Figure 5.6. The dark region is where there is only n^- layer except for the dot in the centre which is the collection electrode with n^{++} doping.

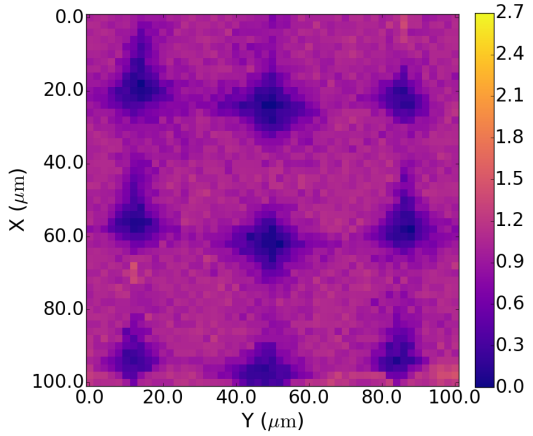
5.3.5 Pixel response as a function of external bias voltage

Due to the lack of different test pixels and dummy pixels as in the Investigator chip causing high leakage current, the MALTA chip allows for applying up to -20 V on the back substrate. The p-wells voltage can be set to a maximum of -6 V, since that voltage is dependent on the junction with the transistors inside the p-well. A measurement to evaluate the effect of different bias on the back of the substrate was performed on irradiated samples as the electric field changes are more visible in this case. Data was collected on each of the sectors with the W2R1 sample at -6 V and -20 V back bias. The results for the continuous n^- layer are shown in Figure 5.7. The pixel response decreases from 76.7% to 72.2% as the back substrate bias increases. The reason for that is that the pixel edges become less responsive. A similar effect is seen for the modified designs as shown in Figure 5.8. The numerical decrease for all three designs can be seen in Table 5.3.

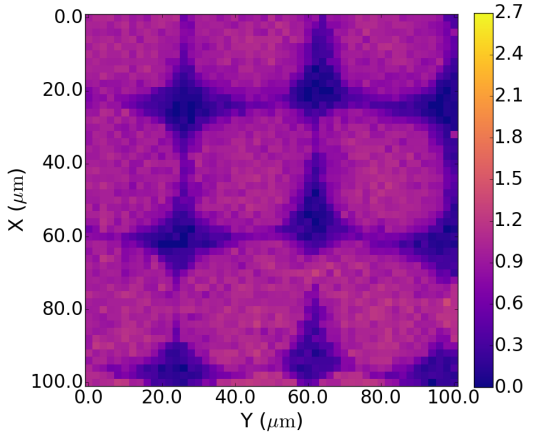
Sample	Bias (V)	continuous n^- response (%)	extra deep p-well response (%)	n^- gap response (%)
W2R1	-6	76.7 ± 3.8	91.1 ± 3.0	90.0 ± 3.1
W2R1	-20	72.2 ± 3.3	86.6 ± 3.9	86.4 ± 2.9

Table 5.3: Average normalised response at two bias voltages for the different sectors of the W2R1 sample irradiated to 1×15 n_{eq}/cm^2.

The reason for this effect is the lower lateral E-field at higher bias voltages. A TCAD simulation at bias voltages of -6, -15 and -20 V is shown in Figure 5.9. The p-well voltages are kept at -6 V. The higher potential difference, when the bias voltage reaches -20 V, creates a stronger electric field in the medial direction, but the similar potential creates a lower lateral electric field. This results in a faster drift

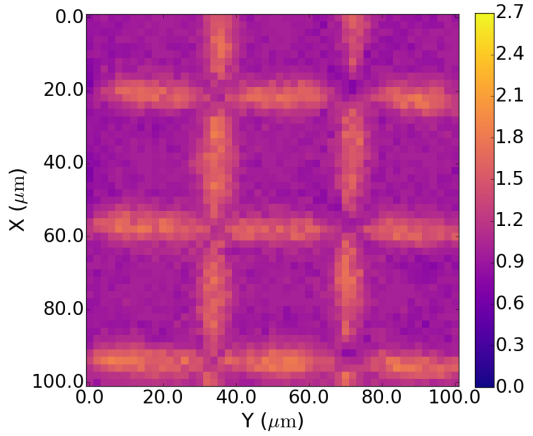


(a) Continuous n^- sector in W2R1 at -6 V biasing voltage.

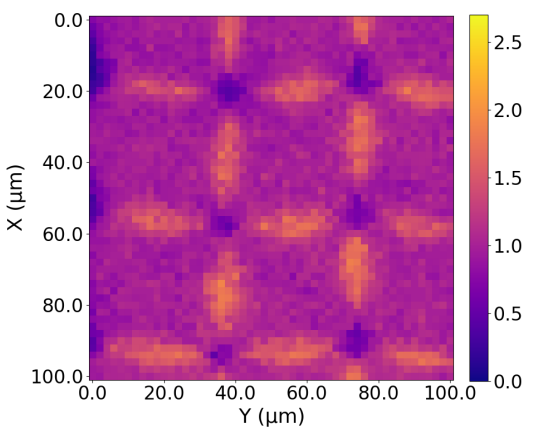


(b) Continuous n^- sector in W2R1 at -20 V biasing voltage.

Figure 5.7: Response maps for pixels with continuous n^- sector in the W2R1 sample irradiated to 1 $\times$ 15 n_{eq}/cm^2 at -6 V (a) and -20 V (b) biasing voltage.



(a) n^- gap sector in W2R1 at -6 V biasing voltage.



(b) n^- gap sector in W2R1 at -20 V biasing voltage.

Figure 5.8: Response maps for pixels with n^- gap in the W2R1 sample irradiated to 1 $\times$ 15 n_{eq}/cm^2 at -6 V (a) and -20 V (b) biasing voltage.

time of the charges from the back substrate to the top side, but a slower lateral drift speed from the p-well centre to the collection electrode. The effect is that the low electric field regions at the corners are amplified due to the symmetry at the edge of the pixel, resulting in larger inefficiency gaps. There is also the effect of charge

clouds created near the back of the substrate having less time to diffuse until they reach the top of the chip, resulting in a sharper boundary of the charge collection.

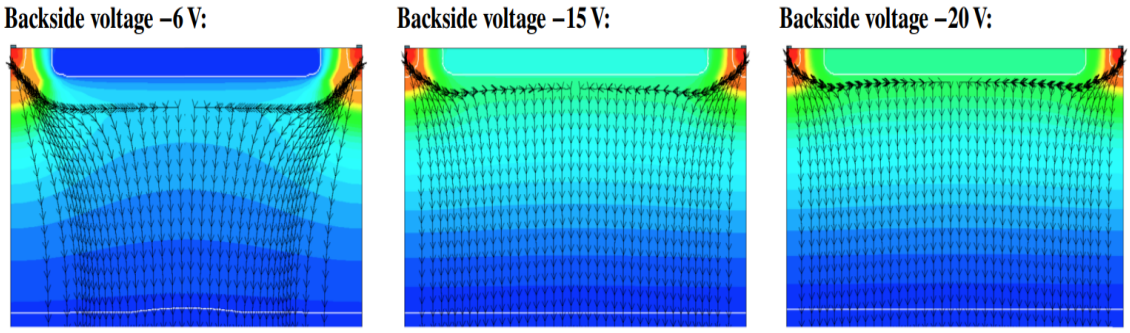


Figure 5.9: TCAD simulations of the continuous n^- layer for different backside external bias voltages applied. The colors represent the potentials and the lines represent the electric field. The simulation is centred on the pixel edge (middle of the p-well) and the collection electrodes are on the two sides. Figure adapted from [60].

In Figure 5.8 it can be seen that the modified regions experience a similar effect as the backside voltage increases. The external p-well implant is a few micrometer thick strip, laid out as a grid on top of the pixel matrix, coinciding with the edges of each pixel. The same pattern occurs for the n^- gap design. The corners of the pixels end up having a crossed (both in X and Y direction) pattern of the modification, which flattens out the region and reduces the potential gradient in that area. This introduces a lower electric field region in the corners, which can be seen in Figure 5.8b. Similarly to the continuous n^- layer, the higher voltage on the back of the substrate flattens out the lateral potential difference and amplifies the inefficiencies.

5.4 Charge Sharing

5.4.1 Analysis from pixel response maps

Charge sharing occurs when a photon hits the region between two or more pixels and a signal is collected by multiple pixels. This produces, on average, a photon response of $\sim$ 200 % at the pixel edge and even higher at the pixel corners. To quantify the amount of charge sharing, the pixel boundary (red square) shown in Figure 5.4a is used. In order to avoid biased results, only the pixels that are entirely within the scan

Sample	Fluence n_{eq}/cm^2	TID (Mrad)	continuous n^- charge sharing (%)	extra p-well charge sharing (%)	n^- gap charge sharing (%)
W2R11	0	0	15.8 ± 5.2	20.3 ± 4.6	16.9 ± 4.9
W2R9	5e14 (p)	66	7.7 ± 2.9	17.9 ± 5.4	21.2 ± 5.1
W2R1	1e15 (n)	0	7.1 ± 2.7	23.6 ± 6.9	21.3 ± 4.9
W5R9	5e14 (p)	70	7.3 ± 3.1	14.1 ± 3.8	15.4 ± 3.8
W4R9	7e13 (p)	9	8.4 ± 3.5	14.9 ± 4.3	15.7 ± 4.4

Table 5.4: Calculated charge sharing percentages for the different samples and designs.

range are considered. To quantify charge sharing we calculate the ratio between the photon response outside the red square and the total photon response. Additionally, the extent of the charge sharing region per pixel is estimated as a separate parameter. Its value is calculated by measuring the distance in micrometers from the edge of the red square to the furthest from that edge non-zero photon response value within the selected row or column. This is done for each side of the square and an average is given as the charge sharing extent of the pixel. For both ways of measuring charge sharing, the values obtained for the measured pixels are averaged to find the charge sharing of the sample. The uncertainty on that values is given by the standard deviation between the values obtained for the pixels.

The results for the charge sharing percentages and extents are summarised in Table 5.4 and Table 5.5 respectively. It can be seen that for all samples the charge sharing increases with the addition of the modifications, which is in good agreement with the pixel response maps shown in Figure 5.5. The fact that the edge regions are sensitive means that there is no low electric field region, confirming the effect of the modifications. No significant decrease in charge sharing can be calculated for the extra deep p-well region and the n^- gap region. The largest changes occur in the pixel corners. However, these regions are small and therefore they do not affect significantly the measurements. The charge sharing is an important parameter for the operation of the detector, as MIPs typically leave charge trails, which are shared between pixels. The passage of charged particles leads to a cluster of hit pixels allowing for better estimation of the particle track. The fact that charge sharing is not affected by the irradiation dose (up until the measurements) indicates that the

Sample	Fluence n_{eq}/cm^2	TID (Mrad)	continuous n^- charge sharing (μm)	extra p-well charge sharing (μm)	n^- gap charge sharing (μm)
W2R11	0	0	4.5 ± 1.5	5.4 ± 1.3	4.5 ± 1.3
W2R9	5e14 (p)	66	2.6 ± 1.8	5.4 ± 2.2	5.5 ± 2.0
W2R1	1e15 (n)	0	3.2 ± 2.0	6.1 ± 2.0	6.5 ± 2.6
W5R9	5e14 (p)	70	2.4 ± 2.0	4.5 ± 1.8	4.5 ± 2.7
W4R9	7e13 (p)	9	2.4 ± 1.9	4.1 ± 1.9	4.1 ± 1.0

Table 5.5: Extents of the charge sharing regions for different samples and pixel designs.

resolution of the devices will not change in the radiation environment where they are expected to operate.

5.4.2 Asymmetry of the pixels

Even though pixel response should be more uniform with the new modifications, there is still an asymmetry in the corners. The asymmetry is clearly seen in Figure 5.5b and Figure 5.5c. The cause of this effect is the double column structure and the asymmetry of the p-well cutout shown in Figure 5.6. Further contributions can also be due to differences in circuit lines in the centre and the perimeter of the double column.

To quantify the asymmetry, the photon response outside the red square in Figure 5.4a is extracted into a separate map. This is done for each pixel and the resulting plot is shown in Figure 5.10. The map only shows the charge sharing regions, which cause the asymmetry effect. The photon response is then summed for each of the pixel edge columns, shown as darker regions. The central column in Figure 5.10 has a higher response value than the other two, which suggest that it is a boundary between two double columns. The lower values would then be the central regions of the double column. The asymmetry value is calculated as the ratio of the double column periphery region to the double column centre region. The error is estimated by combining the variation of the values between the two different columns

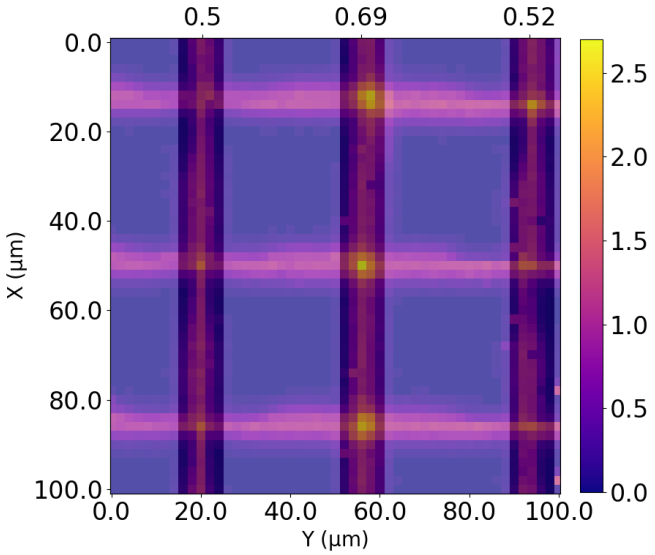


Figure 5.10: Illustration of the charge sharing asymmetry analysis. The response due to charge sharing is calculated in the grey columns and their ratio is defined as the charge sharing asymmetry.

(i.e. the two periphery or the two central regions depending on the scan range) and the normalisation error from the pixel response calculation used in Table 5.2. The results for the asymmetry are shown in Table 5.6. The asymmetry is smaller for the extra deep p-well and n^- gap designs in comparison to the continuous n^- layer design. This is because the electric field changes, due to the optimized p-well cutout shape, have less effect on the modified regions. There is a decrease in charge sharing asymmetry in the modified regions due to the less efficient corner regions caused by the crossing of the modification strips and the constant lateral potential.

5.4.3 Cluster sizes

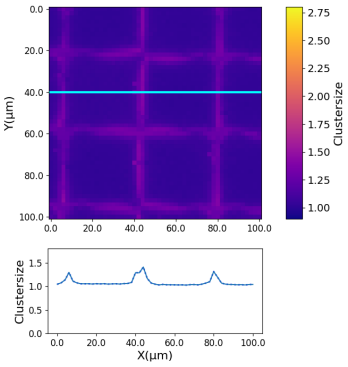
The photon response maps show the superposition of two different effects. The shape and depth of the sensitive region is one part of the information. This is linked to the charge loss in the corners in the continuous n^- layer design. There is also information about the charge that a single photon deposits, which can be split between different pixels. To separate the two effects a cluster size analysis per single hit is performed on the data.

The mini-MALTA chip is designed to record events synchronised with the LHC frequency of 40 MHz. This means that one event has a recording window of 25 ns. Each event is analysed separately and a cluster size value is extracted from

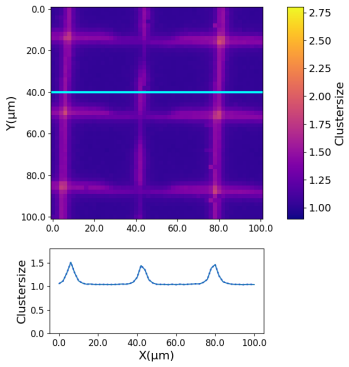
Sample	Fluence n_{eq}/cm^2	TID (Mrad)	continuous n^- asymmetry	extra deep p-well asymmetry	n^- gap asymmetry
W2R11	0	0	1.80 ± 0.11	1.49 ± 0.07	1.43 ± 0.07
W2R9	5e14 (p)	66	1.49 ± 0.12	1.11 ± 0.10	1.17 ± 0.09
W2R1	1e15 (n)		1.16 ± 0.10	1.07 ± 0.06	1.15 ± 0.09
W5R9	5e14 (p)	70	1.39 ± 0.09	1.02 ± 0.06	1.12 ± 0.07
W4R9	7e13 (p)	9	1.22 ± 0.08	1.02 ± 0.05	1.09 ± 0.07

Table 5.6: Charge sharing asymmetries for the different samples and designs.

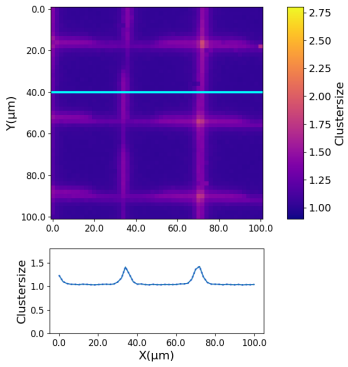
it. Averaging all the cluster sizes for one beam position, gives a number that can be shown on the 2D raster scan map. Events with hits outside the beam position are either due to noise or are coming from the beam halo and are discarded. The results of the average cluster size are plotted on the same scan windows as the pixel response maps in Figure 5.11. The bottom panel shows a one dimensional profile of the average cluster at the position of the blue line. There are no regions with value less than 1 cluster as this is the minimum cluster size and as expected the central regions have an average cluster size of 1. For the extra deep p-well and the n^- gap sectors the resulting cluster maps look very similar to the pixel response maps, as the latter are dominated by charge sharing for these designs. The corners in the periphery of the double column are similar to the photon response maps. In these regions the charge may split into four pixels, however there are very few such hits. This is because of the threshold of the device used for data taking. A signal of $\sim 2000e^-$, as expected from the 8 keV X-ray, needs to be fully collected and split equally between the pixels in order to be detected with the used threshold of ~ 400. Thus the probability of detecting a charge split into four pixels is low. Nevertheless, the effect irradiation has on the pixel corners in the clustering analysis is identical to the one seen in the pixel response maps in Figure 5.5. For the continuous n^- sector, average cluster sizes above 1 are also observed at the pixel edges, though the values are lower compared to the extra deep p-well and n^- gap sector. This is because the inefficiency region leaves an effectively thinner sensitive area, which reduces the average cluster size. However, this analysis shows that there is also charge sharing present in the continuous n^- sector.



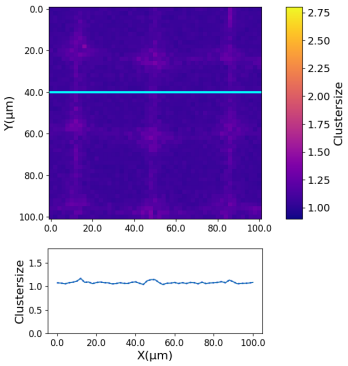
(a) W2R11 continuous n^- layer, non-irradiated



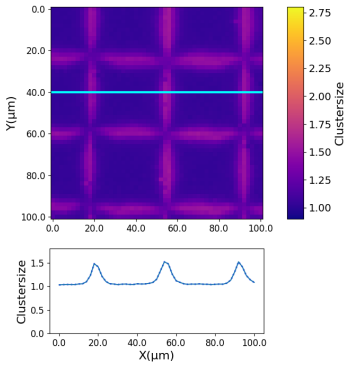
(b) W2R11 extra deep p-well, non-irradiated



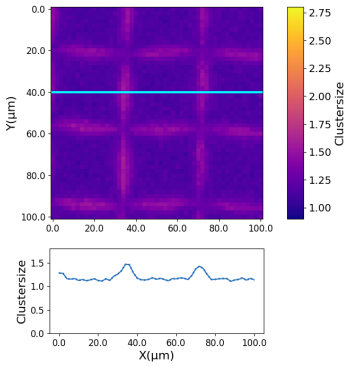
(c) W2R11 n^- gap, non-irradiated



(d) W2R1 continuous n^-, 1×10^{15} n_{eq}/cm^2



(e) W2R1 extra deep p-well, 1×10^{15} n_{eq}/cm^2

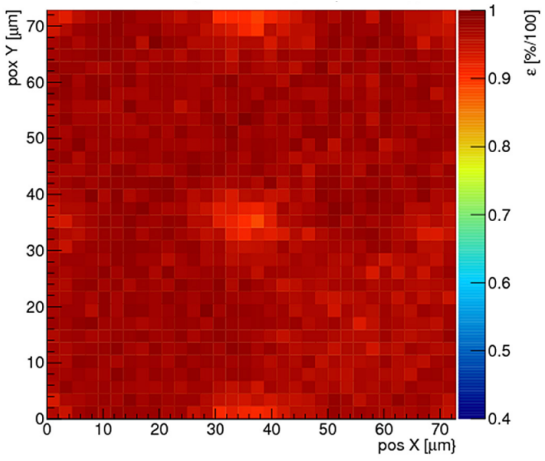


(f) W2R1 n^- gap, 1×10^{15} n_{eq}/cm^2

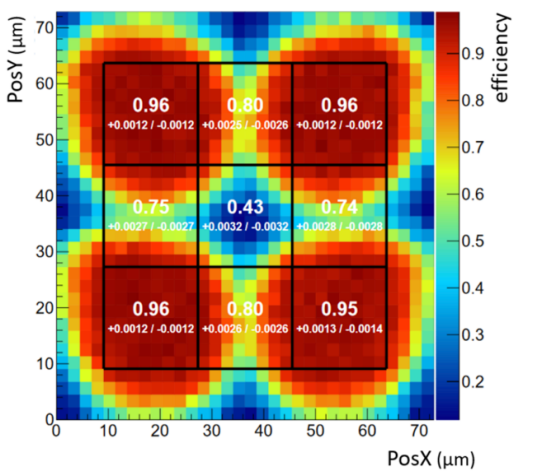
Figure 5.11: Map of cluster sizes for the different sectors in the W2R11 (unirradiated) and W2R1 (neutron-irradiated to 1e15 n_{eq}/cm^2) sample. The bottom panel shows the profile of cluster size for a particular x location, which is indicated by a blue line.

5.5 MIP efficiencies from X-ray data

Most test-beams test pixel detectors using minimum ionising particles, such as protons or electrons, since the devices have to be able to detect these particles well in experiments like ATLAS. Thus it is interesting to compare the results obtained from such test-beams to the results obtained at Diamond. The original MALTA chip was tested in a proton test-beam at SPS [44]. The obtained efficiency maps are shown in Figure 5.12. For better comparison, the data from the pixel response maps in Figures 5.5a and 5.5g is extracted and presented in Figure 5.13. All the results and figures in this section have been published in a separate paper [55].

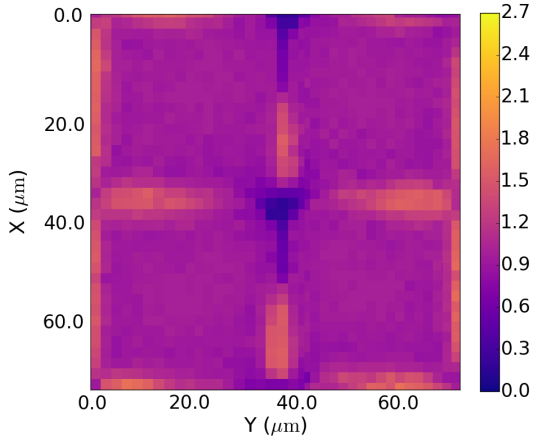


(a) Map for the non-irradiated sample with a threshold of 250 e (average efficiency 96%).

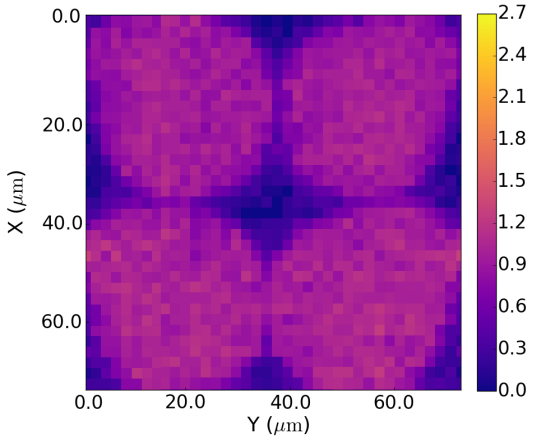


(b) Map for the device irradiated to 1 × 10^{15} n_{eq}/cm^2 with a threshold of 450 e (avg. eff. 72%).

Figure 5.12: Efficiency maps for the MALTA chip measured at a test-beam at SPS. Figures from [81].



(a) Map for the non-irradiated device.



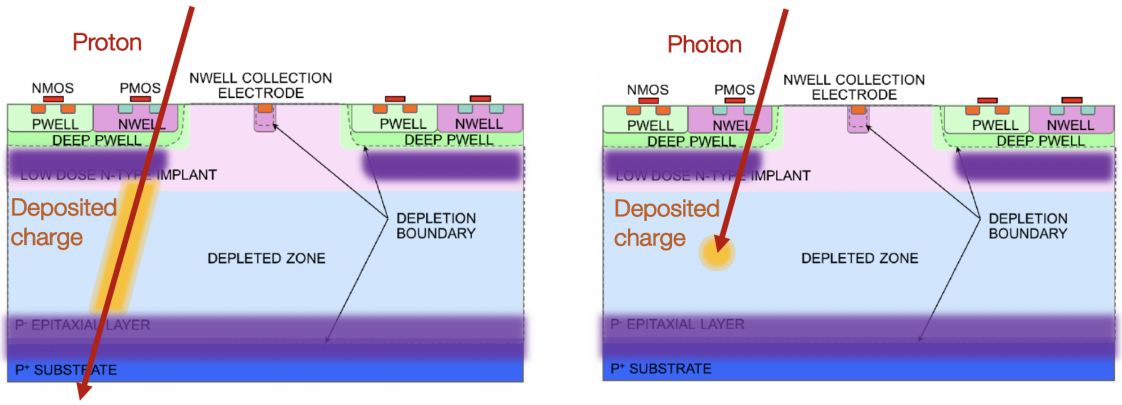
(b) Map for the device irradiated to 1 × 10^{15} n_{eq}/cm^2.

Figure 5.13: Pixel response maps for the continuous n^- sector of mini-MALTA measured at Diamond.

The pixel shape is visible in both figures, but there are major differences, as the efficiency and response maps are sensitive to different effects. Most notably, in the non-irradiated sample the pixel response in the corners decreases to around 20%. In the SPS data, the efficiency in the corners decreases only to around 90%. This is due

to the difference in energy deposition for the different kinds of particles. Protons leave a track of electron-hole pairs along their path, while photons stop and create a charge cloud as illustrated in Figure 5.14 and explained in more detail in chapter 2. Since mini-MALTA is designed to only count hits, without giving an indication of the energy deposited, the effect of the sensitive region depth and shape is more visible for photons. This is because the probability for detecting a photon depends on the sensitive region depth, whereas a MIP would still deposit charge in any kind of sensitive region and, due to the low pixel thresholds, this would be counted as a hit.

Figures 5.5a and 5.5g show a map of charge sharing and depletion depth. The same map for just a single pixel then corresponds to a map of relative sensitive region depth. It is possible to extrapolate the behavior of mini-MALTA in a MIP test-beam by knowing the relative sensitive region depth and by performing some additional measurements with radioactive sources. The methodology and results of this analysis are described in the following subsections.



(a) Schematic of energy deposition of protons.

(b) Schematic of energy deposition of photons.

Figure 5.14: Energy deposition of photons and protons. The purple regions show where the detector is likely to not be fully sensitive.

5.5.1 Methodology

To convert the sensitive region depth map into MIP efficiency, one has to determine if a MIP signal would be large enough to be seen, at each location in the pixel. First, this means understanding the size and shape of the signal at full depletion depth. This can be achieved by measuring the analog signal distribution of a β source,

such as ^{90}Sr, which is expected to show a Landau distribution. Using a γ source, such as ^{55}Fe a point on the gain curve for the device can be obtained. Assuming that the gain curve is linear, as the one measured for the Investigator sample in subsection 3.2.2, the analog signal spectrum in volts can be converted into electrons (e^-). The Landau distribution in terms of electrons can be scaled by the relative sensitive region depth at each location in the device, which is determined by the single pixel response map. This is shown schematically in the left side of Figure 5.15. The pixel threshold determines whether a signal is registered as a hit so the fraction of the scaled Landau distribution, which is above the pixel threshold is calculated and defined as the MIP efficiency at this position. This is illustrated on the right-hand side of Figure 5.15. This procedure is repeated for each pixel and each position of the beam, and a map of the MIP efficiencies at each position is obtained. The conversion is done for each pixel individually, but the map is normalised to the global maximum of hits in the normalisation areas. This process provides results that can be compared with a charged particle test-beam, where the efficiency is calculated with respect to a reference device and using a test-beam telescope setup, so pixel to pixel variations are visible. Finally, a Gaussian filter with a standard deviation of 3 μm is applied to the resulting map from the X-ray test-beam to mimic the resolution expected in a proton test-beam due to the telescope resolution [81].

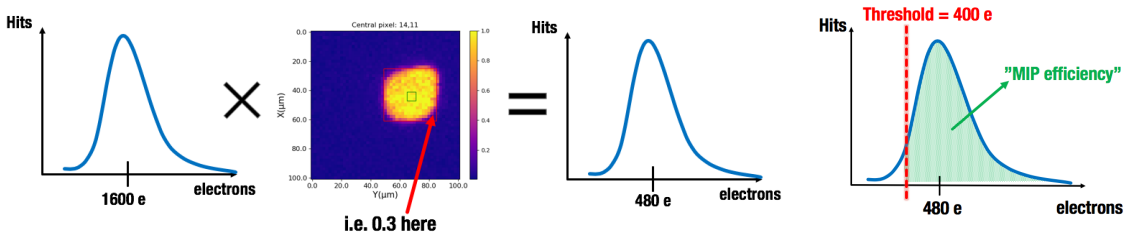
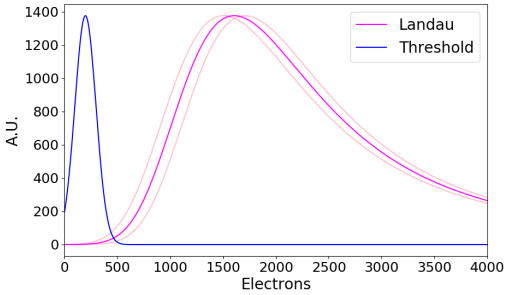
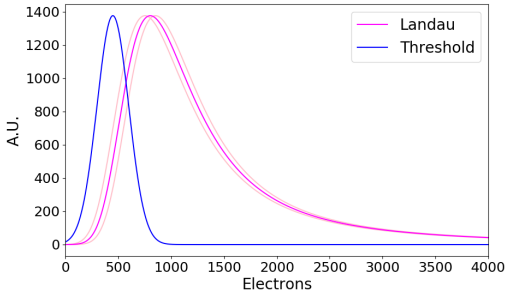


Figure 5.15: Illustration of the MIP analysis technique. (Left) Scaling of the Landau distribution by the relative depletion depth. (Right) Determination of MIP efficiency as the fraction of the Landau distribution above threshold.

The numerical value for the MIP efficiency is determined for each fully visible pixel in the scan. The error on this MIP efficiency is determined from three different sources: the normalisation uncertainty, the determination of the Landau distribution and the pixel threshold. The normalisation uncertainty is determined from the variation of the number of hits in the previously mentioned normalisation square of the single pixel photon response maps (Fig 5.4a) and then propagated through the MIP efficiency calculation. The Landau distribution has an uncertainty which is determined in the fit of the distribution obtained with ^{90}Sr data. This error is then propagated using a Monte Carlo approach by considering the minimum and



(a) Threshold distribution assuming a mean value of 200 e^- in blue. Signal distribution modelled with a Landau function assuming full depletion is shown.



(b) Threshold distribution assuming a mean value of 450 e^- in blue. Signal distribution modelled with a Landau function assuming full depletion is shown.

Figure 5.16: Illustration of the MIP efficiency analysis for data with low pixel threshold and large depletion depth as in the non-irradiated case (a) and high pixel threshold and small depletion depth as in the irradiated case(b). For the error analysis the width of the threshold distribution (blue) and the error on fitting the Landau distribution (pink) were considered.

maximum of the fit parameters and determining how much the MIP efficiency value would change due to these variations. The pixel threshold has an uncertainty due to intrinsic noise and pixel to pixel threshold variation. The value of this error can be determined by measuring the threshold distribution in mini-MALTA. The influence of this error on the MIP efficiency is then determined in the same manner as for the error on the Landau distribution. The effects of the threshold and Landau uncertainties are illustrated in Figure 5.16, which shows the threshold and the signal distribution, which are modelled as a Gaussian and a Landau function respectively. The left-hand side of Figure 5.16 shows the expected distribution in the pixel centre of an non-irradiated sample. The threshold is fairly low and the sensor is fully depleted. Varying the two distributions does not have a large effect on the area of the Landau distribution that is above the threshold. The right-hand side shows the expected distributions for an irradiated sample and away from the pixel centre. The pixel threshold is quite high and the smaller depletion depth means that the Landau distribution is scaled to a smaller signal height. In this case the variation on the threshold has have a significant effect on the value of the MIP efficiency. Thus the errors on the MIP efficiencies of the irradiated samples are expected to be larger than those of an non-irradiated sample.

5.5.2 Source measurements

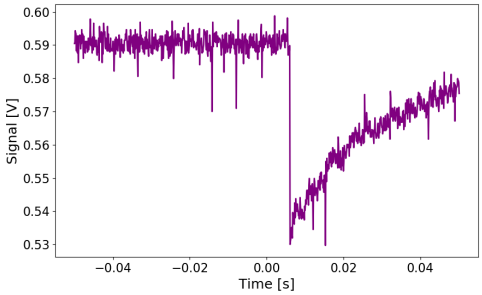
Mini-MALTA has 16 monitoring pixels, 8 on either side of the pixel matrix, which can be used for analog measurements. Different pixels can be used to access either the input or output node of the front-end, i.e. before or after amplification. The pixels also have different layouts: the area, which is normally used for digital readout, is either filled with highly p-doped active area or with n-wells to emulate the n-wells of the digital circuitry. Half of the monitoring pixels have the standard transistors, and half have the enlarged transistors that were implemented to reduce noise.

For the source measurements, a pixel with standard transistors was chosen, which corresponds to the MALTA chip tested at SPS and the continuous n^- layer sector of mini-MALTA that was tested at Diamond. The pixel also had the n-type implants in the empty area, which represents the actual design of the digital circuitry better. Finally, a pixel with signal before amplification was chosen, as this would produce distribution of the signal without any artifact features from the pulse-shaping circuit.

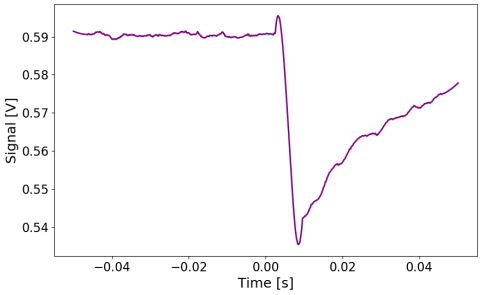
The pixel was read out with an oscilloscope. A voltage of $-2\,V$ on the p-well and $-6\,V$ on the back of the substrate was applied to the devices, as it was done in the SPS test-beam. The signal before amplification is $\sim 20\,mV$, which is smaller than the ones measured in chapter 3 due to the lower p-well voltage. This made it difficult to identify it with a basic pulseheight trigger on the oscilloscope. Instead, the scope traces were continuously recorded and then identified as signal using a software trigger. An example of a signal is shown on the left in Figure 5.17. The software trigger applied is a Savitzky-Golay[53] filter to the waveform to reduce the noise. The signal after the noise filter is shown in Figure 5.17 and was selected through the change in pulseheight and width.

The results of the source measurements are shown in Figure 5.18. The ^{55}Fe spectrum shows the expected Gaussian peaks and a flatter region due to charge sharing before them. Fe-55 is expected to deposit $\sim 1620\,e^-$ electrons, which provides a point on the gain curve for the device. The other known point is the origin. Knowing that the non-irradiated Investigator devices have a linear gain curve, a gain curve for the mini-MALTA is drawn using those two points.

The ^{90}Sr measurement shows the expected Landau distribution. The peak is located at 1540 electrons. Assuming that a MIP deposits 76 e/μm [32], this results in a depletion depth of $\sim$ 20 μm in the pixel centre. The slightly lower depth is explained by the lower p-well voltage than the setup used in chapter 3 and chapter 4.

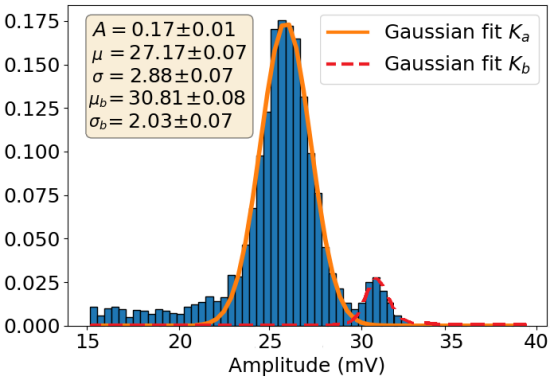


(a) Raw signal trace.

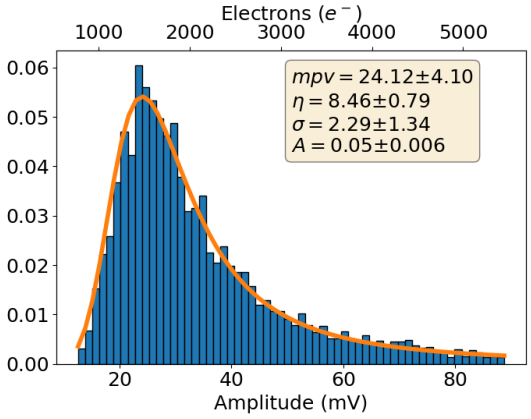


(b) Signal trace after applying the noise filter.

Figure 5.17: Example of a raw trace recorded in the ^{90}Sr measurement shown in (a) and the same trace with a Savitzky-Golay filter applied to it shown in (b).



(a) ^{55}Fe spectrum



(b) ^{90}Sr spectrum

Figure 5.18: Source measurements on one of the analog pixels of mini-MALTA before amplification with the fit parameters of the Gaussian and Landau functions (in mV).

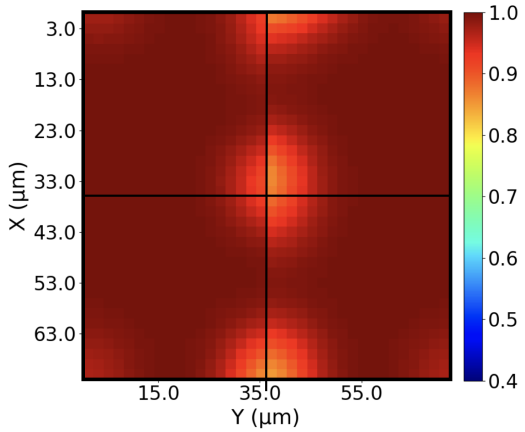
The results of the fit of the Landau distribution are then used to calculate the MIP efficiency.

5.5.3 Results

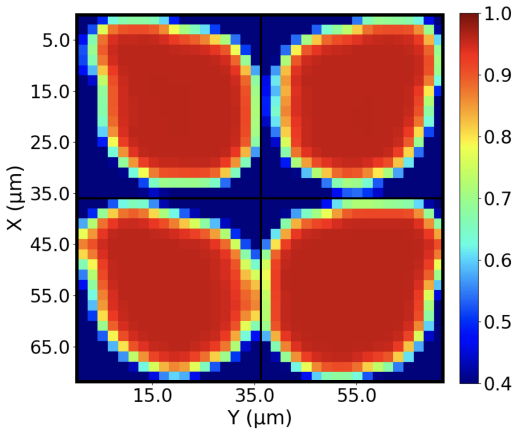
The above calculations were performed for the continuous n^- layer, extra deep p-well and n-gap sectors of a non-irradiated and a mini-MALTA sample irradiated to 1×15 n_{eq}/cm^2. First, the continuous n^- layer design was compared to the MALTA chip, which was measured in a test-beam campaign at SPS [81]. The thresholds used in the charged particle analysis were chosen in agreement with what was used at the test-beam. The extrapolated efficiency maps found with this technique are shown in

Figure 5.19, and the efficiency values are summarised in Table 5.7. The results shown in the figure and the table show the same behaviour as the efficiency maps presented in Figure 5.12. Inefficiencies in pixel corners can be seen even for the non-irradiated design in agreement with the finding presented in chapter 4. The asymmetric charge collection shape is also clearly visible for the irradiated MALTA device. There is slightly smaller asymmetry than in the mini-MALTA, due to the smaller asymmetric extension of the p-well cutout in the MALTA chip. The efficiency values agree very well, and show the expected trends with irradiation and changes in threshold.

The same approach was used to compare the data taken at Diamond with the data taken for the mini-MALTA chip at a test-beam at ELSA. This has the advantage that the same devices were tested. Removing systematic effects due to differences between the samples. The extrapolated efficiencies for a non-irradiated and an irradiated device are summarised in Tables 5.8 and 5.9. The two new modified designs in mini-MALTA were studied, assuming that the ^{90}Sr spectrum should be similar, since the bulk of the substrate and the electric field in the central region of the pixel is identical. The numerical values of the efficiencies are in very good agreement and show similar trends with irradiation. Concerning the efficiency maps, the results from ELSA and Diamond are compared in Figure 5.20. Due to the fact that ELSA uses a lower energy electron beam, the spatial resolution is significantly worse compared to SPS ($\sim$ 13.5μm [34]), as can be seen in Figure 5.20 (a). By applying a Gaussian filter, it is possible to simulate this resolution for the Diamond data. The simulated results are shown in Figure 5.20 (b), which agrees very well with the ELSA results. Using the full available position resolution of the Diamond test-beam, shown in Figure 5.20 (c), the pixel shape is clearly visible again. Of particular interest is the performance of the two new mini-MALTA modified designs. Both designs are fully efficient before irradiation and experience only a small loss in efficiency after irradiation. The extrapolated efficiency maps after irradiation are shown in Figure 5.21. Using the improved spatial resolution provided by Diamond, it can be inferred that the loss in efficiency is due to charge loss in the pixel corners.

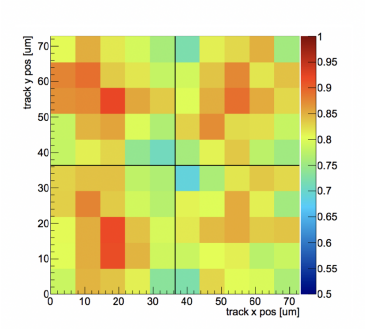


(a) MIP efficiency map for an non-irradiated sample with a threshold of 250 e^-.

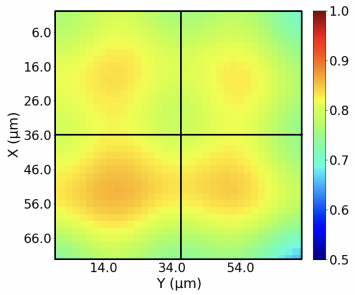


(b) MIP efficiency map for an irradiated (1×15 n_{eq}/cm^2) sample with a threshold of 450 e^-.

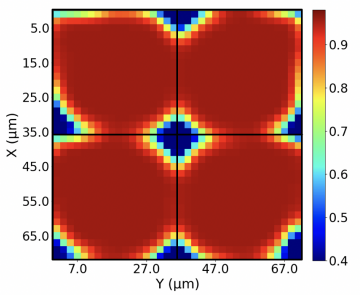
Figure 5.19: MIP efficiency maps for the MALTA equivalent sector of mini-MALTA before (a) and after (b) irradiation.



(a) In-pixel efficiency map measured at ELSA.



(b) Extrapolated charged particle efficiency map, assuming the resolution of the ELSA test-beam.



(c) Extrapolated charged particle with the true resolution of the Diamond test-beam.

Figure 5.20: Efficiency measured at ELSA and extrapolated from the Diamond test-beam on the continuous n^- sector of mini-MALTA. In (a) the efficiency map from the reconstructed ELSA test-beam data is shown (Figure from [34]). In the other two plots the data is from the X-ray test-beam at Diamond light source. In (b) the data is plotted with a simulated resolution equivalent to the ELSA test-beam and (c) shows the natural Diamond test-beam resolution.

Sample	non-irradiated (250 e^-)	irradiated (1e15 n_{eq}/cm^2, 350 e^-)	irradiated (1e15 n_{eq}/cm^2, 450 e^-)
MALTA at SPS	96%	74%	72%
mini-MALTA at Diamond	$(97.9^{+0.5}_{-1.6})$ %	$(76.4^{+2.8}_{-5.2})$%	$(73.0^{+4.1}_{-9.3})$ %

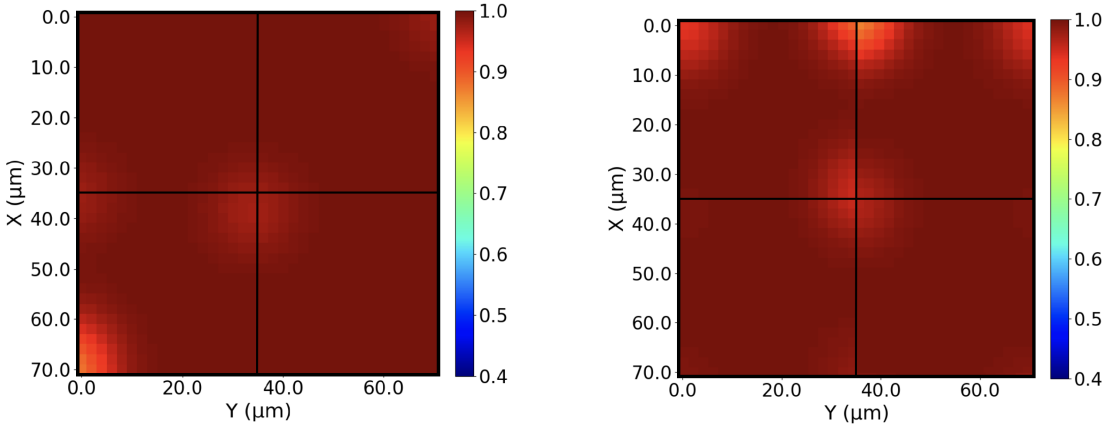
Table 5.7: Measured efficiencies at SPS [81] for the MATLA chip and extrapolated charged particle efficiencies on the continuous n^- sector of mini-MALTA for different thresholds and levels of irradiation. Both measurements were taken at a substrate voltage of -20 V.

Sample: W2R11 non-irradiated	continuous n^--layer (380 e^-)	p-well (200 e^-)	n^--gap (200 e^-)
ELSA efficiency	(97.9 ± 0.1) %	(99.6 ± 0.1) %	(99.6 ± 0.1) %
Diamond efficiency	$(97.7^{+1.8}_{-3.9})$ %	$(99.97^{+0.02}_{-1.6})$ %	$(99.89^{+0.04}_{-1.7})$ %

Table 5.8: Measured efficiencies at ELSA [34] and extrapolated charged particle efficiencies for the different mini-MALTA sectors on an non-irradiated sample. Both measurements were taken at a substrate voltage of -6 V.

Sample: W2R1 irradiated n_{eq}/cm^2	continuous n^--layer (210 e^-)	p-well (105 e^-)	n^--gap (105 e^-)
ELSA efficiency	(78.8 ± 0.2) %	(97.9 ± 0.1)%	(97.6 ± 0.1) %
Diamond efficiency	$(81.1^{+3.1}_{-6.2})$ %	$(97.6^{+0.4}_{-1.7})$%	$(97.8^{+0.3}_{-2.3})$%

Table 5.9: Measured efficiencies at ELSA [34] and extrapolated charged particle efficiencies for the different mini-MALTA sectors on an irradiated (1e15 n/cm^2) sample. Both measurements were taken at a substrate voltage of -6 V.



(a) MIP efficiency map for the additional p-well design.

(b) MIP efficiency map for the n^- gap design.

Figure 5.21: MIP efficiency maps for the new mini-MALTA designs on the irradiated sample (1×15 n_{eq}/cm^2). For both sectors a threshold of 200 e^- was set.

5.6 Summary

In chapter 4, as well as in previous test-beams [44], it has been shown that the initial design of the chip has inefficiencies in the pixel corners when it is irradiated. A new design of the chip has been produced with modifications designed to reduce those inefficiencies. This chapter evaluates the performance of the new chip and the effect of the modifications in an X-ray test-beam. This is a novel approach and is different from the conventional charged particle test-beam, which was also performed in parallel. The results of the X-ray test-beam are presented with their benefits and drawbacks. Additionally, an extrapolation technique is developed to better compare the results from the X-ray test-beam with the charged particle test-beam. As the necessary condition for ATLAS is that the efficiency $> 98.5\%$ before irradiated and $> 97\%$ after [89], it is concluded that the additional modifications reduce the inefficiencies of the device, thus maintaining sufficient efficiency up to the measured radiation dose.

Chapter 6

Conclusions

The ATLAS Experiment at the LHC has played a major role in the discovery of the Higgs boson. The ATLAS detector components closer to the beamline are the silicon vertex detector and tracker. This means that they receive the highest radiation fluence. Thus radiation hardness is one of the requirements for these silicon pixel layers. Current pixel detectors are made of two parts: sensors where electron-hole pairs are created by charged particles and chip that processes the generated signal. The two elements are connected by a complex bump bonding process. Monolithic sensors avoid this process and allow for cheaper and more easily produced parts. Additionally, this reduces the material budget of the detector. There are two main techniques to create a monolithic active pixel sensor, based on HVCMOS and HRCMOS processes. This thesis is focused on the high-resistivity CMOS approach (HRCMOS). In particular, the thesis reports studies on the radiation damage of several CMOS detectors fabricated with the 180nm TowerJazz process.

Radiation damage to the silicon bulk changes the effective doping of the substrate. A direct quantification of the effective doping is the charge collection capacitance of a single pixel. This was measured for both an irradiated and non-irradiated sample called Investigator2. The values found before and after irradiation agreed within error and the discrepancies are small enough to be attributed to variations between samples. It was also shown that due to the larger leakage current one of the pixel reset designs is superior.

The depletion region size is also affected by radiation damage. Images of the depletion depth relative to the chip surface were produced using an edge transient-current technique on the same Investigator2 samples. Using the data from the

capacitance measurements, the depletion region maps were converted to comparable units of e^-. No significant degradation of the depletion depth was found when the device is irradiated. The main source of the difference between the irradiated and non-irradiated device is caused by low electric field regions in the corners of the pixel as simulated using TCAD. Radiation damage amplifies the inefficiencies caused by these regions.

Two modifications to fix the corner inefficiencies were proposed. A new chip called mini-MALTA, which included old pixel designs and two designs with a modification, was produced. Multiple samples (irradiated and non-irradiated) of that chip were tested in a high resolution X-ray test-beam. The outcome of the test-beam confirmed the improved performance of the two modified designs. The detector is designed for massive particles with properties similar to minimum ionisation particles (MIPs). With additional laboratory measurements an extrapolated efficiency for MIPs is estimated, which was then compared to published data from proton and electron test-beams.

Outlook

The modified TowerJazz designs were found to tolerate a radiation equivalent dose to the outermost pixel layer in ATLAS ITk. The next step would be to increase the radiation tolerance sufficient for the inner two layers. This would allow to use monolithic devices in the layers that will be replaced halfway through HL-LHC. The effect would be a significant reduction in the material of the detector allowing for better position resolution.

The monolithic technology is gaining popularity and being used in experiments such as STAR [31] and ALICE [75] and being developed for many others. The similarity between different chip architectures allows for transfer of developmental work as well. The radiation hardness of DMAPS along with the low material are important requirements for $e^+ e^-$ colliders such as CLIC[74], ILC[95], FCC-ee[48], CEPC[40]. The chips developed with the TowerJazz technology are a great candidate for these future projects.

Bibliography

[1] G. Aad et al. ATLAS pixel detector electronics and sensors. *JINST*, 3:P07007, 2008.

[2] G. Aad et al. The ATLAS Experiment at the CERN Large Hadron Collider. *JINST*, 3:S08003, 2008.

[3] Georges Aad et al. Operation and performance of the ATLAS semiconductor tracker. *JINST*, 9:P08009, 2014.

[4] T. Aaltonen et al. Operational Experience, Improvements, and Performance of the CDF Run II Silicon Vertex Detector. *Nucl. Instrum. Meth.*, A729:153–181, 2013.

[5] G. Anelli, M. Campbell, M. Delmastro, F. Faccio, S. Florian, A. Giraldo, E. Heijne, P. Jarron, K. Kloukinas, A. Marchioro, P. Moreira, and W. Snoeys. Radiation tolérant VLSI circuits in standard deep submicron CMOS technologies for the LHC experiments: Practical design aspects. *IEEE Transactions on Nuclear Science*, 46(6 PART 1):1690–1696, 1999.

[6] G Apollinari, I Béjar Alonso, O Brüning, M Lamont, and L Rossi. High-Luminosity Large Hadron Collider (HL-LHC) : Preliminary Design Report. 2015.

[7] V. Arosio, M. Caccia, V. Chmill, A. Ebolese, M. Locatelli, A. Martemiyanov, C. Mattone, R. Santoro, and C. Tintori. Reconstruction of the statistics of photons by a pulsed LED using a silicon photomultiplier based set-up. *Journal of Instrumentation*, 10(08):C08008–C08008, aug 2015.

[8] ATLAS and CMS Collaborations. Measurements of the higgs boson production and decay rates and constraints on its couplings from a combined atlas and cms analysis of the lhc pp collision data at $\sqrt{s} = 7$ and 8 tev. 2016.

[9] G Audi, O Bersillon, J Blachot, and A H Wapstra. The NUBASE evaluation of nuclear and decay properties *. 2003.

[10] H. Augustin et al. Mupix8 — large area monolithic hvcmos pixel detector for the mu3e experiment. *Nuclear Instruments and Methods in Physics Research Section A: Accelerators, Spectrometers, Detectors and Associated Equipment*, 936:681 – 683, 2019. Frontier Detectors for Frontier Physics: 14th Pisa Meeting on Advanced Detectors.

[11] Giancarlo Barbarino, Riccardo de Asmundis, Gianfranca De Rosa, Carlos Maximiliano Mollo, Stefano Russo, and Daniele Vivolo. Silicon Photo Multipliers Detectors Operating in Geiger Regime: an Unlimited Device for Future Applications. In Jeong-Woo Park, editor, *Photodiodes*, chapter 9. IntechOpen, Rijeka, 2011.

[12] R.S. Barnes and M.J. Makin. On the mechanism of irradiation annealing. *Journal of Nuclear Energy (1954)*, 2(3-4):291–298, jan 1956.

[13] K.H. Becks et al. The delphi pixels. *Nuclear Instruments and Methods in Physics Research Section A: Accelerators, Spectrometers, Detectors and Associated Equipment*, 386(1):11 – 17, 1997. Proceedings of the 5th International Workshop on Vertex Detectors.

[14] Gautam Bhattacharyya. The hierarchy problem and physics beyond the standard model. In Md. Naimuddin, editor, *XXII DAE High Energy Physics Symposium*, pages 17–20, Cham, 2018. Springer International Publishing.

[15] The university of birmingham cyclotron. *Nature*, 169(4299):476–477, March 1952.

[16] D. Bortoletto. How and why silicon sensors are becoming more and more intelligent? *Journal of Instrumentation*, 10(08):C08016–C08016, aug 2015.

[17] M. Boscardin, R. Ceccarelli, et al. Performance of new radiation-tolerant thin planar and 3d columnar n+ on p silicon pixel sensors up to a maximum fluence of 5×10e15 neq/cm2. *Nuclear Instruments and Methods in Physics Research Section A: Accelerators, Spectrometers, Detectors and Associated Equipment*, 953:163222, 2020.

[18] J Bronuzzi, A Mapelli, J M Sallese, and M Moll. Principle and modelling of Transient Current Technique for interface traps characterization in monolithic pixel detectors obtained by CMOS-compatible wafer bonding Related content

Analytical model for Transient Current Technique (TCT) signal prediction an. 2016.

[19] Oliver S. Bruning, P. Collier, P. Lebrun, S. Myers, R. Ostojic, J. Poole, and P. Proudlock. LHC Design Report Vol.1: The LHC Main Ring. 2004.

[20] MD Buckland. Simulation and evaluation of hv-cmos pixel sensors for the clic vertex detector. 2018.

[21] I. Caicedo, M. Barbero, et al. The monopix chips: depleted monolithic active pixel sensors with a column-drain read-out architecture for the ATLAS inner tracker upgrade. *Journal of Instrumentation*, 14(06):C06006–C06006, jun 2019.

[22] Ivan Caicedo, Marlon Barbero, et al. The monopix chips: Depleted monolithic active pixel sensors with a column-drain read-out architecture for the atlas inner tracker upgrade. 2019.

[23] M Capeans, G Darbo, K Einsweiller, M Elsing, T Flick, M Garcia-Sciveres, C Gemme, H Pernegger, O Rohne, and R Vuillermet. ATLAS Insertable B-Layer Technical Design Report. Technical Report CERN-LHCC-2010-013. ATLAS-TDR-19, Sep 2010.

[24] R. Cardella, I .Asensi Tortajada, I. Berdalovic, C. Bespin, F. Dachs, V. Dao, L. Flores Sanz de Acedo, F. Piro, T. Hemperek, T. Hirono, B. Hiti, T. Kugathasan, C.A. Marin Tobon, K. Moustakas, H. Pernegger, P. Riedler, E. J. Schioppa, A. Sharma, L. Simon Argemi, W. Snoeys, C. Solans Sanchez, T. Wang, and N. Wermes. MALTA: an asynchronous readout CMOS monolithic pixel detector for the ATLAS high-luminosity upgrade. *Journal of Instrumentation*, 14(06):C06019–C06019, jun 2019.

[25] F Carrió, V Castillo, A Ferrer, L Fiorini, Y Hernández, E Higón, B Mellado, L March, P Moreno, R Reed, C Solans, A Valero, and J A Valls. The sROD module for the ATLAS tile calorimeter phase-II upgrade demonstrator. *Journal of Instrumentation*, 9(02):C02019–C02019, feb 2014.

[26] Francesca Cenna. *Signal Formation in Innovative Silicon Detectors*. PhD thesis, University of Turin, 2014.

[27] Shuo Chen. *A Study on Properties of Novel Metallic Foam for Nuclear Applications*. PhD thesis, 08 2015.

[28] ATLAS Collaboration. Technical Design Report for the ATLAS Inner Tracker Pixel Detector. Technical Report CERN-LHCC-2017-021. ATLAS-TDR-030, CERN, Geneva, Sep 2017.

[29] ATLAS Collaboration. Operational Experience and Performance with the ATLAS Pixel detector at the Large Hadron Collider at CERN. Jun 2021.

[30] Common drain article, wikipedia. `https://en.wikipedia.org/wiki/Common_drain`. Accessed: 2020-01-24.

[31] Giacomo Contin, Leo Greiner, et al. The star maps-based pixel detector. 2017.

[32] Cinzia Da Vià, Gian-Franco Dalla Betta, and Sherwood Parker. Radiation Sensors with Three-Dimensional Electrodes. In *Radiation Sensors with Three-Dimensional Electrodes*, chapter 3, page 240. Boca Raton : CRC Press, 1st edition, 2019.

[33] P. Delpierre. Pixels detectors and silicon X-rays detectors. In *European Symposium on Frontiers in Science and Technology with Synchroton Radiation*, volume 04, pages C9–11–C9–18, Aix-En-Provence, France, 1994. EDP Sciences.

[34] M. Dyndal et al. Mini-MALTA: Radiation hard pixel designs for small-electrode monolithic CMOS sensors for the High Luminosity LHC. *Submitted to JINST*, 2019.

[35] A. C. Thompson et al. X-ray Data Booklet. In *X-ray Data Booklet*. 1st edition, 2001.

[36] J. Fang, M. Reaz, S. L. Weeden-Wright, R. D. Schrimpf, R. A. Reed, R. A. Weller, M. V. Fischetti, and S. T. Pantelides. Understanding the average electron–hole pair-creation energy in silicon and germanium based on full-band monte carlo simulations. *IEEE Transactions on Nuclear Science*, 66(1):444–451, Jan 2019.

[37] J. Fast. The dø silicon detector for run iib at the tevatron. *Nuclear Physics B - Proceedings Supplements*, 125:352 – 357, 2003. Innovative Particle and Radiation Detectors.

[38] Maurice Garcia-Sciveres. The RD53A Integrated Circuit. Technical Report CERN-RD53-PUB-17-001, CERN, Geneva, Oct 2017.

[39] Andrew Graham. Hyperphysics, solids, fermi function. *The Physics Teacher*, 40(5):318–318, 2002.

[40] The CEPC Study Group. Cepc conceptual design report: Volume 1 - accelerator, 2018.

[41] H.H. Hansen. Measurement of the beta-ray spectra of 90Sr-90Y. *The International Journal of Applied Radiation and Isotopes*, 34(8):1241–1247, aug 1983.

[42] Peter W. Higgs. Broken symmetries and the masses of gauge bosons. *Phys. Rev. Lett.*, 13:508–509, Oct 1964.

[43] E. Hines. Performance of Particle Identification with the ATLAS Transition Radiation Tracker. Technical Report arXiv:1109.5925, CERN, Geneva, Sep 2011. Comments: 8 pages, 7 figures. Conference proceedings for the Meeting of the Division of Particles and Fields of the American Physical Society (DPF), 2011.

[44] B. Hiti et al. Development of the monolithic "MALTA" CMOS sensor for the ATLAS ITK outer pixel layer. In *Topical Workshop on Electronics for Particle Physics (TWEPP2018)*, volume 17, page 21, 2018.

[45] Vít Klupák, Ladislav Viererbl, Zdena Lahodová, Jaroslav Šoltés, Ivo Tomandl, and Petra Kudejova. Nickel foil as transmutation detector for neutron fluence measurements. *EPJ Web of Conferences*, 106:05013, 01 2016.

[46] Bjørn Tore Knudsen. Presentation of the wa97 experiment at cern. *Czechoslovak Journal of Physics*, 47(9):925–929, Sep 1997.

[47] Aljaž Kolšek, Vladimir Radulović, and Luka Snoj. Using triga mark-ii research reactor for irradiation with thermal neutrons. 09 2013.

[48] Mike Koratzinos. Fcc-ee accelerator parameters, performance and limitations. *Nuclear and Particle Physics Proceedings*, 273-275:2326–2328, 2016. 37th International Conference on High Energy Physics (ICHEP).

[49] L. LaBarga, C. Adolphsen, et al. The mark ii silicon strip vertex detector and performance of a silicon detector telescope in the mark ii detector at the slc. *IEEE Transactions on Nuclear Science*, 38(1):25–29, Feb 1991.

[50] L. Landau. On the energy loss of fast particles by ionization. *J. Phys.(USSR)*, 8:201–205, 1944.

[51] Hamid E Limodehi, Morteza Mozafari, Hesam Amiri, and François Légaré. Multi-channel fiber optic dew and humidity sensor. *Optical Fiber Technology*, 41:89–94, mar 2018.

[52] Gunnar Lindström. Radiation damage in silicon detectors. *Nuclear Instruments and Methods in Physics Research Section A: Accelerators, Spectrometers, Detectors and Associated Equipment*, 512(1-2):30–43, oct 2003.

[53] Jianwen Luo, Kui Ying, and Jing Bai. Savitzky-golay smoothing and differentiation filter for even number data. *Signal Process.*, 85(7):1429–1434, July 2005.

[54] G. Lutz. A simplistic model for reverse annealing in irradiated silicon. *Nuclear Instruments and Methods in Physics Research Section B: Beam Interactions with Materials and Atoms*, 95(1):41 – 49, 1995.

[55] K. Metodiev, M. Mironova, D. Bortoletto, R. Plackett, P. Allport, I. Asensi Tortajada, R. Cardella, F. Dachs, V. Dao, M. Dyndal, L. Flores Sanz de Acedo, P. Freeman, A. Gabrielli, L. Gonella, M. Munker, H. Pernegger, F. Piro, P. Riedler, A. Sharma, E.J. Schioppa, I. Shipsey, W. Snoeys, C. Solans Sanchez, H. Wennloef, D.P. Weatherill, D. Wood, and S. Worm. New method for estimating detector efficiency for charged particles with diamond light source. *Nuclear Instruments and Methods in Physics Research Section A: Accelerators, Spectrometers, Detectors and Associated Equipment*, page 164573, 2020.

[56] K. Metodiev, L. Vigani, R. Plackett, K. Arndt, D. Wood, D. P. Weatherill, M. Mironova, D. Bortoletto, and I. Shipsey. A compact air cooling system for testing silicon detectors based on a vortex chiller. *Nucl. Instrum. Meth.*, A940:405–409, 2019.

[57] M. Mironova, K. Metodiev, P. Allport, I. Berdalovic, D. Bortoletto, C. Buttar, R. Cardella, V. Dao, M. Dyndal, P. Freeman, L. Flores Sanz de Acedo, L. Gonella, T. Kugathasan, H. Pernegger, F. Piro, R. Plackett, P. Riedler, A. Sharma, E.J. Schioppa, I. Shipsey, C. Solans Sanchez, W. Snoeys, H. Wennlöf, D. Weatherill, D. Wood, and S. Worm. Measurement of the relative response of small-electrode cmos sensors at diamond light source. *Nuclear Instruments and Methods in Physics Research Section A: Accelerators, Spectrometers, Detectors and Associated Equipment*, 956:163381, 2020.

[58] Michael Moll. *Radiation Damage in Silicon Particle Detectors*. PhD thesis, Hamburg U., 1999.

[59] Ruth Magdalena Muenker. Test beam and simulation studies on High Resistivity CMOS pixel sensors. *Journal of Instrumentation*, 2018.

[60] M. Munker, M. Benoit, D. Dannheim, A. Fenigstein, T. Kugathasan, T. Leitner, H. Pernegger, P. Riedler, and W. Snoeys. Simulations of CMOS pixel sensors with a small collection electrode, improved for a faster charge collection and increased radiation tolerance. *Journal of Instrumentation*, 14(05):C05013–C05013, may 2019.

[61] Magdalena Munker. *Test beam and simulation studies on High Resistivity CMOS pixel sensors*. PhD thesis, University of Bonn, May 2018. Presented 26 Jun 2018.

[62] N-type silicon. (n.d.). in yourdictionary. `https://www.yourdictionary.com/n-type-silicon`. Accessed: 2020-01-16.

[63] Nikiforos Nikiforou. Performance of the ATLAS Liquid Argon Calorimeter after three years of LHC operation and plans for a future upgrade. Technical Report arXiv:1306.6756, Jun 2013. Comments: 12 pages, 25 figures, Proceedings of talk presented in 'Advancements in Nuclear Instrumentation Measurement Methods and their Applications', Marseille, 2013.

[64] K. A. Olive et al. Review of Particle Physics. *Chin. Phys.*, C38:090001, 2014.

[65] Bedabrata Pain and Bruce R. Hancock. Accurate estimation of conversion gain and quantum efficiency in CMOS imagers. In Morley M. Blouke, Nitin Sampat, and Ricardo J. Motta, editors, *Sensors and Camera Systems for Scientific, Industrial, and Digital Photography Applications IV*. SPIE, May 2003.

[66] Particulars. Particulars, Advanced meaurment systems, Ltd., 2019.

[67] Joao Pequenao. Computer generated image of the whole ATLAS detector. Mar 2008.

[68] I. Perić, R. Blanco, R. Casanova Mohr, F. Ehrler, F. Guezzi Messaoud, C. Krämer, R. Leys, M. Prathapan, R. Schimassek, A. Schöning, E. Vilella Figueras, A. Weber, and H. Zhang. Status of HVCMOS developments for ATLAS. *Journal of Instrumentation*, 12(02):C02030–C02030, feb 2017.

[69] Ivan Perić, Laurent Blanquart, Giacomo Comes, Peter Denes, Kevin Einsweiler, Peter Fischer, Emanuele Mandelli, and Gerrit Meddeler. The fei3 readout chip for the atlas pixel detector. *Nuclear Instruments and Methods in Physics Research Section A: Accelerators, Spectrometers, Detectors and Associated Equipment*, 565(1):178–187, 2006. Proceedings of the International Workshop on Semiconductor Pixel Detectors for Particles and Imaging.

[70] Ivan Perić, Mridula Prathapan, Heiko Augustin, Mathieu Benoit, Raimon Mohr, Dominik Dannheim, Felix Ehrler, Fadoua Messaoud, Moritz Kiehn, Andreas Nürnberg, Rudolf Schimassek, Mateus Vicente Barreto Pinto, Eva Vilella, Alena Weber, Winnie Wong, and Hui Zhang. A high-voltage pixel sensor for the atlas upgrade. *Nuclear Instruments and Methods in Physics Research Section A: Accelerators, Spectrometers, Detectors and Associated Equipment*, 924, 06 2018.

[71] H Pernegger, R Bates, C Buttar, M Dalla, J W Van Hoorne, T Kugathasan, D Maneuski, L Musa, P Riedler, C Riegel, C Sbarra, D Schaefer, E J Schioppa, and W Snoeys. First tests of a novel radiation hard CMOS sensor process for Depleted Monolithic Active Pixel Sensors. *JINST*, 2017.

[72] Karolos Potamianos. The upgraded Pixel detector and the commissioning of the Inner Detector tracking of the ATLAS experiment for Run-2 at the Large Hadron Collider. *PoS*, EPS-HEP2015:261, 2015.

[73] P–n junction article, wikipedia. `https://en.wikipedia.org/wiki/P%E2%80%93n_junction`. Accessed: 2020-01-17.

[74] S Redford. CLIC vertex detector r&d. *Journal of Instrumentation*, 9(08):C08014–C08014, aug 2014.

[75] F. Reidt. The ALICE pixel detector upgrade. *Journal of Instrumentation*, 11(12):C12038–C12038, dec 2016.

[76] Riedler Petra. The alice its (inner tracking system) upgrade – monolithic pixel detectors for lhc. `https://www.psi.ch/sites/default/files/import/ltp/ThursdayColloquiaEN/riedler.pdf`, 2 2018.

[77] C. Riegel, M. Backhaus, J.W. Hoorne, Thanushan Kugathasan, Lailatulhazzliza Musa, H. Pernegger, P. Riedler, D. Schaefer, Walter Snoeys, and W. Wagner. Radiation hardness and timing studies of a monolithic towerjazz pixel design for the new atlas inner tracker. *Journal of Instrumentation*, 12:C01015–C01015, 01 2017.

[78] Gianluca Aglieri Rinella. The alpide pixel sensor chip for the upgrade of the alice inner tracking system. *Nuclear Instruments and Methods in Physics Research Section A: Accelerators, Spectrometers, Detectors and Associated Equipment*, 845:583 – 587, 2017. Proceedings of the Vienna Conference on Instrumentation 2016.

[79] James William Rohlf. *Modern Physics from A to Z*. John Wiley and Sons, New York, 1994.

[80] Christian Scharf and Robert Klanner. Measurement of the drift velocities of electrons and holes in high-ohmic ¡100¿ silicon. 2015.

[81] E. J. Schioppa et al. Measurement results of the MALTA monolithic pixel detector. In *VCI 2019*.

[82] Andreas S. Schwarz. Silicon strip vertex detectors at lep. *Nuclear Instruments and Methods in Physics Research Section A: Accelerators, Spectrometers, Detectors and Associated Equipment*, 342(1):218 – 232, 1994.

[83] Sally Seidel. Silicon strip and pixel detectors for particle physics experiments. *Physics Reports*, 828:1–34, 2019. Silicon strip and pixel detectors for particle physics experiments.

[84] Stephen Seltzer. Tables of X-Ray Mass Attenuation Coefficients and Mass Energy-Absorption Coefficients, NIST Standard Reference Database 126, 1996.

[85] A. Sharma. Results of the Malta CMOS pixel detector prototype for the ATLAS Pixel ITK. In *AIDA 2020 - Fourth Annual Meeting, Oxford 2019*, 2019.

[86] W. Shockley. Currents to conductors induced by a moving point charge. *Journal of Applied Physics*, 9(10):635–636, October 1938.

[87] W. Snoeys. Monolithic pixel detectors for high energy physics. *Nuclear Instruments and Methods in Physics Research Section A: Accelerators, Spectrometers, Detectors and Associated Equipment*, 731:125–130, 2013. PIXEL 2012.

[88] M. Tanabashi (Particle Data Group). Review of Particle Physics. *Physical Review D*, 98(3):30001, aug 2018.

[89] Stefano Terzo. ATLAS ITk Pixel Detector Overview. Jul 2020.

[90] D. Turecek, J. Jakubek, M. Kroupa, and P. Soukup. Energy calibration of pixel detector working in time-over-threshold mode using test pulses. In *2011 IEEE Nuclear Science Symposium Conference Record*, pages 1722–1725, 2011.

[91] L. Vigani, D. Bortoletto, L. Ambroz, R. Plackett, T. Hemperek, P. Rymaszewski, T. Wang, H. Krueger, T. Hirono, I. Caicedo Sierra, N. Wermes, M. Barbero, S. Bhat, P. Breugnon, Z. Chen, S. Godiot, P. Pangaud, and A. Rozanov. Study of prototypes of LFoundry active CMOS pixels sensors for the ATLAS detector. *Journal of Instrumentation*, 13(2), 2018.

[92] L. Vigani, D. Bortoletto, L. Ambroz, R. Plackett, T. Hemperek, P. Rymaszewski, T. Wang, H. Krueger, T. Hirono, I. Caicedo Sierra, N. Wermes, M. Barbero, S. Bhat, P. Breugnon, Z. Chen, S. Godiot, P. Pangaud, and A. Rozanov. Study of prototypes of LFoundry active CMOS pixels sensors for the ATLAS detector. *Journal of Instrumentation*, 13(2), 2018.

[93] Luigi Vigani. *Study of CMOS prototypes for the ATLAS detector upgrade and searches for invisible decays of the Higgs boson.* PhD thesis, University of Oxford, 2018.

[94] Pauli Virtanen, Ralf Gommers, and SciPy 1.0 Contributors. SciPy 1.0: Fundamental Algorithms for Scientific Computing in Python. *Nature Methods*, 17:261–272, 2020.

[95] M. Yamada, S. Ono, T. Tsuboyama, Y. Arai, J. Haba, Y. Ikegami, I. Kurachi, M. Togawa, T. Mori, W. Aoyagi, S. Endo, K. Hara, S. Honda, and D. Sekigawa. Development of monolithic pixel detector with SOI technology for the ILC vertex detector. *Journal of Instrumentation*, 13(01):C01037–C01037, jan 2018.

[96] V Zeghbroeck. *Principles of Semiconductor Devices and Heterojunctions.* Prentice Hall PTR, 2007.

[97] Zigya online resource. `https://www.zigya.com/application/zrc/images/qvar/PHEN12060171.png`. Accessed: 2020-01-16.

[98] Markus Zinser. *The Large Hadron Collider*, pages 47–51. Springer International Publishing, Cham, 2018.

[99] V. M. Zolotarev. *One-dimensional stable distributions*, volume 65 of *Translations of Mathematical Monographs.* American Mathematical Society, Providence, RI, 1986. Translated from the Russian by H. H. McFaden, Translation edited by Ben Silver.